Advanced TiAlTaN hard coatings for cutting tools

Dipl.-Ing. Birgit Großmann

being a thesis in partial fulfilment of the requirements for the degree of a **Doktor der montanistischen Wissenschaften (Dr. mont.)**

at the Montanuniversität Leoben

Leoben, March 2018

Affidavit

I declare in lieu of oath, that I wrote this thesis and performed the associated research myself, using only literature cited in this volume.

Leoben, March 2018

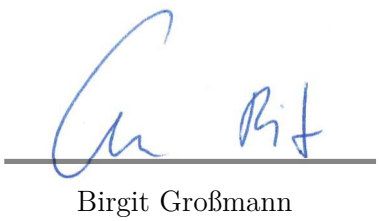

Birgit Großmann

Acknowledgements

Hereinafter, I want to express my gratitude to all the people who contributed to the progress and ultimately to the finalization of this thesis:

First of all, I want to express my sincerest gratitude to Prof. Dr. Christian Mitterer, for placing trust in me and giving me the possibility to compose this thesis at the Chair of Functional Materials and Materials Systems. I am grateful for his expertise, his endless support and patience. His outstanding way to guide and motivate people is inspiring.

I am very grateful to my supervisors Dr. Nina Schalk and Dr. Michael Tkadletz, for the discussions, their support in every situation and for keeping their office doors always open for me.

Special thanks to Dr. Christoph Czettl and DI Markus Pohler from CERATIZIT Austria, for their great support, for all the meetings and trips to Reutte, which always resulted in new visions and motivation boosts.

Financial support by the Austrian Research Promotion Agency FFG is gratefully acknowledged.

Acknowledgements

I want to thank all my colleagues and coworkers at the Department of Physical Metallurgy and Materials Testing for the great working atmosphere. Many of them became friends more than just working mates during these years. Special thanks to 'das Büro', for sharing not just one office. It was a lovely and awesome time.

Many thanks to the staff of the Department of Physical Metallurgy and Materials Testing, especially to Alfons, Angelika, Eva-Maria, Gerhard, Hilde, Karl-Heinz, Regina, Sabrina, Silvia and Veli, for the fantastic support during these years. I am also very grateful to Thomas Christof from the Chair of General and Analytical Chemistry, and to Bernhard Sartory from the Material Center Leoben for their great support.

I also want to thank DI Andreas Jamnig and Thaddäa Rath for their contribution to this thesis.

Special thanks to all of my friends, which never stopped remembering me that there are important things going on outside the office.

I couldn't have finished this thesis without the love and support of my family, my mother Margit, my brother Jürgen and my boyfriend Christoph. Thank you for your patience and endurance during these years, and for giving me the feeling that I would always be welcome and beloved, no matter if or how this thesis would have ended.

Table of content

1. Introduction 1

2. Coating synthesis 5

2.1. Cathodic arc evaporation 6

2.2. Film growth 7

3. $Ti_{1-x}Al_xN$ 11

3.1. Microstructure 11

3.2. Spinodal decomposition 13

3.3. Properties 14

3.4. Alloying of $Ti_{1-x}Al_xN$ with Ta 20

4. Tribological aspects and machining 23

4.1. General aspects of cutting processes 23

4.2. Wear mechanisms relevant for cutting 24

5. Summary and outlook 27

6. Publications 39

6.1. Included publications 39

6.2. Further work contributing to this thesis: 40

6.3. Other publications: 40

Publication I 41

Publication II 63

Publication III 81

1. Introduction

The application of coatings to modify surface properties is documented to start at least ~5000 years ago. Gold was one of the first materials applied, due to its occurrence as solid gold in nature and its workability with the tools available at that time. It was used as gold leaf for decorative reasons, i.a. in ancient Egypt. The deposition of thin films from the vapor phase is limited to the last few centuries, and further advanced by the exploration of the basics of physical- and chemical vapor deposition (PVD and CVD) in the 19th century [1]. As protective coating for wear intensive applications, TiN enjoyed great popularity and is still commonly used. It exhibits a high thermal stability and oxidation resistance up to ~500 °C [2,3]. Additionally, its neat golden color facilitates the use as decorative coating, and is also beneficial for cutting applications for easy detection of wear.

The demand for further performance enhancement towards increased thermal stability and wear resistance led to versatile alloying concepts of TiN-based coatings. The deposition of metastable solid solutions beyond the thermodynamic equilibrium could be realized using PVD techniques, where – among others – $Ti_{1-x}Al_xN$ coatings as the most popular representative emerged. In the late 1980's, first reports about the excellent wear and cutting behavior of $Ti_{1-x}Al_xN$ hard coatings were published, pioneered by Münz [3] and Knotek [4]. The former documented on the superior properties of $Ti_{1-x}Al_xN$ with respect to thermal stability and oxidation resistance. In turning tests, $Ti_{1-x}Al_xN$ coated tools showed a 2-3x higher tool lifetime compared to TiN, while in drilling tests into cast iron a 12 time higher tool lifetime was achieved [3]. The drilling tests performed by Knotek *et al.* [4] showed that drills

coated with $Ti_{1-x}Al_xN$ had a 2.5x higher tool lifetime compared to TiN coated tools, and 15x higher compared to uncoated tools. Randhawa *et al.* [5] confirmed that tremendous increase of the cutting tool lifetime and reported on drilling tests, where a tool lifetime increase of 200 times compared to uncoated tools was achieved, and also more than twice compared to tools coated with TiN. Based on these sensational results, many researchers and companies started the challenging journey of further improvement of this coating system, which lasts until today, 30 years later, and is still ongoing. $Ti_{1-x}Al_xN$ coatings exhibit extraordinary features, which makes them an excellent choice for cutting applications. The enhanced oxidation resistance stems from the nature of Al to form a hard, chemically stable alumina layer on the coating surface, as soon as it is thermally loaded to temperatures exceeding ~700 °C in ambient air [6,7]. Therefore, further oxidation is drastically decreased, since the transport of oxidative agents through the alumina layer is hindered [8,9]. The metastable $Ti_{1-x}Al_xN$ solid solution tends to spinodal decomposition at temperatures beyond ~750-850 °C to face centered cubic (fcc) Ti-rich and fcc Al-rich domains, which results in coherency strains between them and the $Ti_{1-x}Al_xN$ matrix, and thus in hardness increase due to age hardening [10,11]. Consequently, coated tools benefit from an improvement of the mechanical properties during machining, as a result of the temperature increase at the cutting edge. However, at even higher temperatures, the metastable fcc AlN transforms to its stable wurtzite form, leading to a deterioration of the mechanical properties of the coating [12].

Despite the excessive research undertaken during the past decades, the enthusiasm about $Ti_{1-x}Al_xN$ ternary and also $Ti_{1-x}Al_xN$-based quaternary coatings is still unbroken. Although many modern alternative manufacturing processes are on the rise, e.g. additive manufacturing or 3D printing, cutting represents still one of the most important shaping technologies, and the challenge nowadays is the tailoring of coatings for a broad spectrum of every possible application [13].

Consequently, the aim of this work is to widen the available knowledge on Ta alloying of $Ti_{1-x}Al_xN$ coatings. In particular, three main questions stood at the beginning of this thesis.

- To what extent do the growth conditions influence the microstructural properties and the thermal stability of $Ti_{1-x}Al_xN$ coatings?
- How does the Ta content influence the thermal stability of $Ti_{1-x-y}Al_xTa_yN$ coatings?
- In which way does the implementation of Ta atoms to the $Ti_{1-x}Al_yN$ solid solution affect the oxide layer formation and the tribological properties at elevated temperatures?

The first part of the present thesis presents an overview on synthesis of $Ti_{1-x}Al_xN$-based hard coatings, their microstructure and main properties. Within the second part, the defined research questions are highlighted in the form of three published papers.

2. Coating synthesis

Thin films deposition techniques may be described by the source of the coating material used or its transportation to the substrate. PVD and CVD represent the two most important deposition techniques for the production of hard coatings. During CVD, the precursors (gaseous materials) are supplied to the deposition chamber, and the formation of a coating on the substrates occurs by condensation of species generated by chemical reactions. The reactions are mainly thermally activated; hence for hard protective coatings, high substrate temperatures are necessary [14,15], e.g. for TiN ~850-1000 °C [16,17]. These high temperatures limit the possible substrate materials and hence application. For PVD processes, a solid target acts as material source, which is vaporized in order to enable the material transport to the substrates. The vaporized material condenses subsequently on the substrates in order to grow a thin film. Due to the huge flexibility of growth conditions of PVD processes, a vast variety of coatings (metals, alloys, compounds) with versatile properties can be produced [18]. One drawback of the vacuum-based PVD processes is the fact that the coating is only applied to those areas directly facing the target; therefore in indusrial-scale deposition devices, rotating substrate holders are commonly used to ensure homogeneous coating deposition. With CVD usually done at ambient or slightly reduced pressures, also the coating of averted areas is possible. Although considerable effort has recently been made in enabling the deposition of $Ti_{1-x}Al_xN$ coatings by CVD [19–21], PVD techniques are still the most common ones. Since the coatings studied in the present thesis were

unexceptionally grown by cathodic arc evaporation, solely this deposition technique is hereinafter further explained.

2.1. Cathodic arc evaporation

Cathodic arc evaporation (CAE) is a PVD technique widely used for the deposition of hard coatings. The vapor is produced by a DC high-current but low-voltage arc, running between a cathode (i.e., the target) and an anode in a vacuum chamber. The arc is initiated by a short-time contact of the anode (mechanical igniter) and the cathode, with an immediate removal of the anode after ignition. With the very small spot formed at the cathode surface (10^{-8}-10^{-4} m in diameter), extremely high current densities (10^{6}-10^{12} Am^{-2}) occur next to high areal power densities (10^{13} Wm^{-2}). The fast heating of this area enables melting and further vaporization of the cathode material as shown in Fig. 1a.

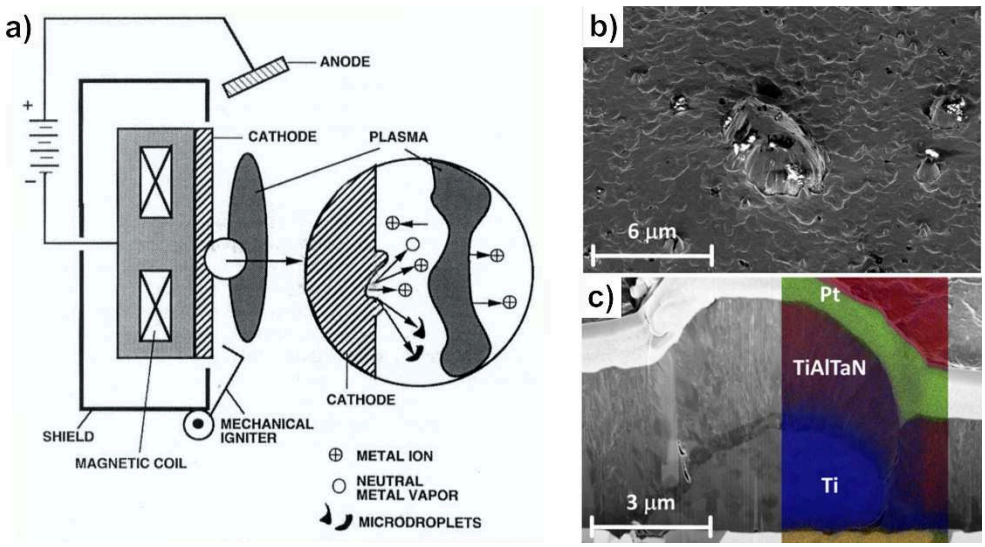

Fig. 1 a) Schematic of the cathodic arc evaporation process [15], b) droplets formed on the coating surface, c) cross section of a droplet located at the interface substrate/coating and its impact on the coating up to the surface, including elemental mapping with energy dispersive X-ray spectroscopy [22].

The cathode spot moves with velocities of ~100 m/s randomly along the target surface, where the arc is confined by magnetic fields and a passive border (e.g. an insulating surrounding). Hence, when the arc leaves the target area, it gets

extinguished. The magnetic field can be adapted to control the plasma, and leads to mainly multiple ionized vapor species. Consequently, a uniform, dense coating can be achieved with CAE, especially for biased processes, where the ions get accelerated towards the substrate due to an applied substrate potential (bias voltage) [15,23,24].

A major drawback of the CAE process is the formation of macroparticles (droplets) within the coating, which stem from additionally ejected molten droplets and solid particles from the target. The incorporation of these droplets within the coating limits their application possibilities significantly. Droplets are typically generating cavities caused by shadowing effects. They can reach several micrometers in size, and generate microstructural coarsened cauliflower features protruding the coating surface [25], see Fig. 1c. The consequently pronounced surface roughness of the coatings caused by droplets, and their increased defect density enables a higher diffusion rate, which promotes oxidation during thermal loading [22]. Tkadletz *et al.* investigated the droplets formed within a $Ti_{1-x-y}Al_xTa_yN$ coating, and reported on their pronounced impact on the tribological properties [22]. Fig. 1b shows a droplet on the coating surface, and in Fig. 1c, the chemical composition of the droplet, and its impact on the surrounding film as well as the film growth is depicted.

2.2. Film growth

When the atom from the vapor phase impinges on the substrate, it either condensates on its surface or gets immediately reflected. If it transfers a sufficient amount of energy to the surface, it gets weakly bonded as an adatom. The kinetic energy of the adatoms enables movement on the surface, until they desorb or form a stable nucleus at the substrate surface or join an already existing nucleus to form clusters. For a low tendency of interaction between the adatom and the surface, widely spread nuclei are formed, while a high interaction tendency results in a high nuclei density [14,18]. With further deposition, the clusters grow, and form a continuous film. In Fig. 2, the three main growth modes, which are depending on the binding energy, are illustrated. The island growth mode after Volmer-Weber (Fig. 2a) occurs when the atoms are more strongly bound to each other than to the

substrate. The clusters grow in three dimensions to form islands. For example, hard coatings as well as semiconductors on oxides grow with that mode. The second growth mode is named after Frank-Van der Merwe, or layer growth, and is illustrated in Fig. 2b. Coatings growing with this mode have stronger bound atoms to the substrate than to each other. The clusters grow in two dimensions to form planar, piled sheets. One example for the layer by layer growth mode is the epitaxial growth of single crystals. The layer plus island mode, shown in Fig. 2c, also called Stranski-Krastanov mode, is a combination of the two mentioned before. After forming at least one monolayer, the film starts to grow in three dimensions to form islands. This growth mode is the most common, and is valid for deposition of metals on metals or semiconductors [15].

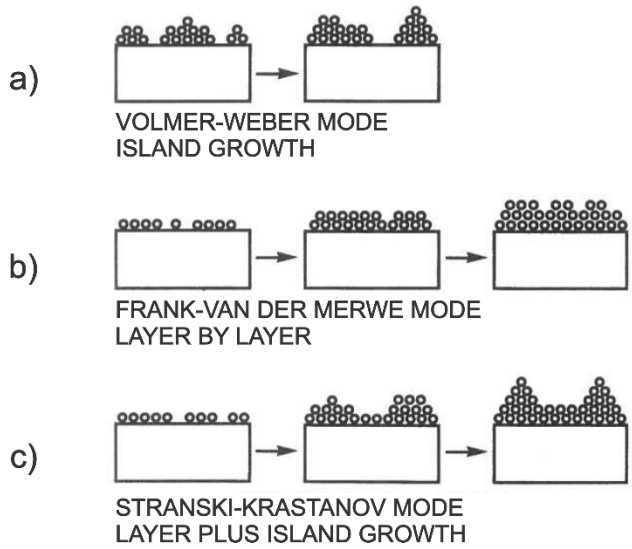

Fig. 2 Basic film growth modes: a) island, b) layer by layer, c) layer plus island mode, after [15].

Various factors are decisively influencing film growth during deposition, i.e., the nature of the substrate, the substrate temperature, the deposition rate, the angle of incidence of the incoming particle flux, the pressure and nature of the ambient gas. The influence of various deposition parameters can be illustrated in a simplified approach in structure zone models (SZM). Movchan and Demchishin proposed 1969 a SZM [26], suggesting three different constitutional zones to be formed within

coatings deposited by electron beam evaporation, as a function of the homologous temperature $T^* = T_s/T_m$, where T_s is the substrate temperature during deposition and T_m is the melting temperature of the coating material. Thornton [27] included information on the Ar gas pressure, and implemented a fourth zone (zone T) in the SZM he presented in 1974. In both models, the structure of the coatings deposited with a low T^* (zone 1) appears porous due to the reduced surface mobility of the adatoms, with tapered crystallites formed in direction of the incident atoms. With increasing temperature, the grains get denser packed, and more fibrous shaped (zone T). Shadowing effects can be balanced due to higher surface diffusivity. Another temperature increase leads to zone 2, where surface diffusion is dominating, and a high amount of nuclei are generated. A columnar structure is created, showing increasing column width with increasing temperature. In zone 3, the temperature is high enough to enable volume diffusion, therefore segregation of impurities during film growth occurs, and a dense, recrystallized film is achieved.

Messier *et al.* [28] presented a SZM in 1984, where he added the influence of the bias voltage to the different zones. Anders [29] proposed recently an adapted form of the Messier' SZM, with the following additions: *(i)* a temperature shift due to the energy of the arriving particles to T^*, *(ii)* the normalized energy E* includes displacement as well as heating due to the kinetic energy of bombarding particles, *(iii)* the film thickness shown at the z-axis highlights the influence of a high bias voltage causing re-sputtering of condensed adatoms during film growth. Fig. 3 shows the different regions within Anders' SZM, and the influence of kinetic energy on the borders between the zones, as well as on the coating thickness.

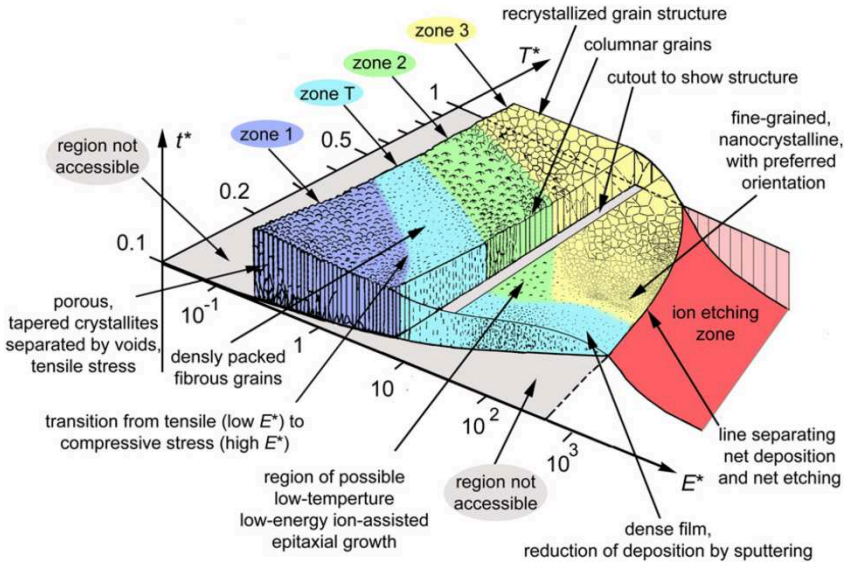

Fig. 3 Structure zone model by Anders illustrating different zones of coating structure as a function of temperature T^* and energy E^* [29].

The kinetic energy of the bombarding particles is mainly influenced by the bias voltage. A bias voltage is a negative potential applied to the substrate, which is used during deposition to accelerate the positively charged ions towards the growing film. Due to their intense impact on the surface, caused by the increased kinetic energy, pronounced resputtering at tips and edges, and condensation even at shadowed areas can be achieved, which leads to a smoother surface, and a reduced coating thickness. Additionally, the impact to the growing film induces residual stress, which can be used to tailor mechanical properties. Therefore, the porous zone 1 in Fig. 3 gets smaller with increasing normalized energy, and the zones are shifted towards lower temperatures [30].

3. $Ti_{1-x}Al_xN$

3.1. Microstructure

The microstructure of $Ti_{1-x}Al_xN$ hard coatings depends strongly on the Al content x, as well as on the deposition conditions used. TiN as primary phase represents a fcc lattice, while for AlN the hexagonal wurtzite structure is stable. AlN exhibits in general a covalent bonding character, while nitrides of transition metals usually are characterized by metal bonding; with common metallurgical techniques the synthesis of $Ti_{1-x}Al_xN$ is hindered due to the extremely low mutual solubility of AlN in TiN and vice versa [31,32], see Fig. 4a. With its ability to deposit metastable solid solutions, PVD allows to grow materials beyond the thermodynamic equilibrium, which possess versatile outstanding properties. Holleck *et al.* [31] suggested a metastable phase diagram of AlN in TiN, which is illustrated in Fig. 4b.

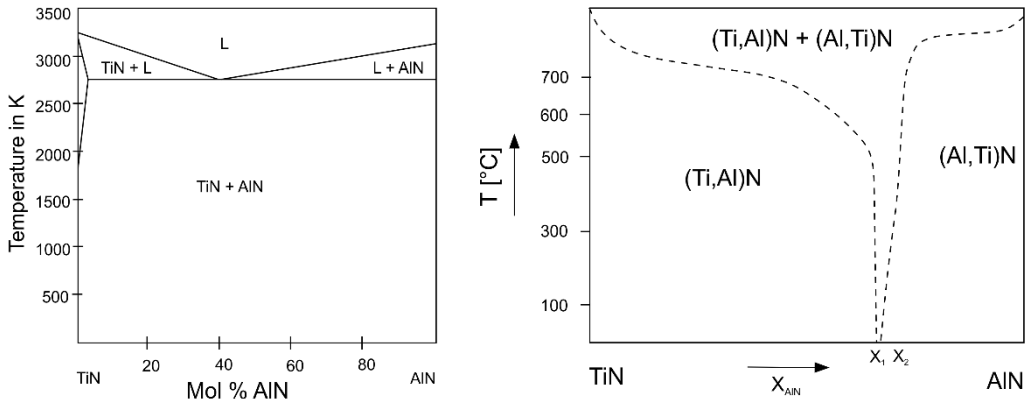

Fig. 4 a) Quasi-binary equilibrium and b) metastable TiN-AlN phase diagram (after [31]).

With the incorporation of Al into TiN, the Al atoms substitute the Ti atoms within the fcc lattice forming $Ti_{1-x}Al_xN$, which remains stable up to x~0.6-0.75, depending on the deposition conditions used [33]. A schematic of the microstructure as a function of the Al content is illustrated in Fig. 5a.

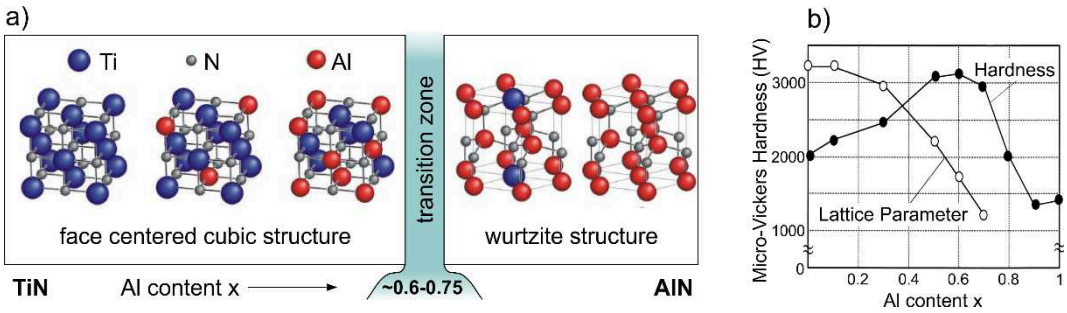

Fig. 5 a) Microstructure (after [34]) and b) hardness of $Ti_{1-x}Al_xN$ coatings with different Al content x (after [35]).

An increasing AlN content results in a hardness increase due to solid solution hardening within the cubic regime, as shown in Fig. 5b. Mayrhofer *et al.* [36] reported that the phase stability of the fcc-$Ti_{1-x}Al_xN$ depends on the number of Ti-Al bonds within the lattice, since they strongly influence the electronic properties, the bond energy and the configurational entropy of the system. Hence, not only the Al content affects the phase regime, but also the distribution of Al atoms within the TiN lattice. For a low amount of Ti-Al bonds, the energy of formation is also low. This explains that the solubility limit of Al in fcc-TiN was reported between ~0.6≤x≤0.75, depending on the deposition parameters used [37–44]. A higher bias voltage applied to the substrate during deposition leads to increased energy of the impinging ions during film growth; the consequently enhanced mobility of the adatoms on the surface can widen the solubility limit of the fcc phase in $Ti_{1-x}Al_xN$ coatings, as shown in publication I. Due to the ion bombardment, new nucleation sites can be generated, which result in a finer grained structure [42]. On the other hand, an higher ion energy could cause selective resputtering of the (lighter) Al atoms [45,46]. However, if the solubility limit of the metastable fcc-$Ti_{1-x}Al_xN$ phase is exceeded, a dual phase structure consisting of fcc and wurtzite is formed. A further

increase of x results in formation of the w-$Ti_{1-x}Al_xN$ phase, where Ti substitutes Al atoms in the w-AlN lattice.

3.2. Spinodal decomposition

The metastable fcc-$Ti_{1-x}Al_xN$ solid solution is characterized by a phase stability up to ~750-850 °C, where first signs of spinodal decomposition are detectable. It decomposes under specific conditions (i.e. sufficient temperature and time) and forms Ti-rich and Al-rich domains; between these cubic domains, coherency strains arise and increase with increasing decomposition progress.

The formed fcc-AlN-rich domains are again metastable; further thermal impact results in transformation to w-AlN [10,47,48]. The higher the annealing temperature is, the faster the decomposition is proceeding, and also the size of the respective Ti-rich and Al-rich domains increases [49]. Fig. 6a and b illustrate the microstructural changes occurring within a $Ti_{0.5}Al_{0.5}N$ coating during annealing in vacuum by dynamic scanning calorimetry and X-ray diffraction [10]. The four DSC features in Fig. 6a can be referred to the following processes: *(i)* recovery (DSC1), *(ii)* beginning spinodal decomposition (i.e., formation of fcc-AlN domains, DSC2), *(iii)* progressed spinodal decomposition and formation of fcc-AlN and fcc-TiN phases (DSC3), *(iv)* completed decomposition, formation of fcc-TiN and w-AlN phases (DSC4). The decomposition process starts for this coating at 860 °C, and is still in progress at 1100 °C, evidenced by the $Ti_{0.5}Al_{0.5}N$ solid solution X-ray diffraction peak being shifted towards lower diffraction angles. However at 1400 °C, the peak is located near the standard peak position of fcc-TiN, indicating that spinodal decomposition is finished. In Fig. 6c, the reconstructed 3D atom probe tomography tip shows the formed Ti- and Al-enriched domains due to spinodal decomposition after annealing at 1350 °C [50].

The formation of w-AlN is unfavored due to several reasons: On the one hand, w-AlN exhibits inferior mechanical properties, therefore the mechanical properties of the coatings deteriorate. On the other hand, the transformation of fcc-AlN to w-AlN is accompanied by an increase of the molar volume, which generates

strains and thus micro-cracks. Therefore, additional diffusion paths in the coating are provided [51], which deteriorates coating adhesion, thermal stability and oxidation resistance.

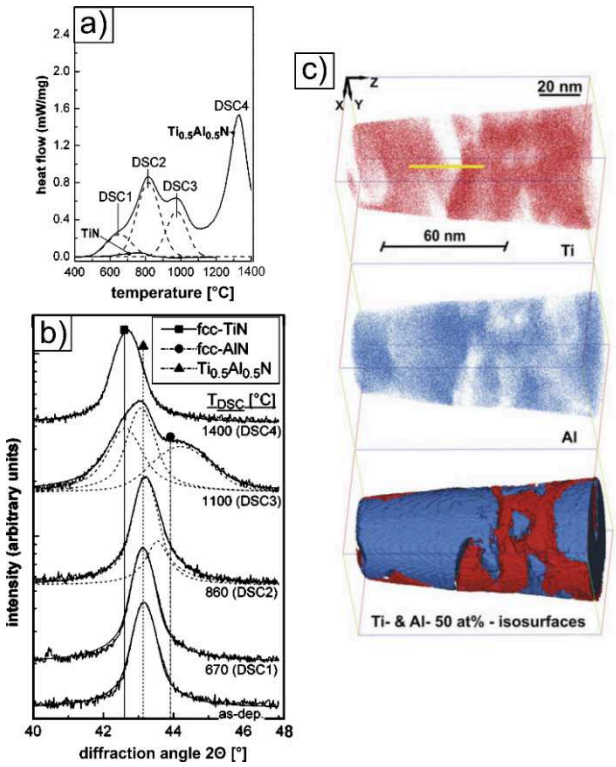

Fig. 6a) Changes of the microstructure of a $Ti_{0.5}Al_{0.5}N$ coating studied by differential scanning calorimetry and evidenced by X-ray diffractograms in b) for four annealing temperatures [10]. c) The reconstructed 3D atom probe tomography image shows the decomposition in metastable Al-rich and Ti-rich domains after annealing at 1350 °C [50].

3.3. Properties

Compared to bulk materials, the definition of mechanical properties of coatings is challenging because of the often occurring substrate influence. Nevertheless, the **hardness** of $Ti_{1-x}Al_xN$ coatings has been in the focus of many publications since the last three decades [10,39,41,52]. The hardness is closely connected to the phase evolution within the coating, i.e. the Al content. Increasing the Al content in the coating leads to a hardness increase up to the solubility limit of AlN within the fcc-$Ti_{1-x}Al_xN$ solid solution; however, even a low w-$Ti_{1-x}Al_xN$ phase fraction leads to a significant hardness drop. The hardness of the coatings is also

influenced by its morphology, which depends on its growth conditions. An increase of the **bias voltage** applied to the substrate leads to a lower crystallite size (see section 2.1.2), and promotes the formation of the fcc-$Ti_{1-x}Al_xN$ up to higher Al contents [42]. Consequently, this results in a higher hardness compared to coatings deposited with a lower bias voltage (see publication I). When the fcc-$Ti_{1-x}Al_xN$ phase is exposed to elevated temperatures, the coherency strains stemming from spinodal decomposition result in a hardness increase, see Fig. 7. This beneficial "self-hardening" effect is known as age hardening [10,39,53]; since during cutting applications high thermal loading occurs, the hardness increase at application temperature is one of the most important factors for the success of $Ti_{1-x}Al_xN$ coatings in machining. However, as soon as first signs of w-AlN formation are evident, the hardness deteriorates.

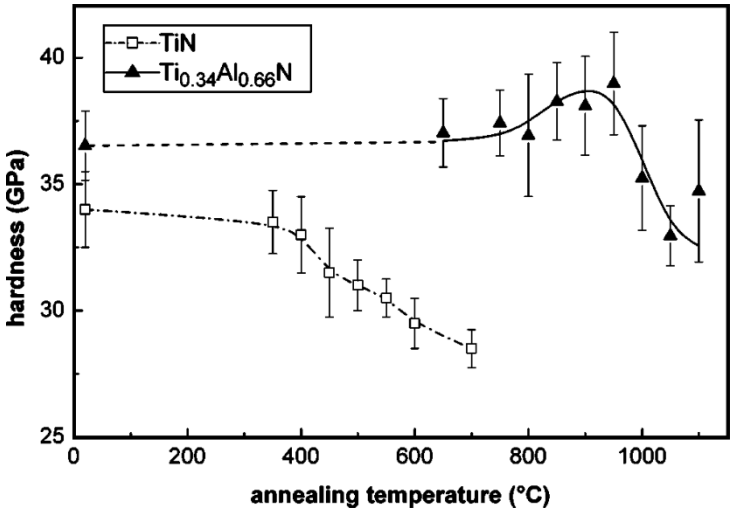

Fig. 7 Hardness of $Ti_{0.34}Al_{0.66}N$ compared to TiN as a function of the annealing temperature [10].

Another advantage of $Ti_{1-x}Al_xN$ compared to TiN coatings is the increased **oxidation resistance**. In general, the oxidation process involves charge transfer, i.e. the movement of electrons, oxygen anions and metal ions as it is illustrated in Fig. 8 [12]. The metal atoms of the coating material get ionized to M^{2+} (i.e., oxidized, since they give electrons e^-), and consequently the oxide atoms at the coating surface get reduced to O^{2-}.

At 600-700 °C in ambient air, on the surface of $Ti_{1-x}Al_xN$ coatings a homogeneous oxide layer M_xO_y, with M=(Al,Ti), is formed. The inward diffusion of O^{2-} controls the oxidation process [8]. At temperatures beyond ~700-800 °C, different oxide layers are formed.

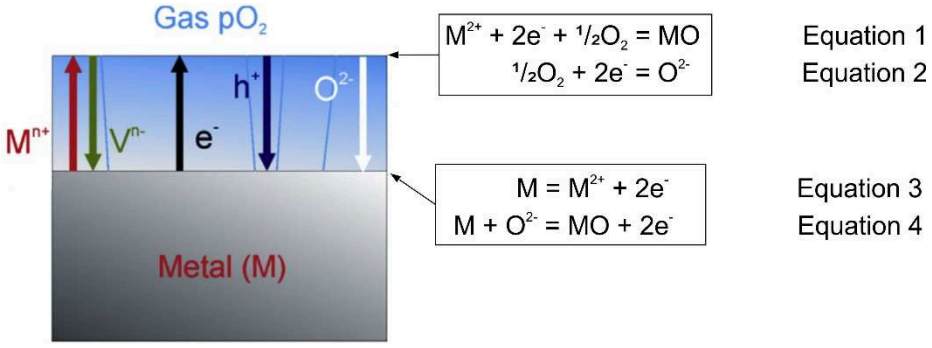

Fig. 8 Main transport mechanisms during oxide scale growth on the surface of a metal, simplified model (modified after [12,54]).

The activation energy for oxidation of Ti is 1.9-2.1 eV, while for Al it is 2.3 eV [9]. Therefore, Ti oxidizes first; when subsequently Al starts to react with O_2, it forms a dense, protective Al_2O_3-rich toplayer at the coating surface, with a porous TiO_2-rich sublayer and the remaining $Ti_{1-x}Al_xN$ underneath. For further oxidation, O^{2-} ions have to be transported from the surface through the Al_2O_3-rich toplayer and the TiO_2-rich interlayer to the oxide-nitride interface, while simultaneous outward diffusion of Al^{3+} from the nitride layer to the surface is necessary. Fig. 9 shows a cross section through a $Ti_{0.54}Al_{0.46}N$ coating with a typical oxide layer formation after annealing in ambient air at 900 °C. The dark toplayer represents the dense Al_2O_3-rich layer, while the brighter, porous sublayer is TiO_2-rich.

Depending on the oxidation temperature, Ti can either form the stable rutile (r) or the metastable anatase (a) TiO_2, where the latter transforms between 400-1000 °C to the stable r-TiO_2, depending on purity, synthesis and environmental conditions [55,56]. For bulk materials, the transformation temperature is given as 915 °C [57]. a-TiO_2 exhibits worse mechanical properties than r-TiO_2. In addition, the monotropic phase transformation to r-TiO_2 is accompanied by a density increase. Thus, stress is generated between the oxide-nitride interface due to the volume

decrease, and the transformed TiO_2-rich layer exhibits cracks and pores, which act as diffusion paths [9]. Moreover, the adhesion of the Al_2O_3-rich toplayer is affected by the increased stress level, and delamination of the oxide layers due to cracks may occur. Hence, the formation of the anatase phase is unfavored, and avoiding it is a major goal in the design of advanced $Ti_{1-x}Al_xN$ hard coatings.

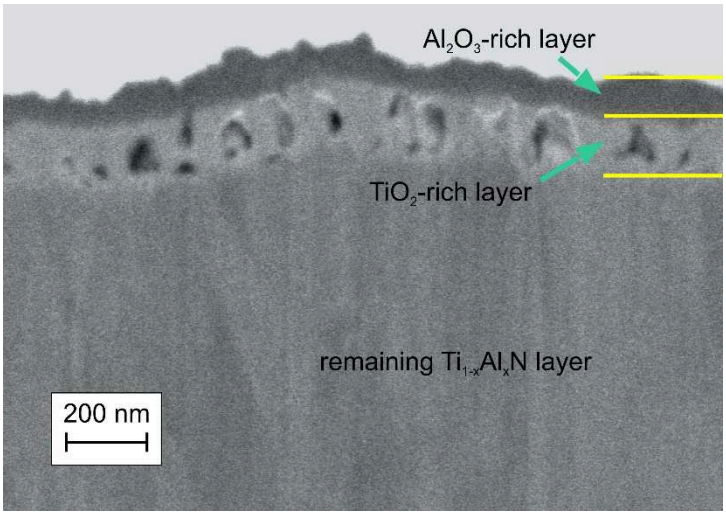

Fig. 9 Scanning electron microscopy cross section illustrating the oxide scale evolution on a $Ti_{0.54}Al_{0.46}N$ coating after annealing at 900 °C for 1 h in ambient air (own work).

The mobility of Al^{+3} and O^{2-} within the Ti-rich oxide sublayer is considerably higher than within the dense Al_2O_3–rich layer, which retards the ongoing oxygen transport through the oxide scale to the remaining coating. Therefore, the limiting factor for further oxidation is the formation of a protective Al_2O_3–rich toplayer.

The **wear resistance** of $Ti_{1-x}Al_xN$ coatings is strongly connected to its hardness, and is at room temperature (RT) also lower for dual phase coatings consisting of fcc- and w-$Ti_{1-x}Al_xN$ than for single phase fcc-$Ti_{1-x}Al_xN$. For coatings deposited by cathodic arc evaporation, droplets protruding out of the coating surface can lead to increased wear rates during tribological testing. The local pressure these droplets are exposed to in sliding contacts causes on the one hand crack formation within the coating, which provides diffusion paths for corrosive or oxidative media; on the other hand, a possible delamination of droplets leads to increased amount of

wear debris, which can act as abrasive medium [22]. In general, **tribological properties** of hard coatings are next to the surface roughness strongly affected by environmental conditions, e.g. moisture and temperature. Pfeiler *et al.* found indication for tribooxidation of $Ti_{1-x}Al_xN$ coatings also at RT [58]. They investigated the coatings in different media at RT, and found a strong sensitivity to moisture. While for coatings tested in synthetic air with reduced moisture, a maximum wear track depth of ~0.5 µm was found, whereas the tests performed in ambient air at a relative humidity of 35±5% caused a five times higher wear track depth of ~2.5 µm. Therefore, even at RT, moisture during testing results in the formation of a thin oxide layer within the wear track, which may be removed during every contact by the counterpart, yielding additional wear debris and thus promoting abrasion.

Tribological testing of $Ti_{1-x}Al_xN$ at elevated temperatures results on the one hand in a less pronounced effect of the droplets on friction, and yields up to certain testing temperatures less wear compared to RT [22]. On the other hand, in ambient air oxidation processes of the coating have a strong influence on the tribological behavior. The stable Al_2O_3-rich toplayer formed during testing at elevated temperature exhibits good abrasive wear resistance due to its high hardness [6,7]. TiO_2, among other oxides, forms solid lubricant-like layers when exposed to elevated temperatures, being of high interest for the machining industry due to its low friction. In general solid lubricants possess a layered structure, where the layers are solely weakly bonded between themselves, but the atoms in each layer are strong covalently bonded and densely packed [59]. The lubricity stems from the ability of the layers to slide over each other, acting as low shear strength nanofilm on the top of the coating. Shear takes place within the nanofilm, and the load is supported by the coating [13]. This predominates over natural cleavage planes [60] and results in a low friction coefficient, while the strong bonding within the layers is responsible for reduced wear of the solid lubricants. For TiN-based coatings, the formation of a solid lubricant-like structure is assumed to occur as follows:

When r-TiO_2 is formed during tribological testing at elevated temperatures, it possesses a reduced friction coefficient compared to room temperature testing of

$Ti_{1-x}Al_xN$. This relies in the formation of substoichiometric oxides, the so-called Magnéli phases (i.e., Me_nO_{2n-1}), which possess a solid lubricant characteristic layered structure. Magnéli [61,62] found first, that oxides of tungsten, molybdenum, titanium and vanadium form homologous series based on the rutile crystal structure with recurrent dislocations. During tribological testing at elevated temperatures, oxygen from the coating surface is removed by the counterpart, but the thermal loading also induces diffusion of vacancies into the surface. When oxygen is lost as $½O_2$ from the surface, it leaves two electrons in the oxygen vacancy to maintain electrical neutrality [60,63], see reverse equation 2 in Fig 8. According to Gardos [60,64], the reduced stoichiometry stems from the oxygen removal during the simultaneous oxidation and wear processes, and hence causes an increasing amount of oxygen vacancies. With further oxygen loss, some Ti^{4+} may change their charge state to Ti^{3+}; anti-phase boundaries are formed, where Ti ions are located closer to each other, and ionic repulsion influences the bonding strength and the energy between the ions. Diffusion of vacancies enables the self-arranged formation to ordered, planar defects, which are strongly bonded within each layer, but the bonding of the layers to each other is weak. The degree of oxygen loss and the amount of Ti^{3+} ions is of huge importance for the microstructure of the oxide scale, and influences strongly the shear strength of the layers. The interaction between these crystallographic shear (CS) planes is influenced by several terms: (*i)* the electrostatic interaction of ions within one layer, (*ii*) the electrostatic interaction of ions within the CS planes to the residual crystal structure, (*iii*) the strain energy within the crystal, and (*iv*) the repulsive energy between the CS planes. When rutile is reduced to $TiO_{1.98}$ - $TiO_{1.93}$, CS planes which lie upon {132} planes develop; with increased reduction the electrostatic interaction energy (whether repulsion or attraction) between the CS planes becomes more important. The repulsion and the therefore weakly bound layers lead to their ability to slide over each other, resulting in a relatively low friction coefficient. The more pronounced reduction to $TiO_{1.89}$ enables CS planes with an index between {132} and {121}, where the total higher energy of the {121} planes influences the bond strength and therefore the friction coefficient of the coating; the distance between the Ti ions

is further reduced, and the ionic repulsion between the crystallographic shear plane boundaries switches to increased dislocation motion with a decrease of the lattice energy. Another reduction to $TiO_{1.66}$ results again in a decrease of the distance between the Ti ions and a predominating {121} CS plane, which holds an increasing lattice strength and hence again a higher friction coefficient [64,65].

3.4. Alloying of $Ti_{1-x}Al_xN$ with Ta

A key to further improve the performance of hard coatings is widening the ternary $Ti_{1-x}Al_xN$ system to quaternary systems with tailored properties. In various publications, the benefits of quaternary alloying elements are pointed out [51,66–71]. Tantalum as alloying element was chosen for the present research because of various reasons. It is known to form a metastable solid solution with $Ti_{1-x}Al_xN$, and to widen the solubility limit of Al in the fcc-$Ti_{1-x-y}Al_xTa_yN$ [70]. In Fig. 10a, the ab initio calculated energies of formation for cubic and wurtzite $Ti_{1-x}Al_xN$ and $Ti_{1-x-y}Al_xTa_yN$, respectively, are shown. For the Ta containing coating, the formation of the wurtzite phase is shifted towards slightly higher Al contents than for $Ti_{1-x}Al_xN$ [72]. In Fig. 10b, the influence of Ta on the coating microstructure is depicted. While the coating at the bottom, $Ti_{0.33}Al_{0.67}N$, shows major wurtzite phase peaks, the coating $Ti_{0.32}Al_{0.63}Ta_{0.05}N$ (i.e., the same Ti/Al ratio, but containing 5 at.-% Ta) shows next to dominant fcc-$Ti_{1-x-y}Al_xTa_yN$ solid solution peaks only minor w-AlN peaks.

For $Ti_{1-x}Al_xN$ coatings deposited by cathodic arc evaporation, the Ti content within the coatings has often been reported to be higher than in the target [73,74]. Adding Ta to the target results in a higher Ta content within the coating than in the respective target, which is mainly at the expense of the Al content (see Fig. 10c). The significant loss of Al during deposition can be explained on the one hand by the mass difference between Al, Ti and Ta, with the higher possibility of the light Al atom to get scattered during the gas transport phase. Another explanation is the higher resputtering probability of Al atoms, as reported in [51].

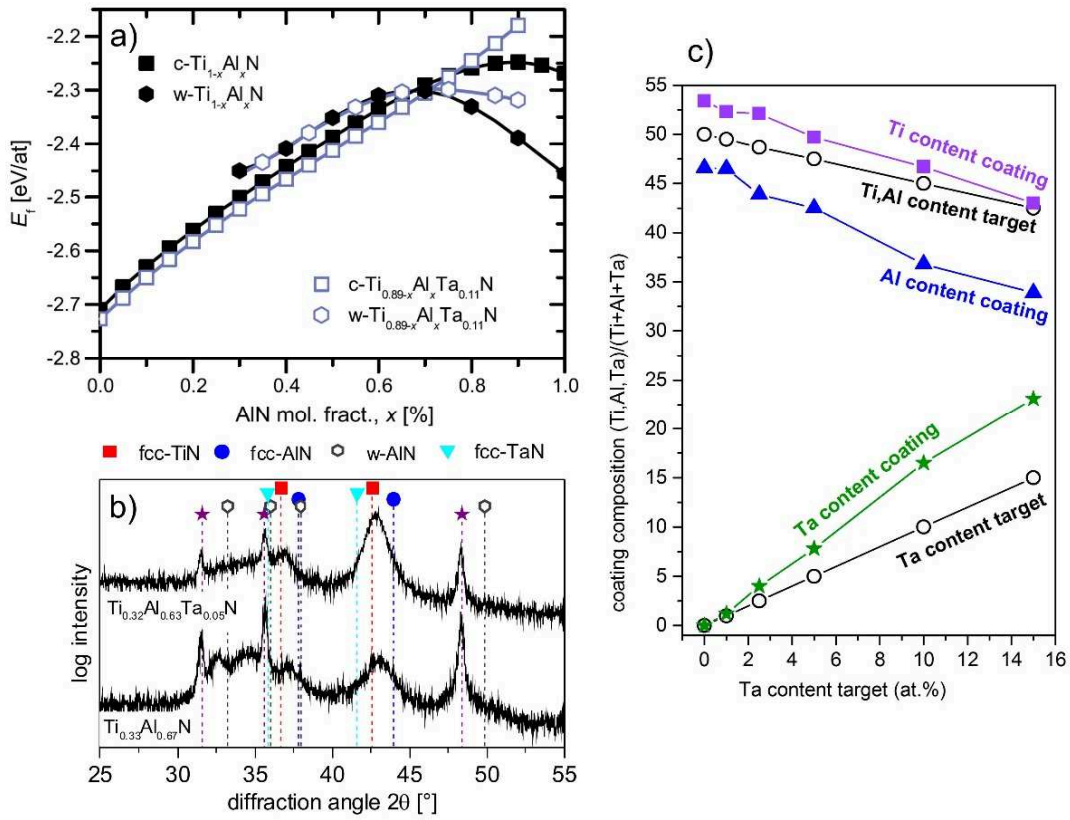

Fig. 10 a) shows the energy of formation for fcc and wurtzite $Ti_{1-x}Al_xN$ and $Ti_{1-x-y}Al_xTa_yN$ phases as a function of the Al content [72], b) highlights the influence of 5 at.-% Ta addition on the microstructure of $Ti_{1-x}Al_xN$ coatings with x=0.67 (target composition). In c) the chemical composition of $Ti_{1-x-y}Al_xTa_yN$ coatings as a function of the Ta content of the target is depicted (both b) and c) represent own work).

Ta addition to the fcc-$Ti_{1-x-y}Al_xTa_yN$ solid solution results in a higher hardness due to increased lattice distortion (see Fig. 11 [72]). Moreover, the thermal stability of $Ti_{1-x-y}Al_xTa_yN$ is significantly increased, as temperature-driven processes like spinodal decomposition and wurtzite phase formation are shifted towards higher temperatures. Rachbauer *et al.* [72] evidenced a temperature increase of 300 °C for the onset of spinodal decomposition of $Ti_{0.42}Al_{0.48}Ta_{0.10}N$ compared to $Ti_{0.51}Al_{0.49}N$ during vacuum annealing. Exceeding the onset temperature of spinodal decomposition, fcc-AlN-enriched and fcc-$Ti_{1-x}Ta_xN$-enriched domains are formed. Age hardening processes influence also the hardness of Ta containing coatings, similar to $Ti_{1-x}Al_xN$, but lead to a less pronounced hardness increase at elevated

temperatures. However, an overall increased hardness level compared to $Ti_{1-x}Al_xN$ up to temperatures >1000 °C can be observed (see Fig. 11 and publication II).

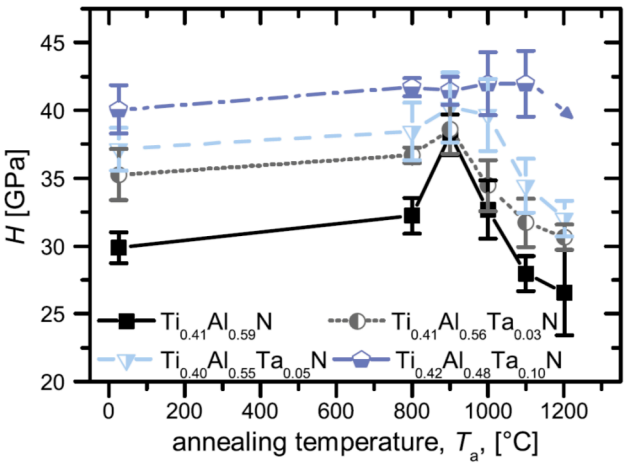

Fig. 11 Hardness evolution versus temperature after annealing of $Ti_{1-x-y}Al_xTa_yN$ coatings with different Ta contents [72].

Ta addition to $Ti_{1-x}Al_xN$ further results in an outstanding oxidation resistance [67,68,75,76]. In $Ti_{1-x}Al_xN$, the limiting factor for further oxidation is the dense Al_2O_3-rich toplayer, while is not sufficiently supported by the TiO_2-rich sublayer exhibiting a low density and therefore enabling diffusion of the oxidation products. In (Ti,Ta)-rich oxides, Ta substitutes Ti in the lattice. Oxygen vacancies are significantly reduced due to the higher ionization state of the pentavalent Ta compared to the quadrivalent Ti. Additionally, Ta suppresses the a-TiO_2 formation during oxidation, as it promotes the early r-TiO_2 formation. Therefore, the densified (Ti,Ta)-rich oxide sublayer contributes to the advanced oxidation resistance of $Ti_{1-x-y}Al_xTa_yN$ coatings, as shown in publication III. As mentioned in section 3.3., the formation of substoichiometric oxides may lead to decreased friction. In r-$(Ti,Ta)O_2$, the Ta^{5+} ions reduce the amount of oxygen vacancies and hence foster the development of substoichiometric Magnéli phases [75]. Therefore, a significantly enhanced tribological behavior up to 900 °C was observed [68].

4. Tribological aspects and machining

4.1. General aspects of cutting processes

For the machining industry, cutting tools for the production of engineering components represent the most important tribological application of coatings. The contact between tool and workpiece during cutting is different to the general tribological contact during sliding and rolling processes. For machining applications, a low friction coefficient and a good abrasive wear resistance at the actual temperatures occurring is favored. The latter is usually provided by hard coatings, since it is strongly related to the coating hardness [13]. A schematic showing the basic contact areas during the cutting process is shown in Fig. 12a.

The high contact temperature during cutting (up to >1000 °C, depending on cutting speed and workpiece material) is mainly caused by the deformation of the chip (~80%), which is affected by the cutting speed and the workpiece material itself [13,77]. The distribution of the energy and therefore the heat is influenced by the cutting speed [77]. Most of the heat (~75%) is dispersed with the chip, while the workpiece material absorbs only ~5%; around 20% of the heat is dissipated through the cutting tool [78]. Additionally to the temperature, a high normal pressure impacts on the rake face. In Fig. 12b, the main wear mechanisms as a function of the cutting speed, and therefore the thermal load, are illustrated. To which extent the mechanisms contribute to the overall wear of the tool (marked as yellow line 'wear') depends on the tribological system consisting of tool material, workpiece material, the potentially applied coolant/lubricant and environmental conditions.

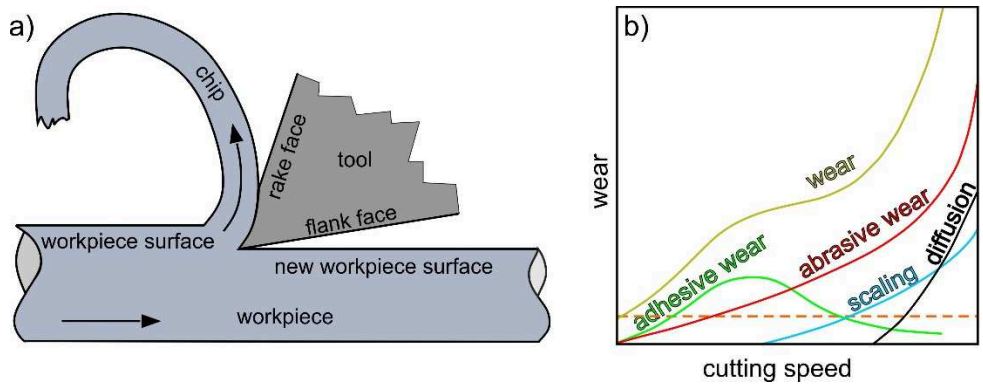

Fig. 12 a) Schematic of a cutting process (after [13]), b) shows the main tool wear mechanisms as a function of the cutting speed (after [79]). The orange dotted line indicates the beginning deformation of the tool edge.

4.2. Wear mechanisms relevant for cutting

The load imposed on the cutting tool during application inevitably determines its lifetime. The main wear mechanisms can be identified as follows [13,77,80]:

Adhesive wear occurs at asperity junctions when tool and chip get locally welded at low cutting speeds. The junctions are immediately destroyed by the acting shear force, which results in material loss. Three forms of **abrasive wear** can occur when hard particles are introduced to the tool surface, i.e., *microploughing, microchipping* and *microcracking*. Abrasive wear has solely mechanical reasons; hard particles remove softer parts of the tool surface. The origin of the particles can be versatile, e.g. a hard phase of the workpiece material (carbides or oxides), or particles released from the build-up edge formed at the rake face. **Tribochemical wear** frequently appears during machining of metals due to the increased temperature, which enables *diffusion wear, oxidative wear and solution wear*. **Delamination wear** is a result of crack formation under the surface, which are induced by cyclic plastic deformation of the surface. With ongoing loading, the cracks start to propagate, leading to fatigue and delamination of coating fragments.

Fig. 13 summarizes the origins of typical wear forms occurring for a cutting insert during machining. Flank wear is formed on the flank face, where the cutting edge

gets into contact with the newly formed surface of the workpiece (see Fig. 13a). At the outer edge of the cut, the formation of a groove or notch can occur, as shown in Fig. 13b. Additionally to the cutting speed, tool lifetime and material combination, the formation of flank wear and notches is also connected to the clearance angle, which is located between the flank face and the new surface [77]. Crater wear occurs at the rake face of the cutting insert. The formation of built-up edges stemming from welded workpiece particles (adhesive wear) on the cutting edge is also unfavored. When the built-up material exceeds a certain volume, it gets ripped down, taking tool particles away [77].

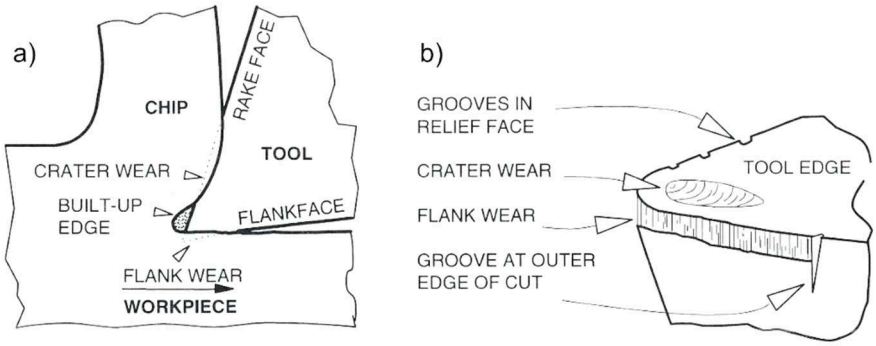

Fig. 13 a) Formation of wear forms on a cutting insert during machining, b) typical wear form on the different surfaces of a cutting insert [13].

In order to evaluate the performance of cutting tools, it is common to conduct cutting tests like milling, turning or drilling. The lifetime criteria is often set as a specific flank wear height. Kathrein *et al.* [71] reported on the wear resistance of multilayer TiAlN/TiAlMN with M=(Ta, V, B) as well as single layer quaternary TiAlMN hard coatings, deposited by cathodic arc evaporation. They found an increased milling lifetime for the single layer TiAlMN compared to the ternary $Ti_{1-x}Al_xN$ coatings, and also higher lifetimes for the tools coated with multilayer coatings. The increased lattice strain level induced by multilayering was associated to an increased hardness, and therefore to reduced wear. In publication I of this thesis, the milling lifetime of $Ti_{1-x}Al_xN$ coatings as a function of the Al content x and the bias voltage was investigated. In analogy to the coatings' hardness, the milling lifetime increased with increasing Al content. Exceeding the solubility limit of AlN

in fcc TiN results in a hardness drop, i.e., for x>0.5, while the cutting performance is at a high level up to x=0.6. Above that limit it drops drastically. Fig. 14 shows pictures of $Ti_{1-x}Al_xN$ coated cemented carbide cutting inserts after turning tests with 100 defined cuts. Fig. 14a depicts a $Ti_{0.53}Al_{0.47}N$ coating, yielding less wear than $Ti_{0.35}Al_{0.65}N$, as shown in Fig. 14b. The more pronounced crater wear of $Ti_{0.35}Al_{0.65}N$ can be explained by the increased wurtzite fraction due to the higher Al content of $Ti_{0.35}Al_{0.65}N$, leading to more pronounced softening due to thermally induced diffusion.

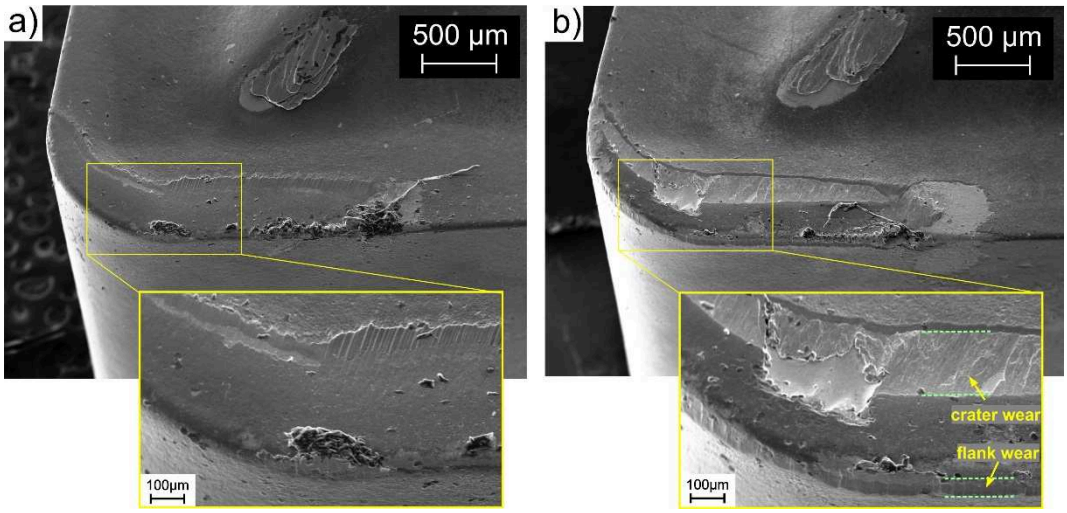

Fig. 14 Effect of increasing Al content on the turning performance of $Ti_{1-x}Al_xN$ coatings after face turning of an X5CrNi18-10 stainless steel for a turning time of 4.68 min a) $Ti_{0.53}Al_{0.47}N$ shows less crater wear than b) the coating containing the higher Al content, i.e., $Ti_{0.35}Al_{0.65}N$ (provided by Markus Pohler/Ceratizit).

It is challenging to compare the coatings by performing cutting tests of the coated tools, and to maintain uniform and reproducible cutting conditions, since many variable parameters are involved; moreover, these tests are considerably time-consuming. Therefore it is common to link results like wear resistance and tool lifetime to tribological properties of the coatings, i.e., friction coefficient and wear rate. The testing of tribological properties of coatings can be performed using simplified conditions reduced to few controllable parameters like temperature, moisture and normal load. Hence, it is a common procedure to extrapolate from e.g. ball-on-disk tests to the cutting performance of coatings.

5. Summary and outlook

In the present thesis, main focus was laid on an experimental study of $Ti_{1-x-y}Al_xTa_yN$ hard coatings, where the effect of varying the Al content, the Ta content as well as deposition conditions on microstructure and properties was investigated. In the following, the thorough study performed on $Ti_{1-x-y}Al_xTa_yN$ coatings leading to the publications inherent to this thesis is summarized with respect to the three main questions mentioned in the introduction of the thesis:

- In the first part of the present study, the main focus was laid on the investigation of different bias voltages applied during growth of $Ti_{1-x}Al_xN$ coatings. The deposition with a higher bias voltage applied to the substrate leads to increased energy of the impinging ions, triggering the generation of new nucleation sites, hence results in formation of more fine-grained coatings. The high bias voltage widens the solubility limit of $Ti_{1-x}Al_xN$ up to higher Al contents, and therefore enables enhanced properties: for high Al contents, the observed lower wurtzite phase fraction leads to increased hardness due to solid solution hardening, while for coatings with a low Al content the increased stress level and the low grain size result in enhanced mechanical and room temperature tribological properties. However, at elevated temperature, the diffusion-driven processes like spinodal decomposition and wurtzite phase formation are enabled considerably faster due to the lower grain size (see publication I).
- The diffusion-driven processes can be shifted towards higher temperatures when a considerable stress level within the coating is present, as it is evidenced by the addition of Ta to $Ti_{1-x}Al_xN$ at constant Al/Ti atomic ratios. Moreover, the resulting lower Al content stabilizes the fcc-$Ti_{1-x-y}Al_xTa_yN$ solid solution and

consequently increases the thermal stability. Considerably higher hardness values compared to $Ti_{1-x}Al_xN$ coatings up to temperatures of 1000 °C were observed (see publication II). However, no unambiguous evidence for age hardening is detectable for Ta contents y>0.08, which is a possible effect of the formation of an additional Ta_2N phase at high Ta contents.

- During thermal annealing in ambient air, the Ta atoms densify the formed porous TiO_2-rich layer, which results in hindered further transport of oxidative agents through the oxide scale. Tribological investigations in ambient air yield a decrease of friction with increasing Ta content, caused by the tribochemical formation of substoichiometric oxides, acting as solid lubricants. Therefore, an increasing Ta content y in $Ti_{1-x-y}Al_xTa_yN$ results in enhanced oxidation resistance and increases the tool lifetime; however, at Ta contents of y≥0.17, a disproportional thick oxide layer develops, which causes again higher friction. The investigation of the different oxide scales (as reported in publication III) contributes fundamentally to our knowledge of the competing processes of oxidation and wear at elevated temperatures.

In summary, the addition of Ta is beneficial up to y~0.08 in $Ti_{1-x-y}Al_xTa_yN$ hard coatings; however, even very small amounts (i.e., y~0.01) yield significant improvements of thermal stability and oxidation resistance.

Future research topics can rely on the further variation of the deposition conditions, especially the investigation of different bias voltages on the growth of Ta containing coatings. An increase of the Al and Ta content in combination with increased bias voltage could further widen the solubility limit of AlN in fcc-$Ti_{1-x-y}Al_xTa_yN$, and lead to enhanced properties at elevated temperatures. Another possible approach is the combination of the advantages of a *low* bias voltage (i.e., the low stress level) with the increased hardness of a coating grown at *high* bias voltage; different bias modulated zones within one coating can hold attractive property combinations. Another possible research topic relies on the development and investigation of $Ti_{1-x-y}Al_xTa_yN$ coatings with a microstructure tailored to withstand the respective wear form occurring during the respective cutting test, for

example compositionally, microstructurally and/or stress modulated multilayers with enhanced thermal stability and fracture toughness, which could lead to peak performances for severe applications.

References

[1] M.N. Gardos, Magnéli phases of anion-deficient rutile as lubricious oxides. Part I. Tribological behavior of single-crystal and polycrystalline rutile (Ti_nO_{2n-1}), Tribol Lett 8 (2000) 65–78.

[2] H. Çalişkan, P. Panjan, S. Paskvale, Monitoring of wear characteristics of TiN and TiAlN coatings at long sliding distances, Tribol. Trans. 57 (2014) 496–502.

[3] W.-D. Münz, Titanium aluminum nitride films: A new alternative to TiN coatings, J. Vac. Sci. Technol. A 4 (1986) 2717.

[4] O. Knotek, W.D. Münz, T. Leyendecker, Industrial deposition of binary, ternary, and quaternary nitrides of titanium, zirconium, and aluminum, J. Vac. Sci. Technol. A 5 (1987) 2173–2179.

[5] H. Randhawa, P.C. Johnson, R. Cunningham, Deposition and characterization of ternary nitrides, J. Vac. Sci. Technol. A 6 (1988) 2136–2139.

[6] S. Ruppi, A. Larsson, A. Flink, Nanoindentation hardness, texture and microstructure of α-Al_2O_3 and κ-Al_2O_3 coatings, Thin Solid Films 516 (2008) 5959–5966.

[7] D. Hochauer, C. Mitterer, M. Penoy, C. Michotte, H.P. Martinz, M. Kathrein, Thermal stability of doped CVD κ-Al_2O_3 coatings, Surf. Coat. Technol. 204 (2010) 3713–3722.

[8] F. Vaz, L. Rebouta, M. Andritschky, da Silva, M. F., J.C. Soares, Thermal oxidation of $Ti_{1-x}Al_xN$ coatings in air, ECerS 17 (1997) 1971–1977.

[9] D. McIntyre, J.E. Greene, G. Håkansson, J.-E. Sundgren, W.-D. Münz, Oxidation of metastable single-phase polycrystalline $Ti_{0.5}Al_{0.5}N$ films: Kinetics and mechanisms, J. Appl. Phys. 67 (1990) 1542.

[10] P.H. Mayrhofer, A. Hörling, L. Karlsson, J. Sjölén, T. Larsson, C. Mitterer, L. Hultman, Self-organized nanostructures in the Ti–Al–N system, Appl. Phys. Lett. 83 (2003) 2049.

[11] P.H. Mayrhofer, L. Hultman, J.M. Schneider, P. Staron, H. Clemens, Spinodal decomposition of cubic $Ti_{1-x}Al_xN$: Comparison between experiments and modeling, IJMR 98 (2007) 1054–1059.

[12] P.H. Mayrhofer, R. Rachbauer, D. Holec, F. Rovere, J.M. Schneider, in: Comprehensive Materials Processing, Elsevier, 2014, pp. 355–388.

[13] K. Holmberg, A. Matthews, Coatings tribology: Properties, techniques and applications in surface engineering, Tribology series 28, Elsevier, Amsterdam, 1994.

[14] R.A. Haefer, Oberflächen- und Dünnschicht-Technologie: Teil 1: Beschichtung von Oberflächen, Springer, Berlin, Heidelberg, 1987.

[15] M. Ohring, Materials science of thin films: Deposition & structure, 2nd ed., Academic press, San Diego, 2002.

[16] H.E. Rebenne, D.G. Bhat, Review of CVD TiN coatings for wear-resistant applications, Surf. Coat. Technol. 63 (1994) 1–13.

[17] J. Wagner, C. Mitterer, M. Penoy, C. Michotte, W. Wallgram, M. Kathrein, The effect of deposition temperature on microstructure and properties of thermal CVD TiN coatings, Int. J. Refract. Met. Hard Mater. 26 (2008) 120–126.

[18] R.F. Bunshah, Deposition technologies for films and coatings: Developments and applications, Materials science series, Noyes Publications, New Jersey, 1982.

[19] J. Zalesak, J. Todt, R. Pitonak, A. Köpf, R. Weißenbacher, B. Sartory, M. Burghammer, R. Daniel, J. Keckes, Combinatorial refinement of thin-film microstructure, properties and process conditions, J Appl Crystallogr 49 (2016) 2217–2225.

[20] J. Todt, J. Zalesak, R. Daniel, R. Pitonak, A. Köpf, R. Weißenbacher, B. Sartory, C. Mitterer, J. Keckes, Al-rich cubic $Al_{0.8}Ti_{0.2}N$ coating with self-organized nano-lamellar microstructure, Surf. Coat. Technol. 291 (2016) 89–93.

[21] J. Todt, R. Pitonak, A. Köpf, R. Weißenbacher, B. Sartory, M. Burghammer, R. Daniel, T. Schöberl, J. Keckes, Superior oxidation resistance, mechanical properties and residual stresses of an Al-rich nanolamellar $Ti_{0.05}Al_{0.95}N$ coating prepared by CVD, Surf. Coat. Technol. 258 (2014) 1119–1127.

[22] M. Tkadletz, C. Mitterer, B. Sartory, I. Letofsky-Papst, C. Czettl, C. Michotte, The effect of droplets in arc evaporated TiAlTaN hard coatings on the wear behavior, Surf. Coat. Technol. 257 (2014) 95–101.

[23] B.F. Coll, D.M. Sanders, Design of vacuum arc-based sources, Surf. Coat. Technol. (1996) 42–51.

[24] D.M. Sanders, A. Anders, Review of cathodic arc deposition technology at the start of the new millennium, Surf. Coat. Technol. 133-134 (2000) 78–90.

[25] I. Petrov, P. Losbichler, D. Bergstrom, J.E. Greene, W.-D. Münz, T. Hurkmans, T. Trinh, Ion-assisted growth of $Ti_{1-x}Al_xN/Ti_{1-y}Nb_yN$ multilayers by combined cathodic-arc/magnetron-sputter deposition, Thin Solid Films 302 (1997) 179–192.

[26] B.A. Movchan, A.V. Demchishin, Study of the structure and properties of thick vacuum condensates of nickel, titanium, tungsten, aluminium oxide and zirconium dioxide, Fiz.metal.metalloved., 28 (1969) 653–660.

[27] J.A. Thornton, Influence of substrate temperature and deposition rate on structure of thick sputtered Cu coatings, J. Vac. Sci. Technol. (1975) 830–835.

[28] R. Messier, A.P. Giri, R.A. Roy, Revised structure zone model for thin film physical structure, J. Vac. Sci. Technol. A 2 (1984) 500–503.

[29] A. Anders, A structure zone diagram including plasma-based deposition and ion etching, Thin Solid Films 518 (2010) 4087–4090.

[30] G. Kienel, Vakuumbeschichtung: Anwendungen Teil 1 24, VDI, Düsseldorf, 1993.

[31] H. Holleck, Metastable coatings - Prediction of composition and structure, Surf. Coat. Technol. 1988 (36) 151–159.

[32] R. Cremer, M. Witthaut, D. Neuschütz, Experimental determintation of the metastable (Ti,Al)N diagram up to 700 deg C, Value-Addition Metallurgy (1998) 249–258.

[33] D. Holec, R. Rachbauer, L. Chen, L. Wang, D. Luef, P.H. Mayrhofer, Phase stability and alloy-related trends in Ti–Al–N, Zr–Al–N and Hf–Al–N systems from first principles, Surf. Coat. Technol. 206 (2011) 1698–1704.

[34] M. Kawate, A. Kimura, T. Suzuki, Microhardness and lattice parameter of $Cr_{1-x}Al_xN$ films, J. Vac. Sci. Technol. A 20 (2002) 569–571.

[35] A. Kimura, H. Hasegawa, K. Yamada, T. Suzuki, Effects of Al content on hardness, lattice parameter and microstructure of $Ti_{1-x}Al_xN$ films, Surf. Coat. Technol. 120-121 (1999) 438–441.

[36] P.H. Mayrhofer, D. Music, J.M. Schneider, Influence of the Al distribution on the structure, elastic properties, and phase stability of supersaturated $Ti_{1-x}Al_xN$, J. Appl. Phys. 100 (2006) 94906.

[37] S. PalDey, S. Deevi, Single layer and multilayer wear resistant coatings of (Ti,Al)N: a review, Mat. Sci. Eng. A 342 (2003) 58–79.

[38] M. Zhou, Y. Makino, M. Nose, K. Nogi, Phase transition and properties of Ti–Al–N thin films prepared by r.f.-plasma assisted magnetron sputtering, Thin Solid Films 339 (1999) 203–208.

[39] A. Hörling, L. Hultman, M. Odén, J. Sjölén, L. Karlsson, Mechanical properties and machining performance of $Ti_{1-x}Al_xN$-coated cutting tools, Surf. Coat. Technol. 191 (2005) 384–392.

[40] G. Greczynski, J. Lu, M.P. Johansson, J. Jensen, I. Petrov, J.E. Greene, L. Hultman, Role of Ti^{n+} and Al^{n+} ion irradiation (n=1, 2) during $Ti_{1-x}Al_xN$ alloy film growth in a hybrid HIPIMS/magnetron mode, Surf. Coat. Technol. 206 (2012) 4202–4211.

[41] K. Kutschej, P.H. Mayrhofer, M. Kathrein, P. Polcik, R. Tessadri, C. Mitterer, Structure, mechanical and tribological properties of sputtered $Ti_{1-x}Al_xN$ coatings with $0.5 \leq x \leq 0.75$, Surf. Coat. Technol. 200 (2005) 2358–2365.

[42] C. Wüstefeld, D. Rafaja, V. Klemm, C. Michotte, M. Kathrein, Effect of the aluminium content and the bias voltage on the microstructure formation in $Ti_{1-x}Al_xN$ protective coatings grown by cathodic arc evaporation, Surf. Coat. Technol. 205 (2010) 1345–1349.

[43] C. Wüstefeld, D. Rafaja, M. Dopita, M. Motylenko, C. Baehtz, C. Michotte, M. Kathrein, Decomposition kinetics in $Ti_{1-x}Al_xN$ coatings as studied by in-situ X-ray diffraction during annealing, Surf. Coat. Technol. 206 (2011) 1727–1734.

[44] M. Hans, D. Music, Y.-T. Chen, L. Patterer, A.O. Eriksson, D. Kurapov, J. Ramm, M. Arndt, H. Rudigier, J.M. Schneider, Crystallite size-dependent metastable phase formation of TiAlN coatings, SCI REP UK 7 (2017) 16096.

[45] K. Sato, N. Ichimiya, A. Kondo, Y. Tanaka, Microstructure and mechanical properties of cathodic arc ion-plated (Al,Ti)N coatings, Surf. Coat. Technol. 163-164 (2003) 135–143.

[46] D. Rafaja, C. Wüstefeld, C. Baehtz, V. Klemm, M. Dopita, M. Motylenko, C. Michotte, M. Kathrein, Effect of internal interfaces on hardness and thermal stability of nanocrystalline $Ti_{0.5}Al_{0.5}N$ coatings, Metall and Mat Trans A 42 (2011) 559–569.

[47] P.H. Mayrhofer, F.D. Fischer, H.J. Böhm, C. Mitterer, J.M. Schneider, Energetic balance and kinetics for the decomposition of supersaturated $Ti_{1-x}Al_xN$, Acta Mater. 55 (2007) 1441–1446.

[48] B. Grossmann, N. Schalk, C. Czettl, M. Pohler, C. Mitterer, Phase composition and thermal stability of arc evaporated $Ti_{1-x}Al_xN$ hard coatings with $0.4 \leq x \leq 0.67$, Surf. Coat. Technol. 309 (2017) 687–693.

[49] J. Zhou, J. Zhong, L. Chen, L. Zhang, Y. Du, Z.-K. Liu, P.H. Mayrhofer, Phase equilibria, thermodynamics and microstructure simulation of metastable spinodal decomposition in c–$Ti_{1-x}Al_xN$ coatings, Calphad 56 (2017) 92–101.

[50] R. Rachbauer, E. Stergar, S. Massl, M. Moser, P.H. Mayrhofer, Three-dimensional atom probe investigations of Ti–Al–N thin films, Scr. Mater. 61 (2009) 725–728.

[51] R. Hollerweger, H. Riedl, J. Paulitsch, M. Arndt, R. Rachbauer, P. Polcik, S. Primig, P.H. Mayrhofer, Origin of high temperature oxidation resistance of Ti–Al–Ta–N coatings, Surf. Coat. Technol. 257 (2014) 78–86.

[52] A. Hörling, L. Hultman, M. Odén, J. Sjölén, L. Karlsson, Thermal stability of arc evaporated high aluminum-content $Ti_{1-x}Al_xN$ thin films, J. Vac. Sci. Technol. A 20 (2002) 1815.

[53] L. Chen, Y. Du, P.H. Mayrhofer, S.Q. Wang, J. Li, The influence of age-hardening on turning and milling performance of Ti–Al–N coated inserts, Surf. Coat. Technol. 202 (2008) 5158–5161.

[54] N. Birks, G.H. Meier, F.S. Pettit (Eds.), Introduction to the high-temperature oxidation of metals, 2nd ed., Cambridge Univ. Press, Cambridge, 2009.

[55] R.D. Shannon, J.A. Pask, Kinetics of the Anatase-Rutile Transformation, ACerS 48 (1965) 391–398.

[56] D.A.H. Hanaor, C.C. Sorrell, Review of the anatase to rutile phase transformation, J Mater Sci 46 (2011) 855–874.

[57] H.J. Rösler, Lehrbuch der Mineralogie, 5th ed., p. 399, Deutscher Verlag für Grundstoffindustrie, Leipzig, 1991.

[58] M. Pfeiler, G.A. Fontalvo, J. Wagner, K. Kutschej, M. Penoy, C. Michotte, C. Mitterer, M. Kathrein, Arc evaporation of Ti–Al–Ta–N coatings: The effect of bias voltage and Ta on high-temperature tribological properties, Tribol Lett 30 (2008) 91–97.

[59] A. Erdemir, A crystal-chemical approach to lubrication by solid oxides, Tribol Lett 8 (2000) 97–102.

[60] M.N. Gardos, The effect of anion vacancies on the tribological properties of rutile (TiO_{2-x}), Tribol. Trans. 31 (1988) 427–436.

[61] A. Magnéli, Structures of the ReO_3-type with recurrent dislocations of atoms: 'Homologous series' of molybdenum and tungsten oxides, Acta Cryst. 6 (1953) 495.

[62] A. Magnéli, G. Andersson, On the MoO_2 Structure Type, Acta Chem. Scand. 9 (1955) 1378–1381.

[63] M. Woydt, Tribological characteristics of polycrystalline Magnéli-type titanium dioxides, Tribol Lett 8 (2000) 117–130.

[64] M.N. Gardos, H.-S. Hong, W.O. Winer, The effect of anion vacancies on the tribological properties of rutile (TiO_{2-x}), Part II: Experimental evidence, Tribol. Trans. 33 (1990) 209–220.

[65] Y. Shimizu, E. Iguchi, Theory of the elastic strain energy due to crystallographic shear plane arrays in reduced rutile (Ti O2), Phys. Rev. B 17 (1978) 2505–2517.

[66] C.M. Koller, R. Hollerweger, C. Sabitzer, R. Rachbauer, S. Kolozsvári, J. Paulitsch, P.H. Mayrhofer, Thermal stability and oxidation resistance of arc evaporated TiAlN, TaAlN, TiAlTaN, and TiAlN/TaAlN coatings, Surf. Coat. Technol. 259 (2014) 599–607.

[67] V. Khetan, N. Valle, D. Duday, C. Michotte, M.-P. Delplancke-Ogletree, P. Choquet, Influence of temperature on oxidation mechanisms of fiber-textured AlTiTaN coatings, ACS Appl. Mater. Interfaces 6 (2014) 4115–4125.

[68] V. Khetan, N. Valle, D. Duday, C. Michotte, C. Mitterer, M.-P. Delplancke-Ogletree, P. Choquet, Temperature-dependent wear mechanisms for magnetron-sputtered AlTiTaN hard coatings, ACS Appl. Mater. Interfaces 6 (2014) 15403–15411.

[69] K. Kutschej, P.H. Mayrhofer, M. Kathrein, P. Polcik, C. Mitterer, Influence of oxide phase formation on the tribological behaviour of Ti–Al–V–N coatings, Surf. Coat. Technol. 200 (2005) 1731–1737.

[70] K. Kutschej, P.H. Mayrhofer, M. Kathrein, C. Michotte, P. Polcik, C. Mitterer, Multi-functional multi-component $Ti_{1-x}Al_xN$ based coatings, Plansee Seminar Proc. 16th Int. Plansee Seminar, Plansee, Reutte (2005) 774.

[71] M. Kathrein, C. Michotte, M. Penoy, P. Polcik, C. Mitterer, Multifunctional multi-component PVD coatings for cutting tools, Surf. Coat. Technol. 200 (2005) 1867–1871.

[72] R. Rachbauer, D. Holec, P.H. Mayrhofer, Increased thermal stability of Ti–Al–N thin films by Ta alloying, Surf. Coat. Technol. 211 (2012) 98–103.

[73] D.-Y. Wang, Y.-W. Li, W.-Y. Ho, Deposition of high quality (Ti,Al)N hard coatings by vacuum arc evaporation process, Surf. Coat. Technol. 114 (1999) 109–113.

[74] W.D. Davis, H.C. Miller, Analysis of the electrode products emitted by dc arcs in a vacuum ambient, Journal of Applied Physics 40 (1969) 2212–2221.

[75] R.G. Reddy, Y. Li, M.F. Arenas, Oxidation of a Ternary Ti_3Al-Ta Alloy, High Temp. Mater. Process. 21 (2002) 195–206.

[76] M. Mikula, M. Truchlý, D.G. Sangiovanni, D. Plašienka, T. Roch, M. Gregor, P. Ďurina, M. Janík, P. Kúš, Experimental and computational studies on toughness enhancement in Ti-Al-Ta-N quaternaries, J. Vac. Sci. Technol. A 35 (2017) 60602.

[77] B. Denkena, H.K. Tönshoff, Spanen, Springer, Berlin, Heidelberg, 2011.

[78] B. Lux, C. Colombier, H. Altena, K. Stjernberg, Preparation of alumina coatings by chemical vapour deposition, Thin Solid Films 138 (1986) 49–64.

[79] G. Vieregge, Zerspanung der Eisenwerkstoffe, 2nd ed., Stahleisen M.B.H, Düsseldorf, 1970.

[80] D.F. Moore, Principles and applications of tribology, 1st ed., International series on materials science and technology, v. 14, Pergamon Press, Oxford, New York, 1975.

6. Publications

6.1. Included publications

Phase composition and thermal stability of arc evaporated $Ti_{1-x}Al_xN$ hard coatings with $0.4 \leq x \leq 0.67$

Surface & Coatings Technology 309 (2017) 687-693

Birgit Grossmann, Nina Schalk, Christoph Czettl, Markus Pohler, Christian Mitterer

Tailoring age hardening of $Ti_{1-x}Al_xN$ by Ta alloying

Journal of Vacuum Science & Technology
A: Vacuum, Surfaces and Films 35, 060604 (2017)

Birgit Grossmann, Andreas Jamnig, Nina Schalk, Christoph Czettl, Markus Pohler, Christian Mitterer

High-temperature tribology and oxidation of $Ti_{1-x-y}Al_xTa_yN$ hard coatings

Surface & Coatings Technology, in press, DOI:
10.1016/j.surfcoat.2018.02.062

Birgit Grossmann, Michael Tkadletz, Nina Schalk, Christoph Czettl, Markus Pohler, Christian Mitterer

6.2. Further work contributing to this thesis:

Influence of the Ta content on microstructure, properties and thermal stability of arc evaporated $Ti_{1-x-y}Al_xTa_yN$ hard coatings

Proceedings of the 19th International Plansee Seminar, Reutte 2017

Birgit Grossmann, Michael Tkadletz, Nina Schalk, Christoph Czettl, Markus Pohler, Andreas Jamnig, Christian Mitterer

Influence of Ta on the thermal stability of $Ti_{1-x}Al_xN$ hard coatings deposited with different bias voltages

co-supervised diploma thesis, written by Andreas Jamnig, Montanuniversität Leoben, 2016

Tribological investigations of TiAlN coatings alloyed with Ta at 700 °C

co-supervised bachelor thesis, written by Thaddäa Rath, Montanuniversität Leoben, 2016

6.3. Other publications:

Few-step synthesis, thermal purification and structural characterization of porous boron nitride nanoplatelets

Nikolaos Kostoglou, Jelena Luković, Biljana Babić, Branko Matović, Demetris Photiou, Georgios Constantinides, Kiriaki Polychronopoulou, Vladislav Ryzhkov, Birgit Grossmann, Christian Mitterer, Claus Rebholz

Publication I

Phase composition and thermal stability of arc evaporated $Ti_{1-x}Al_xN$ hard coatings with $0.4 \leq x \leq 0.67$

Surface & Coatings Technology 309 (2017) 687-693

by

Birgit Grossmann[1*], Nina Schalk[1], Christoph Czettl[2], Markus Pohler[2], Christian Mitterer[1]

1. Introduction

Outstanding cutting performance and extended service lifetime of cutting tools are required to fulfill industrial demands. $Ti_{1-x}Al_xN$ hard coatings are widely applied to meet these requirements; therefore, they are in the focus of many investigations [1-32]. There are several advantages of the $Ti_{1-x}Al_xN$ coating system over binary TiN coatings, like enhanced mechanical properties [1-4] and the formation of a protective Al_2O_3 layer at elevated temperatures, which results in an enhanced oxidation resistance [5,6]. Using physical vapor deposition, the synthesis of metastable single-phase face-centered cubic (fcc) $Ti_{1-x}Al_xN$ is possible up to Al contents of x~0.67 by substituting the Ti by Al atoms in the fcc-TiN lattice. The maximum hardness for fcc-$Ti_{1-x}Al_xN$ was found at x~0.5-0.6 [1,2,7]. However, if the Al content exceeds the solubility limit, the wurtzite structure is formed, resulting in a deterioration of the mechanical properties when a significant fraction of wurtzite is present [1-4,8]. At elevated temperatures, the metastable fcc-$Ti_{1-x}Al_xN$ phase undergoes spinodal decomposition into fcc-AlN and fcc-TiN, which leads to a further increase of the hardness due to age hardening [3,4,9,10]. Increasing the temperature above ~900 °C causes a transformation of the metastable fcc-AlN into the stable wurtzite phase, which results in a hardness drop [3,9]. In addition to the Al content, also the deposition parameters, in particular the bias voltage, have a considerable influence on the microstructure and thus, also on the phase composition and decomposition kinetics of $Ti_{1-x}Al_xN$ coatings at elevated temperatures [2,11,12]. According to Wüstefeld *et al.* [2], the appearance of wurtzite phase fractions in arc evaporated $Ti_{1-x}Al_xN$ coatings can be shifted to higher Al contents by increasing the negative bias voltage. In another work [11], they showed that a higher bias voltage promotes the onset of the formation of the wurtzite phase during annealing. Within these investigations [2,11], Wüstefeld *et al.* concentrated on the microstructural evolution of $Ti_{1-x}Al_xN$ coatings with varying Al contents grown at different bias voltages.

The aim of the present work is to establish a relationship between the microstructure and thermal stability of $Ti_{1-x}Al_xN$ coatings grown with different Al

contents and bias voltages, and their tribological and application behavior. Thus, $Ti_{1-x}Al_xN$ coatings were deposited by cathodic arc evaporation using four different target compositions and two different bias voltages. The elemental composition and microstructure were examined using energy dispersive X-ray spectroscopy (EDX) and X-ray diffraction (XRD), respectively. Nanoindentation was used for the determination of the mechanical properties. In order to study the tribological properties, ball-on-disk tests were performed and in addition cutting tests were done. The thermal stability was investigated using differential scanning calorimetry (DSC).

2. Experimental Methods

Utilizing an industrial scale Oerlikon Balzers Innova cathodic arc evaporation system, eight coatings were deposited from powder metallurgical TiAl targets with four different compositions and using two different bias voltages V_B (-40 and -100 V), following procedures described in more detail in earlier papers [13-16]. Hereinafter, we will refer to coatings of the series 'V_B = -40 V' and 'V_B = -100 V'. Targets with Ti/Al atomic ratios of 60/40, 50/50, 40/60 and 33/67, respectively, were used. The coatings were grown in a pure N_2 atmosphere on polished cemented carbide (CC) disks (∅ 30 mm × 4 mm), CC cutting inserts in SNUN 120312EN-, SEKW 1204AFSN-, and XDKT 11T308SR-F50-geometry (according to ISO 1832), and a low alloy steel foil. The composition of the CC SNUN was 92 wt% tungsten carbide, 6 wt% cobalt and 2 wt% mixed carbides, while the CC discs consist of 77 wt% tungsten carbide, 11 wt% cobalt and 12 wt% mixed carbides. 2-fold rotation was applied for coating the disks and steel foil, while all other substrates were mounted on a substrate holder to undergo 3-fold rotation. The deposition time was adjusted to reach a thickness of 5±1 µm for all coatings. Prior to deposition, the substrates were sputter-etched in a pure Ar plasma.

The coating thickness was determined for all coatings on the SNUN substrates by means of the ball cratering technique using a CSM Instruments CaloWear device. The elemental composition of the coatings was measured by EDX using an Oxford Instruments INCA extension in a Zeiss EVO50 scanning electron

microscope (SEM) and built-in sensitivity factors for quantification. The SEM was also used for surface examination of the coated SNUN samples. The microstructure of the as deposited coatings grown on SNUN substrates was investigated using XRD in gracing incidence geometry (incidence angle 2°) utilizing Cu Kα radiation with $\lambda = 0.154$ nm in a Bruker-AXS D8 Advance diffractometer, equipped with a Sol-X-Detector. For the determination of the coating hardness, a UMIS (Ultra Micro Indentation System) nanoindenter from Fischer-Cripps Laboratories equipped with a Berkovich tip was applied. As the coatings exhibited typically for arc evaporated coatings a quite rough surface [17], the samples were diamond polished prior to the hardness measurements. Plateau tests with an applied force decreasing from 30 to 10 mN in steps of 0.5 mN were performed to determine reliable hardness values without significant contribution of the softer substrate and the indentation size effect [18,19]. To obtain information about the tribological properties, the coated disks were tested in ambient air (humidity 33±2%) at room temperature (RT) and at 700 °C using a CSM Instruments ball-on-disk tribometer. Al_2O_3 balls with a diameter of 6 mm were used as counterparts. A normal load of 5 N and a sliding speed of 10 cm/s were applied and the sliding distance was set to 300 m. Utilizing an optical white light interferometer (Veeco Wyko NT1000), the abraded coating volume was determined to calculate the wear rate of the respective coatings. In addition, two different milling tests were performed: face milling, using SEKW cutting inserts, and shoulder milling, using XDKT cutting inserts. Both application tests were carried out in dry condition. As workpiece material, a low carbon streel (SP300, a Superplast® 300® prehardened plastic mold steel from INDUSTEEL) was used. In case of the shoulder milling test, a working angle of 90°, a cutting speed (v_c) of 100 m/min, and a feed rate per tooth (f_z) of 0.15 mm/rot were used, while in face milling the following conditions were applied: working angle = 45°, $v_c = 250$ m/min, $f_z = 0.25$ mm/rot. The end of lifetime for both tests was defined at a flank wear of 0.3 mm, or fracture.

In order to investigate the thermal stability, DSC measurements of the powdered coatings were performed utilizing a Setaram Labsys Evo 2400 DSC. The powder was obtained by chemically dissolving the steel foil substrates in 13% nitric

acid, and subsequent grinding. During the DSC measurements, the chamber was purged with Ar. A heating rate of 23 K/min was applied, and the cooling rate was set to 20 K/min. With the obtained DSC signals, temperatures for annealing treatments were selected in order to investigate the main partial reactions. The annealing treatments were performed in a high vacuum furnace (HTM Reetz, base pressure $<5\times10^{-4}$ Pa), with a heating rate of 20 K/min, a holding time of 15 min and a system dependent cooling rate. Subsequently, the powders were investigated using the same Bruker-AXS D8 Advance diffractometer as above in Θ-2Θ geometry.

3. Results

3.1. As deposited coatings

Fig. 1 shows the elemental composition of the coatings measured by EDX as a function of the target composition. The Al/(Al+Ti) atomic ratio in the coatings deposited with V_B = -40 V is slightly (~4%) lower than in the respective targets, while in the coatings grown at V_B = -100 V the Al/(Al+Ti) content is marginally (~1%) higher than in the respective targets. All coatings contain 50±2 at% nitrogen.

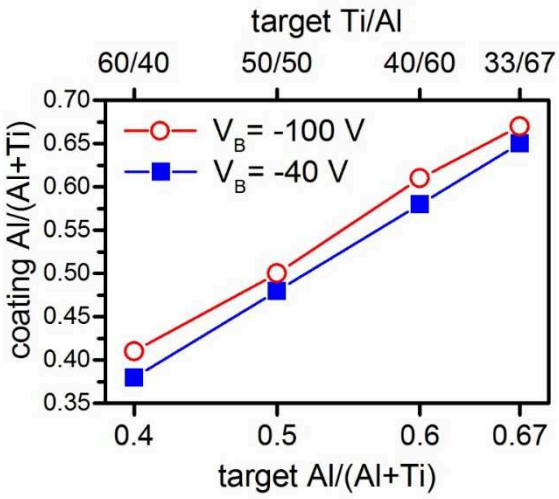

Fig. 1 Elemental composition of the $Ti_{1-x}Al_xN$ coatings as a function of the Al content.

The XRD patterns of the as deposited coatings grown at V_B = -40 V and V_B = -100 V are presented in Figs. 2a and b, respectively, from bottom to top with increasing Al content. The standard peak positions for fcc-TiN (ICDD 00-038-1420)

and fcc-AlN (ICDD 00-025-1495) as well as wurtzite AlN (ICDD 01-076-0702) are added as dashed lines. A single-phase fcc-$Ti_{1-x}Al_xN$ solid solution can be observed for the coatings with Al/(Al+Ti) ≤ 0.5, irrespective of V_B. At higher Al contents (target composition Ti/Al 40/60 and 33/67), the coatings show a dual-phase structure, where the wurtzite phase fractions are more pronounced for those deposited with the lower bias voltage (Fig. 2a). Wüstefeld *et al.* [2]also observed wurtzite phase fractions already at lower Al contents for coatings deposited at a lower bias voltage (i.e. below -40 V) than for coatings grown at higher bias voltage (i.e. above -80 V).

In addition, the peaks of the coatings deposited at V_B = -100 V are significantly broader, indicating a lower crystallite size due to the higher kinetic energy of the impinging ions [20] and/or higher microstrain as a result of the higher bias voltage [21,22].

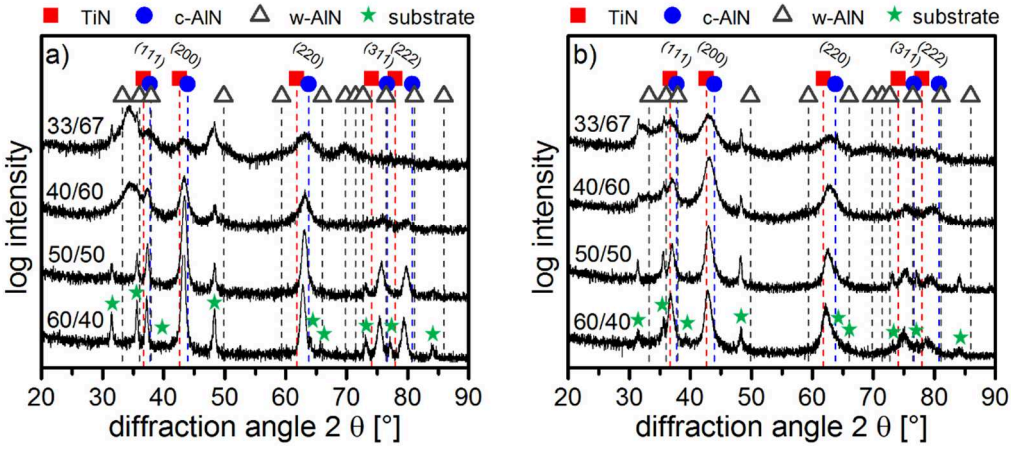

Fig. 2 X-ray diffractograms of the $Ti_{1-x}Al_xN$ coatings grown at a) VB = -40 V and at b) VB = -100 V.

Compared to the coatings deposited at the lower bias voltage Fig. 2a), the peaks observed for the coatings grown at the higher bias voltage (Fig. 2b) are slightly shifted to lower diffraction angles. This is in good agreement with literature [12,23] and indicates compressive residual stresses.

The hardness of the $Ti_{1-x}Al_xN$ coatings as a function of the Al content is shown in Fig. 3 for both bias series. The coatings grown at V_B = -100 V show a significantly higher hardness than those grown at V_B = -40 V. The maximum

hardness with ~34 GPa was determined for the coatings deposited from the targets with the Ti/Al-ratios of 60/40 and 50/50. The significant hardness increase associated with the higher bias voltage can be attributed to the smaller crystallite size and higher defect density, which is a result of the more intense ion bombardment [24,25]. With increasing Al content, the hardness decreases for both bias series, which can be related to increasing wurtzite phase fractions (Figs. 2a and b). This trend correlates well with previous investigations on arc evaporated [2] and also sputtered [26] $Ti_{1-x}Al_xN$ films.

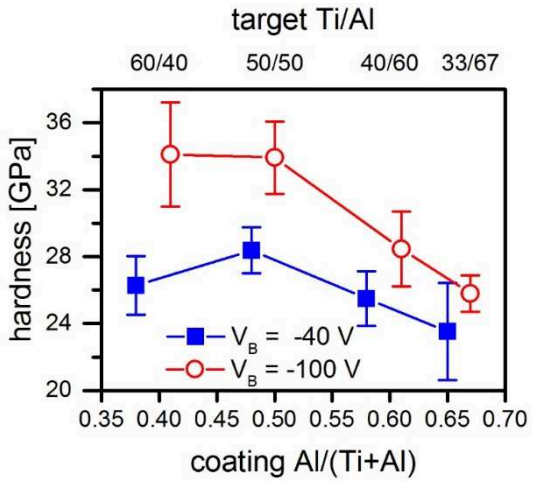

Fig. 3 Hardness of the $Ti_{1-x}Al_xN$ coatings as a function of the Al content.

For the determination of friction coefficient and wear rate, ball-on-disk tests were performed at RT and at 700 °C. The friction coefficients determined at RT and 700 °C for the coating series deposited at V_B = -40 V and V_B = -100 V are shown in Fig.4a and b. Independent from the bias voltage, the friction coefficient of the coatings tested at RT is not significantly affected by the Al content, except for the highest Al-containing coatings, which show a significantly lower friction coefficient.

The friction coefficients of the coatings deposited at V_B = -100 V (Fig. 4b) are slightly higher than those of the coatings grown at V_B = -40 V (Fig. 4a). This can be related to both their higher hardness (Fig. 3), making velocity accommodation in the sliding contact more difficult [27], and the higher droplet density observed by SEM for the coatings deposited at V_B = -100 V due to the reduced growth rate. At

700 °C, the friction coefficient is considerably lower than at RT, most probably stemming from the formation of a protective Al_2O_3-rich top layer [6,26]. The decrease of the friction coefficient with increasing Al content (Fig. 4a) is also an indication for this Al_2O_3-rich top layer. However, at 700°C the lowest friction coefficient is observed for the coatings with the lowest Al content, where the fraction of the softer rutile TiO_2 phase in the oxide scale becomes more important [13,28].

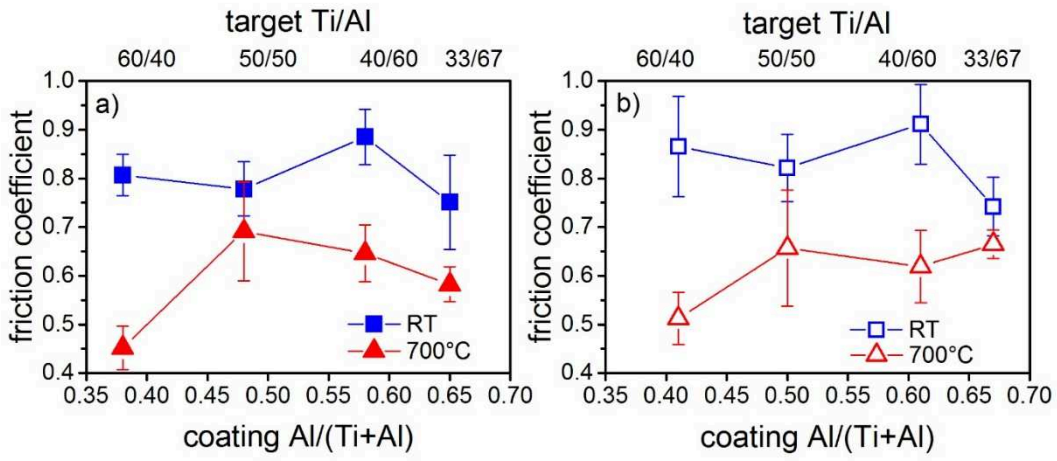

Fig. 4 Friction coefficient of the $Ti_{1-x}Al_xN$ coatings grown at a) VB = -40 V, and b) VB = -100 V as a function of the Al content.

In Figs. 5a and b, the wear rates determined after ball-on-disk tests at RT and 700 °C of the coatings grown at V_B = -40 V and V_B = -100 V, respectively, as a function of the Al content are presented. The coatings with the single-phase fcc-structure (target composition 60/40 and 50/50 for both bias voltages) show the lowest wear rates at RT. With increasing Al content and the existence of a dual-phase structure, the wear rate increases. This increase is even more pronounced for the coatings deposited at V_B = -100 V (Fig. 5b).

The wear rates of both bias series correlate in general well with the hardness measurements, being in good agreement with the notion of abrasion as the dominating wear mechanism at RT [29]. This is most pronounced for the highest Al containing coating at V_B = -100 V, where the observed higher droplet density results in rapid wear of the less hard dual-phase coating [17].

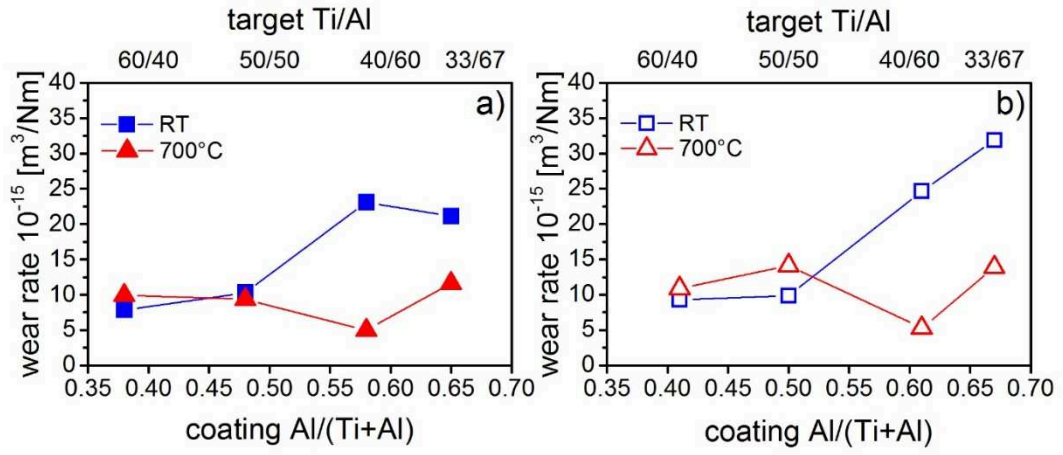

Fig. 5 Wear rate of the $Ti_{1-x}Al_xN$ coatings grown at a) VB = -40 V, and b) VB = -100 V as a function of the Al content.

At 700 °C, the lowest wear rate is detected for the coatings grown using the target composition Ti/Al 40/60. With the further increase of the Al content, the wear increases due to lower hardness caused by an increasing wurtzite phase fraction.

The application behavior of the coatings was investigated in two different milling tests, where the cutting inserts in SEKW geometry were used for face milling (Fig. 6a) and the inserts in XDKT geometry were used for shoulder milling (Fig. 6b). The milling lifetime increases with rising Al content in the coatings, irrespective of the appearance of a small fraction of the wurtzite phase. For both coating series and both milling tests, the maximum lifetime is reached for the coatings deposited with the Ti/Al 40/60 target. Further increasing of the Al content results in a decrease of the milling lifetime for the coatings V_B = -40 V for both milling tests, while the milling lifetime of coatings deposited with V_B = -100 V remains high. In general, the same trends can be observed in both milling tests, but in shoulder milling considerably longer lifetimes are reached (Fig. 6b).

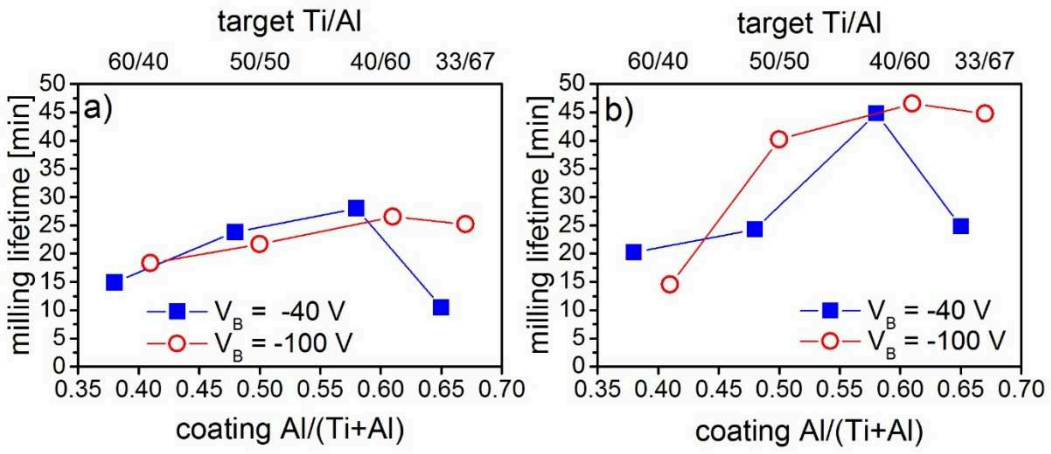

Fig. 6 Milling lifetime of $Ti_{1-x}Al_xN$ coated cemented carbide cutting inserts as a function of the Al content in a) face milling and b) shoulder milling.

3.2. Thermal stability

To illuminate the thermal stability of the coatings, the DSC signal versus temperatures for two representative coatings (Ti/Al 60/40 and 33/67, both deposited at V_B = -100 V) is shown in Fig. 7, enabling the identification of temperatures where microstructural changes occur. DSC signals stemming from $Ti_{1-x}Al_xN$ coatings up to temperatures of ~750 °C originate from recovery and recrystallization processes [9].

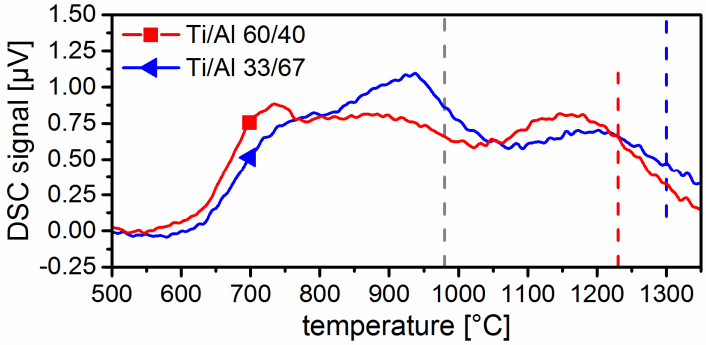

Fig. 7 DSC signal versus temperature obtained for $Ti_{1-x}Al_xN$ coatings deposited with target compositions of Ti/Al = 60/40 and 33/67 at VB = -100 V. The selected temperatures for the annealing treatments are marked by dashed lines.

For temperatures exceeding 750-800 °C, three exothermic contributions occur, corresponding to formation of fcc-AlN and fcc-TiN domains (both in the temperature range 850-950 °C in Fig. 7) and the transformation of fcc-AlN to

wurtzite (above 1050 °C in Fig. 7). These two peaks are shifted to slightly higher temperatures for the higher Al containing coating. For further investigation of the occurring microstructural changes related to these peaks, additional annealing treatments in a vacuum furnace and subsequent XRD measurements were performed. Three different annealing temperatures were chosen for each coating in order to illuminate the main microstructural changes taking place: 980, 1230 and 1500 °C for the coatings deposited with the targets Ti/Al 60/40 and 50/50 and 980, 1300 and 1500 °C for the coatings with higher Al contents.

The X-ray diffractograms of the as deposited and annealed coating powders with the lowest Al content (target composition Ti/Al 60/40), grown at V_B = -40 V and V_B = -100 V, are shown in Fig. 8a and b, respectively. In the as deposited state, both coatings consist of a single-phase fcc-$Ti_{1-x}Al_xN$ structure. After annealing at 980 °C, a peak broadening can be observed. Further, the peaks are slightly shifted to lower diffraction angles and thus towards the standard peak position of fcc-TiN, while a shoulder on their right hand side appears (best visible for the (200) peak), indicating the onset of spinodal decomposition [9,30].

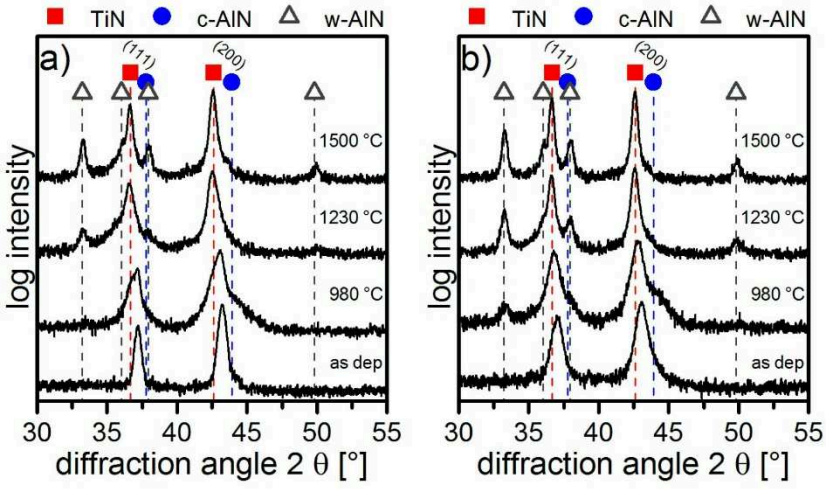

Fig. 8 X-ray diffractograms of annealed $Ti_{1-x}Al_xN$ coatings deposited with a target composition of Ti/Al = 60/40 and a) VB = -40 V, and b) VB = -100 V.

For the coating grown at V_B = -40 (Fig. 8a), the wurtzite peak at a diffraction angle of ~33° is barely noticeable after annealing at 980 °C, whereas for

the coating deposited at V_B = -100 V Fig. 8b) it is already much more pronounced. This might be attributed to the higher amount of nucleation sites due to the finer grained structure [12]. With temperature increasing to 1230 °C, the wurtzite peak at 33° is for both coatings more distinct. At this annealing temperature also wurtzite peaks at higher diffraction angles (36 and 50°) can be observed. The peaks of the cubic phases are shifted to the standard peak position of fcc-TiN. However, the peaks are still asymmetric and broad, which indicates that there is some fcc-AlN left. After further increasing the annealing temperature to 1500 °C, decomposition is completed, as evidenced by sharp and symmetric peaks occurring at their standard positions.

Fig. 9 shows the microstructural evolution of the coatings grown with the Ti/Al 50/50 target. The coatings in the as deposited state clearly show a single-phase fcc-$Ti_{1-x}Al_xN$ structure.

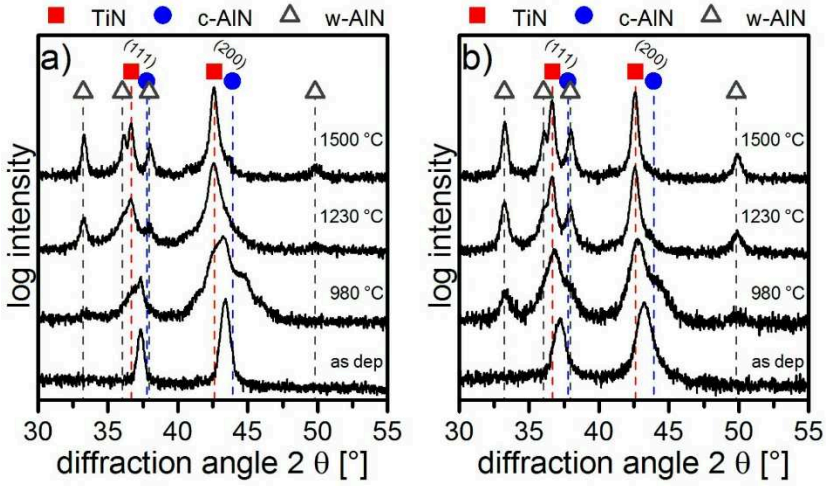

Fig. 9 X-ray diffractograms of annealed $Ti_{1-x}Al_xN$ coatings deposited with a target composition of Ti/Al = 50/50 and a) VB = -40 V, and b) VB = -100 V.

After annealing at 980 °C, already pronounced wurtzite peaks appear for the coating deposited at V_B = -100 V (Fig. 9b), while in the diffractogram of the coating grown at V_B = -40 V only a small wurtzite peak is visible (at 33° in Fig. 9a). At that temperature, a significant broadening of the fcc-$Ti_{1-x}Al_xN$ peaks occurs and shoulders on their right hand side emerge, which are, as already stated, indications for spinodal decomposition. With another temperature increase to 1230 °C, the peaks

of the coating deposited at V_B = -40 V are still broad and asymmetric, while the coating grown at V_B = -100 V shows sharp peaks, indicating an advanced decomposition. At 1500 °C, the decomposition for both coatings is completed.

The microstructural changes after annealing of the coatings deposited with the Al/Ti 40/60 target are summarized in Figs. 10a and b. Already in the as deposited state, the coating grown at V_B = -40 V reveals a small wurtzite peak at 33° (Fig. 10a).

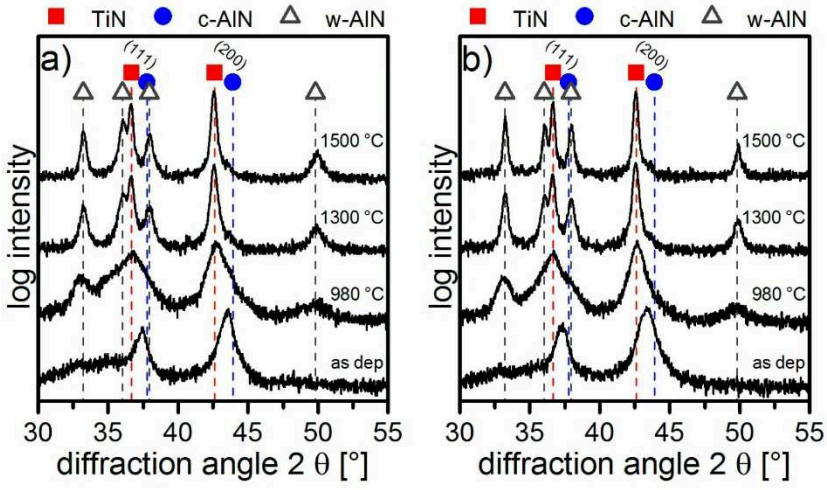

Fig. 10 X-ray diffractograms of annealed $Ti_{1-x}Al_xN$ coatings deposited with a target composition of Ti/Al = 40/60 and a) VB = -40 V, and b) VB = -100 V.

For the coating deposited at V_B = -100 V, a wurtzite peak can be detected as well, but with an even smaller intensity (Fig. 10b). After increasing the temperature to 980 °C, both diffractograms exhibit very broad and asymmetric peaks, but still the fcc phase dominates. Spinodal decomposition is more advanced for the coating deposited at V_B = -100 V, as indicated by the position of the cubic peaks at lower angles. The temperature increase to 1300 °C leads to a complete decomposition of both coatings, indicated by the shift of the peaks towards the standard positions of fcc-TiN and wurtzite AlN. A further increase of the temperature to 1500 °C leads to peaks which are located at the same positions, but appear sharper, which is an indication for grain growth [9].

The changes in microstructure after annealing of the coatings with the highest Al content (target composition Ti/Al 33/67) are presented in Fig. 11a and b. Both coatings show a dual-phase structure in the as deposited state, where the wurtzite phase is more pronounced for the coating deposited with V_B = -40 V (Fig. 11a). After annealing at 980 °C, evidence for decomposition to fcc-TiN and fcc-AlN is clearly visible for the coating grown at V_B = -40 V (compare (200)-peak in Fig. 11a).

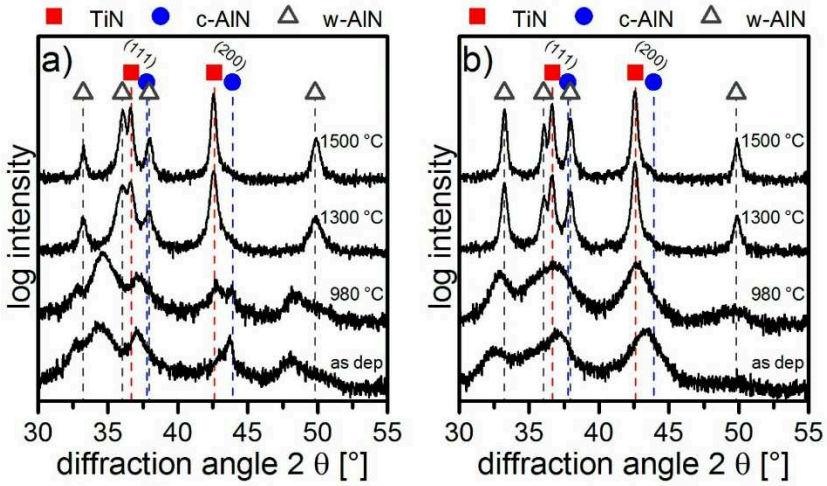

Fig. 11 X-ray diffractograms of annealed $Ti_{1-x}Al_xN$ coatings deposited with a target composition of Ti/Al = 33/67 and a) VB = -40 V, and b) VB = -100 V.

In contrast, the peaks representing cubic phases within the high bias coating do not show an obvious phase separation yet; however, their observed shift to lower diffraction angles and the rise of the intensity of the wurtzite peaks provide strong indications for a more advanced decomposition than for the low bias coating. The temperature increase to 1300 °C results for both coatings in a completed decomposition, where the peaks representing the wurtzite phase are more pronounced for the coating deposited at V_B = -100 V. Annealing of the coatings at 1500 °C results in sharper peaks compared to 1300 °C, indicating grain growth.

4. Discussion

Phase evolution in $Ti_{1-x}Al_xN$ coatings has been addressed in numerous papers [1-28]. Thus, in the following we focus on the discussion of the thermal stability and high temperature properties of arc evaporated $Ti_{1-x}Al_xN$ coatings grown with different Al contents and bias voltages.

In the as deposited state, the coatings deposited at V_B = -100 V show a lower grain size, as indicated by peak broadening, and a single-phase cubic structure stable up to higher Al contents than the coatings grown with V_B = -40 V, which is in good agreement to Wüstefeld *et al.* [2]. The X-ray diffractograms presented in Figs. 8b and 11b confirm that the DSC peak between 850 and 950 °C of both coatings in Fig. 7 stems from spinodal decomposition, which is more pronounced for the coating deposited with the target Ti/Al 33/67, indicating the higher driving force for decomposition due to the higher Al content. The peak above 1050 °C stemming from wurtzite phase formation is more pronounced for the coating deposited with the target Ti/Al 60/40 compared to the target Ti/Al 33/67. This is related to the lower amount of wurtzite AlN already existing within the lower Al containing coating (see Fig. 8b), whereas the coating synthesized with the target Ti/Al 33/67 shows already a pronounced wurtzite phase fraction at 980 °C resulting in a lower driving force for phase transformation.

The coatings grown with V_B = -100 V show more pronounced wurtzite phase fractions than the coatings deposited at V_B = -40 V, which can be explained by the increased driving force for wurtzite phase formation stemming from the higher Al content (Fig. 1) [31]. However, the higher bias voltage also leads to a decomposition finished at lower temperatures, which is evidenced by the increasing dominance of the TiN peak on its standard position (see the (200) peaks in Fig. 8 and Fig. 9). According to Rachbauer *et al.* [32], spinodal decomposition is promoted by smaller grain sizes, providing more diffusion paths via the grain boundaries.

The coherency strains stemming from spinodal decomposition can be expected to result in a hardness increase with increasing Al content [7,33]. This

hardness increase is hardly reflected by the wear rate shown in Fig. 5 for the tests performed at 700 °C. This is most probably related to the early stage of decomposition at this temperature (Fig. 7 and Fig. 11), resulting in a low fraction of cubic domains, and the thin and thus not mechanically protecting oxide scales (according to refs. [34,35], oxide scale thicknesses of a few 10 nm were measured for similar annealing treatments). In contrast, the longest milling lifetime was obtained for the coatings deposited with the target Ti/Al 40/60, despite the hardness decrease due to the appearance of the wurtzite phase. While the milling lifetime for the coating grown with V_B = -40 V and the highest Al content (target composition Ti/Al 33/67) deteriorates, it is just slightly decreasing for the coating deposited at V_B = -100 V. This can be assumed to be due to the dominant wurtzite phase within the coatings grown with V_B = -40 V, while those deposited at V_B = -100 V consist mostly of a cubic phase with minor wurtzite phase fractions. The hardly pronounced agreement between the dependence of the wear rates displayed in Fig. 5 and the milling lifetime presented in Fig. 6 versus the Al content is most likely related to temperature differences between the performed tests. While the 700 °C used for the ball-on-disk tests correspond to the early stage of both, spinodal decomposition [9] and oxide scale formation [6], the temperatures at the cutting edge during the dry milling tests are assumed to be considerably higher [36], giving rise to more pronounced coherency strains and thicker oxide scales.

In summary, taking into account the evolution of microstructure and properties of $Ti_{1-x}Al_xN$ coatings with varying Al contents at elevated temperatures investigated within this work, the following strategies (besides excellent adhesion, low roughness [17], coating thickness and stress state [37] adjusted to the particular application) could be considered to further increase the cutting performance: (*i*) an Al content as high as possible for a sufficient amount of cubic domains and for formation of a stable oxide scale, (*ii*) a wurtzite fraction as small as possible to achieve maximum hardness, and (*iii*) a grain size yielding a suitable length of the diffusion path for spinodal decomposition at the given application temperature to achieve the most pronounced age hardening.

5. Conclusions

Cathodic arc evaporated $Ti_{1-x}Al_xN$ coatings were deposited using targets with four different Ti/Al ratios and two bias voltages, and the relationship between microstructure, mechanical and tribological properties, cutting performance and thermal stability was investigated. In addition to the cubic $Ti_{1-x}Al_xN$ phase, the as deposited coatings are characterized by wurtzite phase fractions for high Al contents, which is more pronounced for the lower bias voltage. The fine grained coatings deposited at higher bias voltage decompose at lower temperatures as a result of the lower diffusion lengths, giving rise to superior performance in milling for high Al contents, despite of a small wurtzite phase fraction. The observed comprehensive insight to the evolution of microstructure and properties of $Ti_{1-x}Al_xN$ coatings enables to suggest design rules individually applied for the given application.

6. Acknowledgements

The authors are grateful to Gerhard Hawranek (Montanuniversität Leoben) for SEM and EDX investigations and to Karsten Köpfle (Ceratizit Austria) for the milling tests. This work was financially supported by the Österreichische Forschungsförderungsgesellschaft FFG (grant number 845255).

References

[1] A. Kimura, H. Hasegawa, K. Yamada, T. Suzuki, Effects of Al content on hardness, lattice parameter and microstructure of $Ti_{1-x}Al_xN$ films, Surf. Coat. Technol. 120-121 (1999) 438–441.

[2] C. Wüstefeld, D. Rafaja, V. Klemm, C. Michotte, M. Kathrein, Effect of the aluminium content and the bias voltage on the microstructure formation in $Ti_{1-x}Al_xN$ protective coatings grown by cathodic arc evaporation, Surf. Coat. Technol. 205 (2010) 1345–1349.

[3] A. Hörling, L. Hultman, M. Odén, J. Sjölén, L. Karlsson, Mechanical properties and machining performance of $Ti_{1-x}Al_xN$-coated cutting tools, Surf. Coat. Technol. 191 (2005) 384–392.

[4] A. Hörling, L. Hultman, M. Odén, J. Sjölén, L. Karlsson, Thermal stability of arc evaporated high aluminum-content $Ti_{1-x}Al_xN$ thin films, J. Vac. Sci. Technol. A 20 (2002) 18

[5] W.-D. Münz, Titanium aluminum nitride films: A new alternative to TiN coatings, J. Vac. Sci. Technol. A 4 (1986) 2717.

[6] D. McIntyre, J.E. Greene, G. Håkansson, J.-E. Sundgren, W.-D. Münz, Oxidation of metastable single-phase polycrystalline $Ti_{0.5}Al_{0.5}N$ films: Kinetics and mechanisms, J. Appl. Phys. 67 (1990) 1542.

[7] S. PalDey, S. Deevi, Single layer and multilayer wear resistant coatings of (Ti,Al)N: a review, Mat. Sci. Eng. A 342 (2003) 58–79.

[8] A. Kimura, H. Hasegawa, K. Yamada, T. Suzuki, Metastable $Ti_{1-x}Al_xN$ films with different Al content, J. Mater. Sci. Lett. 19 (2000) 601–602.

[9] P.H. Mayrhofer, A. Hörling, L. Karlsson, J. Sjölén, T. Larsson, C. Mitterer, L. Hultman, Self-organized nanostructures in the Ti–Al–N system, Appl. Phys. Lett. 83 (2003) 2049.

[10] A. Knutsson, M.P. Johansson, L. Karlsson, M. Odén, Thermally enhanced mechanical properties of arc evaporated $Ti_{0.34}Al_{0.66}N$/TiN multilayer coatings, J. Appl. Phys. 108 (2010) 44312.

[11] C. Wüstefeld, D. Rafaja, M. Dopita, M. Motylenko, C. Baehtz, C. Michotte, M. Kathrein, Decomposition kinetics in $Ti_{1-x}Al_xN$ coatings as studied by

in-situ X-ray diffraction during annealing, Surf. Coat. Technol. 206 (2011) 1727–1734.

[12] N. Schalk, C. Mitterer, J. Keckes, M. Penoy, C. Michotte, Influence of residual stresses and grain size on the spinodal decomposition of metastable $Ti_{1-x}Al_xN$ coatings, Surf. Coat. Technol. 209 (2012) 190–196.

[13] M. Pfeiler, C. Scheu, H. Hutter, J. Schnöller, C. Michotte, C. Mitterer, M. Kathrein, On the effect of Ta on improved oxidation resistance of Ti–Al–Ta–N coatings, J. Vac. Sci. Technol. A 27 (2009) 554.

[14]] A.E. Reiter, V.H. Derflinger, B. Hanselmann, T. Bachmann, B. Sartory, Investigation of the properties of $Al_{1-x}Cr_xN$ coatings prepared by cathodic arc evaporation, Surf. Coat. Technol. 200 (2005) 2114–2122.

[15] J.L. Endrino, V. Derflinger, The influence of alloying elements on the phase stability and mechanical properties of AlCrN coatings, Surf. Coat. Technol. 200 (2005) 988–992.

[16] J.L. Endrino, G.S. Fox-Rabinovich, R. Escobar Galindo, W. Kalss, S. Veldhuis, L. Soriano, J. Andersson, A. Gutiérrez, Oxidation post-treatment of hard AlTiN coating for machining of hardened steels, Surf. Coat. Technol. 204 (2009) 256–262.

[17] M. Tkadletz, C. Mitterer, B. Sartory, I. Letofsky-Papst, C. Czettl, C. Michotte, The effect of droplets in arc evaporated TiAlTaN hard coatings on the wear behavior, Surf. Coat. Technol. 257 (2014) 95–101.

[18] R. Saha, W.D. Nix, Effects of the substrate on the determination of thin film mechanical properties by nanoindentation, Acta Mater. 50 (2002) 23–38.

[19] A.C. Fischer-Cripps, Critical review of analysis and interpretation of nanoindentation test data, Surf. Coat. Technol. 200 (2006) 4153–4165.

[20] A. Anders, A structure zone diagram including plasma-based deposition and ion etching, Thin Solid Films 518 (2010) 4087–4090.

[21] D. Rafaja, C. Wüstefeld, C. Baehtz, V. Klemm, M. Dopita, M. Motylenko, C. Michotte, M. Kathrein, Effect of Internal Interfaces on Hardness and Thermal Stability of Nanocrystalline $Ti_{0.5}Al_{0.5}N$ Coatings, Metall and Mat Trans A 42 (2011) 559–569.

[22] K. Sato, N. Ichimiya, A. Kondo, Y. Tanaka, Microstructure and mechanical properties of cathodic arc ion-plated (Al,Ti)N coatings, Surf. Coat. Technol. 163-164 (2003) 135–143.

[23] M. Ahlgren, H. Blomqvist, Influence of bias variation on residual stress and texture in TiAlN PVD coatings, Surf. Coat. Technol. 200 (2005) 157–160.

[24] P. Mayrhofer, F. Kunc, J. Musil, C. Mitterer, A comparative study on reactive and non-reactive unbalanced magnetron sputter deposition of TiN coatings, Thin Solid Films 415 (2002) 151–159.

[25] H.A. Jehn, in: W. Gissler, H. Jehn (Eds.), Advanced Techniques for Surface Engineering, Springer Netherlands, 1992, pp. 5-29.

[26] K. Kutschej, P.H. Mayrhofer, M. Kathrein, P. Polcik, R. Tessadri, C. Mitterer, Structure, mechanical and tribological properties of sputtered $Ti_{1-x}Al_xN$ coatings with $0.5 \leq x \leq 0.75$, Surf. Coat. Technol. 200 (2005) 2358–2365.

[27] I.M. Hutchings, Tribology: Friction and Wear of Engineering Materials, 1. publ ed., Metallurgy & materials science series, Arnold, London u.a, 1992.

[28] Siva Rama Krishna, D., Y.L. Brama, Y. Sun, Thick rutile layer on titanium for tribological applications, Tribol. Int. 40 (2007) 329–334.

[29] T. Weirather, K. Chladil, B. Sartory, D. Caliskanoglu, R. Cremer, W. Kölker, C. Mitterer, Increased thermal stability of $Ti_{1-x}Al_xN$/TiN multilayer coatings through high temperature sputter deposition on powder-metallurgical high-speed steels, Surf. Coat. Technol. 257 (2014) 48–57.

[30] R. Rachbauer, D. Holec, P.H. Mayrhofer, Increased thermal stability of Ti–Al–N thin films by Ta alloying, Surf. Coat. Technol. 211 (2012) 98–103.

[31] P.H. Mayrhofer, F.D. Fischer, H.J. Böhm, C. Mitterer, J.M. Schneider, Energetic balance and kinetics for the decomposition of supersaturated $Ti_{1-x}Al_xN$, Acta Mater. 55 (2007) 1441–1446.

[32] R. Rachbauer, S. Massl, E. Stergar, D. Holec, D. Kiener, J. Keckes, J. Patscheider, M. Stiefel, H. Leitner, P.H. Mayrhofer, Decomposition

pathways in age hardening of Ti-Al-N films, J. Appl. Phys. 110 (2011) 23515.

[33] L. Chen, J. Paulitsch, Y. Du, P.H. Mayrhofer, Thermal stability and oxidation resistance of Ti–Al–N coatings, Surf. Coat. Technol. 206 (2012) 2954–2960.

[34] V. Khetan, N. Valle, D. Duday, C. Michotte, C. Mitterer, M.-P. Delplancke-Ogletree, P. Choquet, Temperature-Dependent Wear Mechanisms for Magnetron-Sputtered AlTiTaN Hard Coatings, ACS Appl. Mater. Interfaces (2014) 140822141431002.

[35] M. Pfeiler, J. Zechner, M. Penoy, C. Michotte, C. Mitterer, M. Kathrein, Improved oxidation resistance of TiAlN coatings by doping with Si or B, Surf. Coat. Technol. 203 (2009) 3104–3110.

[36] J. Kopac, M. Sokovic, S. Dolinsek, Tribology of coated tools in conventional and HSC machining, J. Mater. Process. Tech. 118 (2001) 377–384.

[37] A. Riedl, R. Daniel, J. Todt, M. Stefenelli, D. Holec, B. Sartory, C. Krywka, M. Müller, C. Mitterer, J. Keckes, A combinatorial X-ray sub-micron diffraction study of microstructure, residual stress and phase stability in TiAlN coatings, Surf. Coat. Technol. 257 (2014) 108–113.

Publication II

Tailoring age hardening of $Ti_{1-x}Al_xN$ by Ta alloying

Journal of Vacuum Science & Technology A:
Vacuum, Surfaces and Films 35, 060604 (2017)

by

Birgit Grossmann, Andreas Jamnig, Nina Schalk,
Christoph Czettl, Markus Pohler, Christian Mitterer

1. Introduction

Despite the extensive research on $Ti_{1-x}Al_xN$ based hard coatings during the last two decades, there is still room for further improvement of their microstructure and properties. The benefits of this material system rely on its outstanding hardness and oxidation resistance at elevated temperature based on spinodal decomposition of the metastable supersaturated face-centered cubic (fcc-) $Ti_{1-x}Al_xN$ solid solution and thus age hardening [1–4] as well as on the formation of dense and thus protecting oxide scales [5]. However, at temperatures exceeding the onset of spinodal decomposition, the metastable fcc-AlN transforms to the stable wurtzite (w-) AlN, resulting in a hardness drop [1,3]. Further, the mechanical properties of $Ti_{1-x}Al_xN$ are considerably influenced by its chemical composition, since the incorporation of Al into fcc-TiN is limited up to x~0.6-0.7. Exceeding this solubility limit results in the formation of a dual-phase structure, i.e. the fcc-$Ti_{1-x}Al_xN$ solid solution and the unfavored w-AlN phase, which is known to deteriorate the mechanical properties [1,2,6,7]. Earlier papers indicate that alloying of Ta to $Ti_{1-x}Al_xN$ shifts the wurtzite phase formation to higher Al contents [8] as well as to higher temperatures [9]. However, there is a lack of studies on the influence of Ta contents varied systematically up to high values within the $Ti_{1-x-y}Al_xTa_yN$ system on the mechanical properties and thermal stability. Thus, within the present work the influence of an increasing Ta content up to y=0.231 in $Ti_{1-x-y}Al_xTa_yN$ coatings on their mechanical properties as well as on their thermal stability was investigated.

2. Experimental

The coatings were deposited using cathodic arc evaporation in an industrial scale Oerlikon Balzers Innova deposition plant. The Ta content of the powder metallurgically manufactured TiAlTa compound targets was 0, 1, 2.5, 5, 10, and 15 at.-%, respectively, at a constant Ti:Al ratio of 1:1. As substrates, polished cemented carbide (CC) cutting inserts in SNUN 120312EN geometry (according to ISO 1832) were used, as well as a low alloy steel foil. The steel foil was mounted onto the substrate carrousel to undergo 2-fold rotation, while the CC inserts were coated

using 3-fold rotation. The depositions were performed in pure N_2 atmosphere (3.2×10^{-2} mbar) at a bias voltage of -70 V and a substrate temperature of 550 °C. Prior to deposition, the substrates were ion-etched in a pure argon plasma.

The respective coating thickness was determined by the ball cratering technique utilizing a CSM Instruments CaloWear device to 3.7±0.2 µm. The elemental composition of the coatings was measured by energy dispersive X-ray spectroscopy using an Oxford Instruments INCA extension in a Zeiss EVO50 scanning electron microscope and is shown in table 1 together with the composition of the respective targets. The microstructure was investigated utilizing a Bruker-AXS D8 Advance X-ray diffractometer equipped with a Sol-X detector and a Cu-Kα X-ray source with a wavelength of 0.154 nm. Coatings in the as deposited state on CC were measured in gracing incidence configuration (angle of incidence: 2 °). A CSM instruments nanoindenter, equipped with a Berkovich tip, was used to determine the indentation hardness. 20 indents per sample were made to obtain reliable values. The loading rate was 60 mN/min, with a maximum load of 30 mN. Prior to the measurements, the catings were polished with 3 and 1 µm diamond suspension, to obtain smooth surfaces.

Differential scanning calorimetry (DSC) was applied to determine the microstructural changes during annealing, utilizing a Setaram Setsys Evo 2400 system. The coating powder used for DSC was produced by chemically dissolving the coated steel foil in 2M nitric acid. Subsequently, the powder was dried and ground. During the DSC measurements, the chamber was purged with argon, and a heating rate of 23 K/min was applied up to 1500 °C. By analyzing the DSC signal, temperatures for additional annealing treatments were determined, aiming at a thorough investigation of the partial reactions taking place during thermal ramping. The annealing treatments were carried out in a high vacuum furnace (HTM Reetz, base pressure $<5\times10^{-6}$ mbar) with a heating rate of 20 K/min, a holding time of 15 min and a system depending cooling rate. Prior to and after annealing, the microstructure of the powder was investigated using the same Bruker-AXS diffractometer as already mentioned, but in Θ-2Θ mode. The lattice parameter a of

the measured powders was calculated with a combination of Bragg's law and the plane-spacing equation for cubic crystals

$$a = \frac{\lambda}{2\sin(\theta)}\sqrt{h^2 + k^2 + l^2}$$

where λ is the wavelength, θ is the diffraction angle and (hkl) are the Miller indices of the respective diffraction peak [10]. In addition, utilizing the same high vacuum furnace and annealing parameters, a series of heat treatments was done for coated CC between 700 and 1000 °C with steps of 50 °C. Hardness evolution was subsequently measured using these samples and the already mentioned nanoindenter.

3. Results and discussion

In table 1 the elemental composition of the coatings and targets is summarized. All coatings contain 48.3±3.3 at.-% nitrogen. The Ta content in the coatings is considerably higher than in the respective targets, whereas a significant fraction of Al atoms is lost during deposition. The huge mass difference between Al, Ti and Ta and the therefore high possibility of Al for being scattered in the gas phase is a reasonable explanation for this phenomenon [11]. In addition preferred resputtering of Al has been reported as another reason to explain the differences between coating and target composition [11]. In the following, the chemical composition of the coatings in the form $Ti_{1-x-y}Al_xTa_yN$ will be used to distinguish the different samples.

Table 1: Elemental composition of the targets and the respective $Ti_{1-x-y}Al_xTa_yN$ coatings (in at.-%).

Ti/Al/Ta (target)	50/50/0	49.5/49.5/1	48.7/48.8/2.5	47.5/47.5/5	45/45/10	42.5/42.5/15
Ti/Al/Ta (coating	53.4/46.6/0	52.3/46.5/1.2	52.1/43.9/4	49.7/42.5/7.8	46.7/36.8/16.5	43/33.9/23.1

Fig. 1a shows the X-ray diffractograms of the as deposited coatings, from bottom to top with increasing Ta content. The standard peak positions for fcc-TiN (ICDD 00-038-1420), fcc-AlN (ICDD 00-025-1495) as well as fcc-TaN (ICDD 00-049-1283) are added as dashed lines. Additionally, the peaks of the WC phase of the substrate are visible and marked by asterisks (ICDD 03-065-4539). All coatings show

a single-phase fcc structure. The diffractogram of the coating without Ta shows that the fcc-$Ti_{1-x}Al_xN$ peak is located between the standard peak positions of fcc-AlN and TiN. While the X-ray diffractogram of $Ti_{0.523}Al_{0.465}Ta_{0.012}N$ hardly shows any differences to the diffractogram of the Ta-free system, the higher Ta content of $Ti_{0.521}Al_{0.439}Ta_{0.04}N$ results in a small shift of the $Ti_{1-x-y}Al_xTa_yN$ peak to lower angles, indicating an increase of the lattice parameter, as already reported by Rachbauer *et al* [12]. A further increase of the Ta content to $Ti_{0.497}Al_{0.425}Ta_{0.078}N$, $Ti_{0.467}Al_{0.368}Ta_{0.165}N$ and $Ti_{0.43}Al_{0.339}Ta_{0.231}N$ leads to a further shift of the peaks of the fcc phase to lower angles. With increasing Ta content, also a broadening of the peaks can be observed. This can be attributed to grain refinement, but might also indicate the formation of fcc-TiTaN- and fcc-AlN enriched domains as a result of surface initiated spinodal decomposition already during coating growth [12,13].

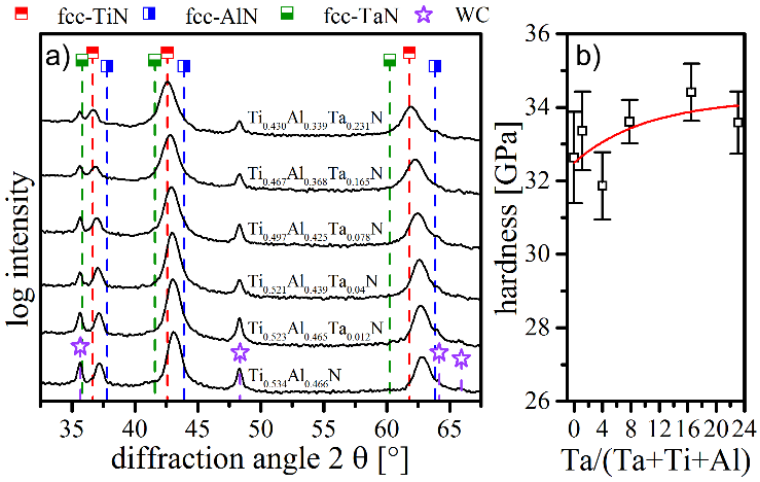

Fig. 1 a) X-ray diffractograms of the $Ti_{1-x-y}Al_xTa_yN$ coatings. The peaks of the WC phase originate from the CC substrate. b) Hardness of the as deposited $Ti_{1-x-y}Al_xTa_yN$ coatings as a function of Ta content.

With increasing Ta content, a slight increase of the hardness occurs, as shown in Fig. 1b, starting from 32.5 GPa for $Ti_{0.534}Al_{0.466}N$ up to 34.4 GPa for $Ti_{0.467}Al_{0.368}Ta_{0.165}N$. This is in good agreement with the observed grain refinement, the indication for the onset of spinodal decomposition during deposition and the

hardness increase observed by Rachbauer *et al.* for $Ti_{1-x-y}Al_xTa_yN$ coatings grown by magnetron sputter deposition [8].

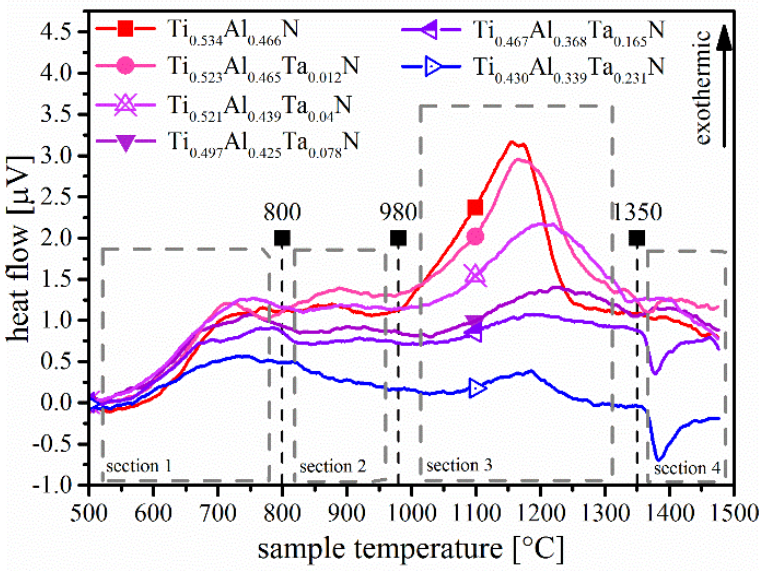

Fig. 2 DSC signal of the $Ti_{1-x-y}Al_xTa_yN$ coatings with different Ta contents as a function of temperature. The three selected temperatures for additional annealing treatments are marked by dashed lines.

Powdered coatings were investigated by DSC to determine microstructural changes during annealing. The respective DSC signals as a function of temperature are presented in Fig. 2. For all six Ta contents, the DSC features can be divided into four sections. The first one below 800 °C (section 1), the second between 800 and 980 °C (section 2), the third between 980 and 1350 °C where the largest exothermic DSC signal was detected, and section 4, where the coatings with a low Ta content show an additional small exothermic peak, while for $Ti_{0.467}Al_{0.368}Ta_{0.165}N$ and $Ti_{0.43}Al_{0.339}Ta_{0.231}N$, an endothermic feature at about 1380 °C is visible. With increasing Ta content, the position of the peaks in section 2 and 3 are shifted to higher temperatures, and their intensity decreases, indicating a less pronounced reaction. To further investigate the partial reactions leading to the respective features, annealing treatments of the powdered coatings in a vacuum furnace at 800, 980 and 1350 °C were conducted and subsequent X-ray diffraction measurements were carried out. The results are hereinafter presented together with the diffractograms received after the DSC run.

The resulting diffractograms of the coating powders after the annealing treatments are presented in Figs. 3a-f. In the as deposited state, they are similar for coatings on the CC substrate and in powder form, both indicating formation of a fcc phase for all compositions. After annealing the $Ti_{0.534}Al_{0.466}N$ powder at 800 °C (Fig. 3a), a slight peak shift towards higher diffraction angles is detectable which corresponds to section 1 in Fig. 2 and indicates recovery processes with relaxation of microstrains [14]. Additionally, on both sides of the (200) peak shoulders are visible, evidencing first signs of spinodal decomposition (i.e. formation of fcc-TiN rich domains evidenced by a shoulder on the left hand side and a less pronounced shoulder on the right hand side of the peak indicating fcc-AlN rich domains) [3,8]. An increase of the annealing temperature to 980 °C leads to a shift of the fcc-$Ti_{1-x}Al_xN$ peaks to lower angles towards the standard peak position of fcc-TiN, while on the right hand side of the (200) peak the shoulder increases, indicating advanced spinodal decomposition. Additionally to the $Ti_{1-x}Al_xN$ phase, first w-AlN peaks can be detected. The DSC features in section 2 can thus be related to spinodal decomposition and beginning wurtzite phase formation. Further increase of the annealing temperature to 1350 °C results in pronounced w-AlN peaks (Fig. 3a), while the fcc-$Ti_{1-x}Al_xN$ peak reaches the fcc-TiN peak position, indicating that fcc-$Ti_{1-x}Al_xN$ has completely decomposed and fcc-AlN has transformed to w-AlN. The pronounced feature in section 3 of the DSC plot can thus be associated with formation of the wurtzite phase. The further increase of the annealing temperature to 1500 °C (i.e. after the DSC run) has no influence on the X-ray diffractogram of the $Ti_{0.534}Al_{0.466}N$ powder and consequently no feature was detected in section 4 of the DSC signal. The X-ray diffractograms of the $Ti_{0.523}Al_{0.465}Ta_{0.012}N$ and $Ti_{0.521}Al_{0.439}Ta_{0.04}N$ powders (Figs. 3b and c) show in the as deposited state a shift of the fcc-$Ti_{1-x-y}Al_xTa_yN$ peak towards lower angles, as already discussed in Fig. 1a. After annealing at 800 °C, for both samples slight shoulders are visible in the diffractograms, which concurs with the DSC features of the respective powders being shifted to slightly higher temperatures (section 1 in Fig. 2). After the annealing treatment at 980 °C, the height of the shoulders on the right hand side of the fcc-$Ti_{1-x-y}Al_xTa_yN$ peak decreases

with increasing Ta content, the fcc-$Ti_{1-x-y}Al_xTa_yN$ peaks shift to lower angles and the wurtzite peak at ~33 ° is less pronounced than for the Ta-free coating. This is again in good agreement with the decreasing intensity of the DSC features for these compositions and their shift to higher temperatures (section 2 in Fig. 2). After annealing at 1350 °C, the fcc-$Ti_{1-x-y}Al_xTa_yN$ peaks are shifted to even lower diffraction angles than the standard peak position of TiN. The intensity of the wurtzite peak of the $Ti_{0.521}Al_{0.439}Ta_{0.04}N$ powder compared to the Ta-free powder after annealing at 1350 °C is less pronounced (Figs. 3a and c), and concurs with the DSC signal for both coatings, which shows a shift of the onset temperature of wurtzite phase formation to higher values (section 3 in Fig. 2). Spinodal decomposition as well as wurtzite phase formation are finished for the $Ti_{0.523}Al_{0.465}Ta_{0.012}N$ and $Ti_{0.521}Al_{0.439}Ta_{0.04}N$ powders at 1350 °C, as the X-ray diffractograms show no differences to those of the coatings annealed at 1500 °C. For the $Ti_{0.497}Al_{0.425}Ta_{0.078}N$ powder, the increased Ta content leads in the as deposited state to a further shift to lower angles (Fig. 3d). After annealing at 800 °C, two slight shoulders at both sides of the fcc (200) peak appear. Annealing at 980 °C leads to more pronounced shoulders and a shift of the fcc-$Ti_{1-x-y}Al_xTa_yN$ peak to lower angles, which indicates spinodal decomposition. After annealing at 1350 °C, a peak indicating w-AlN can be observed, as well as a pronounced peak shift towards lower angles, leaving the fcc-peak situated between fcc-TiN and fcc-TaN. Additionally, the hexagonal (hex-) Ta_2N phase (ICDD 01-089-4764) can be detected, which represents a stable nitride within the Ta-N system [15–17]. Increasing the annealing temperature to 1500 °C results in narrow peaks without shoulders, indicating a complete decomposition and phase transformation of fcc-AlN to w-AlN.

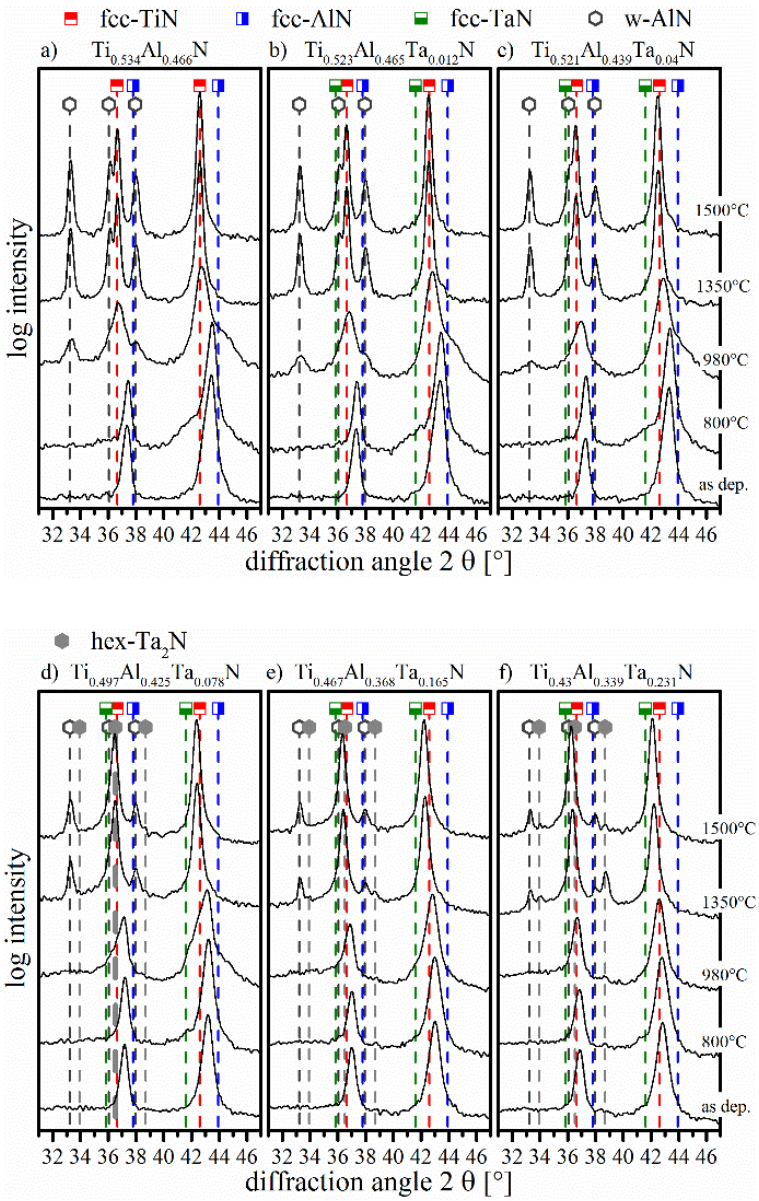

Fig. 3 Phase evolution with increasing annealing temperatures for the powdered coatings of a) $Ti_{0.534}Al_{0.466}N$, b) $Ti_{0.523}Al_{0.465}Ta_{0.012}N$, c) $Ti_{0.521}Al_{0.439}Ta_{0.04}N$, d) $Ti_{0.497}Al_{0.425}Ta_{0.078}N$, e) $Ti_{0.467}Al_{0.368}Ta_{0.165}N$ and f) $Ti_{0.43}Al_{0.339}Ta_{0.231}N$ (as dep. indicates the as deposited state).

A further increase of the Ta content ($Ti_{0.467}Al_{0.368}Ta_{0.165}N$ and $Ti_{0.43}Al_{0.339}Ta_{0.231}N$ in Figs. 3e and f) leads to a further retardation of decomposition and wurtzite phase formation to higher temperatures, which is in good agreement with the detected DSC signal for these samples (sections 2 and 3 in Fig. 2). The

$Ti_{0.467}Al_{0.368}Ta_{0.165}N$ powder shows small shoulders on both sides of the fcc-$Ti_{1-x-y}Al_xTa_yN$ peak after annealing at 980 °C, indicating the onset of spinodal decomposition. After annealing at 1350 °C, the peak shift and the additionally visible w-AlN peaks point towards a more advanced decomposition. Besides the peak shift to lower angles after annealing at 980 °C, no evidence of decomposition is visible up to an annealing temperature of 1350 °C for the $Ti_{0.43}Al_{0.339}Ta_{0.231}N$ powder. At this temperature, w-AlN is evident and thus the loss of AlN in the fcc-$Ti_{1-x-y}Al_xTa_yN$ matrix results in a further peak shift towards lower diffraction angles. At1500 °C, fcc-AlN has completely transformed to w-AlN, and the fcc-$Ti_{1-x-y}Al_xTa_yN$ peak is located between the standard peak positions of TaN and TiN. For $Ti_{0.467}Al_{0.368}Ta_{0.165}N$ and $Ti_{0.43}Al_{0.339}Ta_{0.231}N$ the metastable fcc-$Ti_{1-x-y}Al_xTa_yN$ solid solution seems mostly to be supersaturated by Ta at the synthesis condition used, since hex-Ta_2N precipitates seem already to be present in the as deposited state (i.e. the increased noise at 38.8 °). Since the formation of hex-Ta_2N is accompanied by a N_2-release, the reaction in the DSC plot in Fig. 2 appears as an endothermic feature [18]. The superimposition of this endothermic feature with the exothermic peak stemming from the w-AlN phase formation should not be misleadingly identified as a shift of the wurtzite formation to lower temperatures (section 3 in Fig. 2). A second endothermic feature for the $Ti_{0.467}Al_{0.368}Ta_{0.165}N$ and $Ti_{0.43}Al_{0.339}Ta_{0.231}N$ powders can be observed at ~1375 °C (section 4 in Fig. 2), which is in good agreement with the decrease of the hex-Ta_2N peak after annealing at 1500 °C, indicating further N_2 release. The out-of-plane lattice parameters of the powdered samples determined from the (200) peak position are summarized in Fig. 4, evidencing the increasing lattice parameter with increasing Ta content of the as deposited coatings. After annealing at 800 °C, the lattice parameters are slightly decreased due to recovery. The retarded spinodal decomposition is evidenced by the less steep increase of the lattice parameter for those coatings with $y \geq 0.078$.

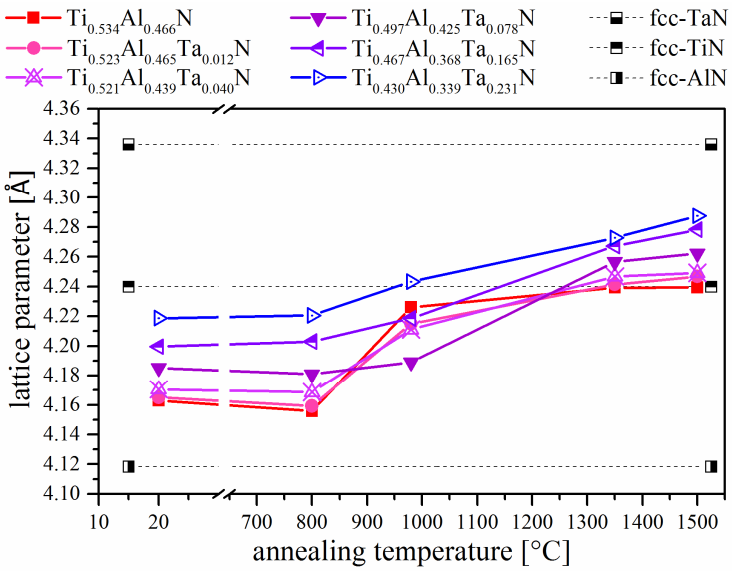

Fig. 4 Evolution of the lattice parameter: of the $Ti_{1-x-y}Al_xTa_yN$ coatings with different Ta contents as a function of temperature. The standard lattice parameters of fcc-TaN, fcc-TiN and fcc-AlN are shown as well.

In Figs. 5 the hardness of the $Ti_{1-x-y}Al_xTa_yN$ coatings as a function of the annealing temperature are presented. The $Ti_{1-x}Al_xN$ coating shows a hardness increase from 32.5 in the as deposited state to 34 GPa at 700 °C caused by spinodal decomposition (Fig. 5a) [3,8]. For T>700 °C the hardness is slightly reduced; at T>850 °C it drops drastically due to the onset of w-AlN formation. The $Ti_{0.523}Al_{0.465}Ta_{0.012}N$ coating shows the highest hardness value of 34 GPa at 750 °C; a further temperature increase up to 850 °C leads to a slight hardness reduction followed by a significant drop at even higher temperatures. An increase of the Ta content to $Ti_{0.521}Al_{0.439}Ta_{0.04}N$, results in a slight hardness increase with temperature rising up to 800 °C, and a constant decrease for higher temperatures, until the minimum hardness of ~30 GPa is reached at 1000 °C. For the $Ti_{0.497}Al_{0.425}Ta_{0.078}N$ coating (Fig. 5b) no specific hardness maximum can be detected, i.e. from the as deposited state up to 900 °C the hardness values are rather constant between 33 and 34.2 GPa; they slightly decrease for T>950 °C to a minimum value of 32.7 GPa. With a further increase of the Ta content to $Ti_{0.467}Al_{0.368}Ta_{0.165}N$, the high hardness is maintained up to higher temperatures, yielding a hardness of 34 GPa even after

annealing at 950 °C. The coating containing the highest Ta content, i.e. $Ti_{0.43}Al_{0.339}Ta_{0.231}N$, does also not show a distinct hardness maximum but reaches with a value of 32.2 GPa the highest hardness at 1000 °C of all coatings.

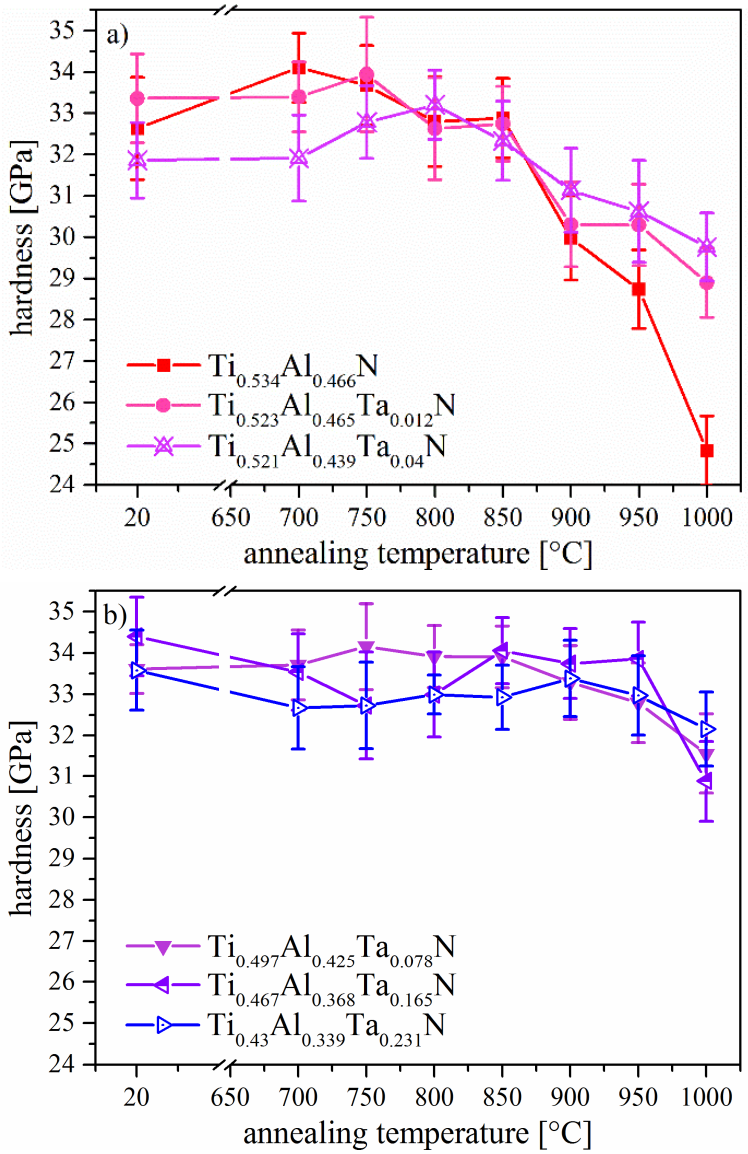

Fig. 5 Hardness of the $Ti_{1-x-y}AlxTayN$ coatings with a) a low Ta content and b) a high Ta content after annealing in vacuum.

Our findings demonstrate that diffusion-governed processes like spinodal decomposition and wurtzite phase formation of TiAlN based coatings can be tailored by incorporation of Ta. The retardation of these processes by even low amounts of

Ta is explained by two mechanisms, i.e. the additional residual stress stemming from incorporation of large Ta atoms within the $Ti_{1-x}Al_xN$ solid solution hinders diffusion and the lower driving force for decomposition as a result of the reduced mixing enthalpy stabilizes the metastable $Ti_{1-x-y}Al_xTa_yN$ solid solution [19]. The latter arises from the reduced Al content and the therefore decreased stored energy, evidenced by the intensity decrease of the DSC signal [11]. The X-ray diffractograms after annealing also confirm the shift of the onset of spinodal decomposition as well as wurtzite phase formation with increasing Ta content to higher temperatures.

Various researchers observed the sub-stoichiometric hex-Ta_2N phase in their as deposited TaN coatings by varying the N_2 partial pressure [15,17,20,21]. Hex-Ta_2N was also detected after annealing of TaN coatings in an atmosphere without N_2 supersaturation [22–24] as well as of $Al_{1-x}Ta_xN$ coatings [18] and of high Ta containing $Ti_{1-x-y}Al_xTa_yN$ coatings [9,11]. While in most reports, the hex-Ta_2N phase is formed in ternary or quaternary systems after annealing treatments above 1000 °C [9,11,18], it exists in the present $Ti_{0.467}Al_{0.368}Ta_{0.165}N$ and $Ti_{0.43}Al_{0.339}Ta_{0.231}N$ coatings already in the as deposited state. This might be attributed to differences in the synthesis conditions, where the higher bias voltage of -70 V applied in the present study leads to a considerably finer grained structure [14] compared to other reports (e.g. a bias voltage of -40 V was used in [9,18]), which promotes diffusion-driven phase formation [25] and thus results in the early formation of the hex-Ta_2N phase.

The coatings containing a low Ta content (i.e., $Ti_{0.534}Al_{0.466}N$, $Ti_{0.523}Al_{0.465}Ta_{0.012}N$ and $Ti_{0.521}Al_{0.439}Ta_{0.04}N$) show age hardening effects originating from coherency strains due to spinodal decomposition; their hardness maximum is – similar to their onset temperature of spinodal decomposition – shifted to higher temperatures with increasing Ta content. However, for those coatings exceeding a certain Ta content (i.e. $Ti_{0.497}Al_{0.425}Ta_{0.078}N$, $Ti_{0.467}Al_{0.368}Ta_{0.165}N$ and $Ti_{0.43}Al_{0.339}Ta_{0.231}N$) no obvious evidence for a hardness increase is present. The softening due to recovery and grain growth [26] is obviously balanced by age hardening, yielding stable hardness values up to 950-1000 °C. This is in contradiction to the hardness reported by Koller *et al* [9], who observed for $Ti_{0.45}Al_{0.36}Ta_{0.19}N$

coatings a hardness increase of ~5 GPa after annealing at 1000 °C and thus pronounced age hardening. Microstructural analysis showed no hex-Ta_2N phase in their coatings. The influence of hex-Ta_2N on the mechanical properties of $Ti_{1-x-y}Al_xTa_yN$ has not been investigated yet; however, it potentially hampers the favored age hardening.

4. Conclusion

The present work highlights the influence of varying Ta contents on the mechanical properties and thermal stability of $Ti_{1-x-y}Al_xTa_yN$ coatings. An increasing Ta content enhances the thermal stability of the fcc-$Ti_{1-x-y}Al_xTa_yN$ solid solution by shifting the spinodal decomposition to higher temperatures, thus maintaining a high coating hardness up to 1000 °C.

5. Acknowledgements

The authors acknowledge Manuela Male (Ceratizit Austria GmbH) for the nanoindentation measurements. This work was financially supported by the Österreichische Forschungsförderungsgesellschaft FFG (grant number 845255).

References

[1] A. Hörling, L. Hultman, M. Odén, J. Sjölén, L. Karlsson, Mechanical properties and machining performance of $Ti_{1-x}Al_xN$-coated cutting tools, Surface and Coatings Technology 191 (2005) 384–392.

[2] A. Hörling, L. Hultman, M. Odén, J. Sjölén, L. Karlsson, Thermal stability of arc evaporated high aluminum-content $Ti_{1-x}Al_xN$ thin films, Journal of Vacuum Science & Technology A: Vacuum, Surfaces, and Films 20 (2002) 1815–1823.

[3] P.H. Mayrhofer, A. Hörling, J. Sjölén, T. Larsson, C. Mitterer, L. Hultman, Self-organized nanostructures in the Ti-Al-N system, Appl. Phys. Lett. 83 (2003) 2049–2051.

[4] A. Knutsson, M.P. Johansson, L. Karlsson, M. Odén, Thermally enhanced mechanical properties of arc evaporated $Ti_{0.34}Al_{0.66}N$/TiN multilayer coatings, Journal of Applied Physics 108 (2010) 44312.

[5] D. McIntyre, J.E. Greene, G. Håkansson, J.-E. Sundgren, W.-D. Münz, Oxidation of metastable single-phase polycrystalline $Ti_{0.5}Al_{0.5}N$ films: Kinetics and mechanisms, J. Appl. Phys. 67 (1990) 1542.

[6] A. Kimura, H. Hasegawa, K. Yamada, T. Suzuki, Effects of Al content on hardness, lattice parameter and microstructure of $Ti_{1-x}Al_xN$ films, Surf. Coat. Technol. 120-121 (1999) 438–441.

[7] C. Wüstefeld, D. Rafaja, V. Klemm, C. Michotte, M. Kathrein, Effect of the aluminium content and the bias voltage on the microstructure formation in $Ti_{1-x}Al_xN$ protective coatings grown by cathodic arc evaporation, Surf. Coat. Technol. 205 (2010) 1345–1349.

[8] R. Rachbauer, D. Holec, P.H. Mayrhofer, Increased thermal stability of Ti–Al–N thin films by Ta alloying, Surf. Coat. Technol. 211 (2012) 98–103.

[9] C.M. Koller, R. Hollerweger, C. Sabitzer, R. Rachbauer, S. Kolozsvári, J. Paulitsch, P.H. Mayrhofer, Thermal stability and oxidation resistance of arc evaporated TiAlN, TaAlN, TiAlTaN, and TiAlN/TaAlN coatings, Surf. Coat. Technol. 259 (2014) 599–607.

[10] B.D. Cullity, Elements of X-Ray Diffraction, Addison-Wesley (1956) Menlo Park.

[11] R. Hollerweger, H. Riedl, J. Paulitsch, M. Arndt, R. Rachbauer, P. Polcik, S. Primig, P.H. Mayrhofer, Origin of high temperature oxidation resistance of Ti–Al–Ta–N coatings, Surf. Coat. Technol. 257 (2014) 78–86.

[12] R. Rachbauer, D. Holec, P.H. Mayrhofer, Phase stability and decomposition products of Ti–Al–Ta–N thin films, Appl. Phys. Lett. 97 (2010) 151901.

[13] F. Adibi, I. Petrov, L. Hultman, U. Wahlström, T. Shimizu, D. McIntyre, J.E. Greene, J.-E. Sundgren, Defect structure and phase transitions in epitaxial metastable cubic $Ti_{0.5}Al_{0.5}N$ alloys grown on MgO(001) by ultra-high-vacuum magnetron sputter deposition, J. Appl. Phys. 69 (1991) 6437.

[14] N. Schalk, C. Mitterer, J. Keckes, M. Penoy, C. Michotte, Influence of residual stresses and grain size on the spinodal decomposition of metastable $Ti_{1-x}Al_xN$ coatings, Surf. Coat. Technol. 209 (2012) 190–196.

[15] J. Gatterer, G. Dufek, P. Ettmayer, R. Kieffer, Das kubische Tantalmononitrid (B 1-Typ) und seine Mischbarkeit mit den isotypen Übergangsmetallnitriden und -carbiden, Mh. Chem. 106 (1975) 1137–1147.

[16] C. Stampfl, A.J. Freeman, Stable and metastable structures of the multiphase tantalum nitride system, Phys. Rev. B 71 (2005).

[17] L. Rivaud, Structure and physical properties of polycrystalline hexagonal Ta_2N films deposited by reactive sputtering, J. Vac. Sci. Technol. A 9 (1991) 2180.

[18] C.M. Koller, A. Kirnbauer, R. Rachbauer, S. Kolozsvári, P.H. Mayrhofer, Thermally-induced phase transformation sequence of arc evaporated Ta–Al–N coatings, Scr. Mater. 113 (2016) 75–78.

[19] D. Holec, L. Zhou, R. Rachbauer, P.H. Mayrhofer, Alloying-related trends from first principles: An application to the Ti–Al–X–N system, J. Appl. Phys. 113 (2013) 113510.

[20] G.R. Lee, J.J. Lee, C.S. Shin, I. Petrov, J.E. Greene, Self-organized lamellar structured tantalum–nitride by UHV unbalanced-magnetron sputtering, Thin Solid Films 475 (2005) 45–48.

[21] K. Valleti, A. Subrahmanyam, S.V. Joshi, A.R. Phani, M. Passacantando, S. Santucci, Studies on phase dependent mechanical properties of dc magnetron sputtered TaN thin films: evaluation of super hardness in orthorhombic Ta_4N phase, J. Phys. D: Appl. Phys. 41 (2008) 45409.

[22] N. Terao, Structure of tantalum nitrides, Jpn. J. Appl. Phys. 10 (1971) 248–259.

[23] M. Grosser, M. Münch, H. Seidel, C. Bienert, A. Roosen, U. Schmid, The impact of substrate properties and thermal annealing on tantalum nitride thin films, Appl. Surf. Sci. 258 (2012) 2894–2900.

[24] Angelkort, C., Berendes, A., Lewalter, H., Bock, W., Kolbesen, B.O., Formation of tantalum nitride films by rapid thermal processing, Thin Solid Films 437 (2003) 108–115.

[25] B. Grossmann, N. Schalk, C. Czettl, M. Pohler, C. Mitterer, Phase composition and thermal stability of arc evaporated $Ti_{1-x}Al_xN$ hard coatings with $0.4 \leq x \leq 0.67$, Surf. Coat. Technol. 309 (2017) 687–693.

[26] C. Mitterer, P.H. Mayrhofer, J. Musil, Thermal stability of PVD hard coatings, Vacuum 71 (2003) 279–284.

PUBLICATION III

High-temperature tribology and oxidation of $Ti_{1-x-y}Al_xTa_yN$ hard coatings

Surface and Coatings Technology, in press,

DOI: 10.1016/j.surfcoat.2018.02.062

by

Birgit Grossmann, Michael Tkadletz, Nina Schalk,
Christoph Czettl, Markus Pohler, Christian Mitterer

1. Introduction

Although hard, protective coatings have been the focus of worldwide research for several decades, there is still the challenge to meet the demands of future cutting applications. The incorporation of a fourth element into ternary coating material systems to further enhance their properties is a common procedure in order to improve the cutting performance or to widen the spectra of possible applications. Higher throughput and the therefore increasing temperatures at the cutting edge result in further demands for improvement of thermal stability as well as oxidation resistance of hard coatings. For severe applications, coatings within the $Ti_{1-x}Al_xN$ system show a beneficial evolution of mechanical properties due to microstructural changes at elevated temperatures. Spinodal decomposition of the metastable face-centered cubic (fcc) $Ti_{1-x}Al_xN$ solid solution leads to formation of fcc-AlN and fcc-TiN domains, and the emerging coherency strains result in a hardness increase at temperatures in the range of 700 to 1000 °C (age hardening) [1–3]. However, exceeding this temperature, the metastable fcc-AlN transforms into its stable wurtzite form (w-AlN), which is unfavored due to its inferior mechanical properties [2,3]. An additional w-AlN phase is also formed in $Ti_{1-x}Al_xN$ when x exceeds the solubility limit of ~0.67, resulting in a dual-phase structure consisting of fcc-$Ti_{1-x}Al_xN$ and w-AlN. At even higher Al contents, coatings with a single w-$Ti_{1-x}Al_xN$ phase are formed [1,2,4,5]. Despite the hardness increase due to spinodal decomposition of fcc-$Ti_{1-x}Al_xN$, the limited oxidation resistance obstructs the practicability of this coating system at elevated temperatures, eventually providing the decisive factor for failure.

During oxidation up to ~750 °C, the inward diffusion of oxygen and the formation of a single Ti/Al based oxide layer is the main ongoing reaction; however above 750 °C, inward diffusion of oxygen and outward diffusion of Al atoms happen simultaneously, and an outermost, dense Al_2O_3-rich layer and underneath a porous TiO_2-rich scale develop [6–8]. TiO_2 exists in two forms, i.e., anatase (a) TiO_2 and rutile (r) TiO_2. The transformation temperature for bulk a-TiO_2 to r-TiO_2 was found to be at 915 °C [9], while for coatings and powders the metastable a-TiO_2 can transform between 400-1000 °C to the stable r-TiO_2, depending on purity, synthesis

and environmental conditions [10,11]. The monotropic transformation is accompanied by a density increase [12], resulting in stress generation due to the difference in volume and in the formation of pores at the nitride-oxide interface. This deteriorates the adhesion of the oxide layer [6,11], where the direct formation of the r-TiO_2 layer without prior formation of a-TiO_2 is beneficial for $Ti_{1-x}Al_xN$ coatings. In addition, the substoichiometric form of TiO_2 (the so-called Magnéli phase series Ti_nO_{2n-1} with $3<n<10$ [13]) reduces friction and hence less heat is generated at the cutting edge, which is a crucial factor for tool lifetime and performance.

The advantageous effect of alloying additional elements to $Ti_{1-x}Al_xN$ was intensively studied by numerous authors [14–18]. In particular, addition of Ta to $Ti_{1-x}Al_xN$ proved to be beneficial in terms of enhancing thermal stability [19–22] and oxidation resistance [7,12,21,23,24]. Ta stabilizes the fcc-$Ti_{1-x-y}Al_xTa_yN$ solid solution up to slightly higher Al contents [19] and retards spinodal decomposition as well as w-AlN formation to higher temperatures [22]. The oxidation resistance is affected by Ta addition in different ways: (I) since the cubic to wurtzite transformation is shifted to higher temperatures, the resulting volume change [25,26] and therefore stress and crack formation is also postponed; thus, diffusion of oxygen through the fcc lattice is reduced; (II) the a-TiO_2 phase formation is suppressed by Ta incorporation, and the transition of a-TiO_2 to r-TiO_2, which is accompanied by a volume change, is hindered [12]; (III) Ta^{5+} (as formed in Ta_2O_5) represents a higher ionization state than Ti^{4+} (as formed in TiO_2) and thus reduces the number of oxygen vacancies in the rutile layer more efficiently, which leads to a decreased oxidation of the remaining $Ti_{1-x-y}Al_xTa_yN$ layer [7,23,27].

Although several papers have been published on the benefits of Ta addition to $Ti_{1-x}Al_xN$ hard coatings, the influence of Ta contents, varied systematically up to high values within the $Ti_{1-x-y}Al_xTa_yN$ system on the tribological properties, thermal stability as well as oxidation resistance has not yet been studied in detail. Since a comprehensive understanding of the mutual links between oxidation and wear is of crucial importance, but still missing in literature, the main focus of the present study relies on the evaluation of the tribological properties of $Ti_{1-x-y}Al_xTa_yN$ hard coatings

and the resulting oxide layer formation during testing at elevated temperatures. Within this work, the influence of Ta atomic fractions of $0 \leq y \leq 0.23$ in $Ti_{1-x-y}Al_xTa_yN$ hard coatings on the oxidation resistance and the consequently changing tribomechanical response of the coatings to dry sliding tests at elevated temperatures were investigated. For this purpose, ball-on-disk tests in ambient air at room temperature (RT), 700 and 900 °C were conducted, and cross-sections of the oxide scale formed during the elevated temperature tests were analyzed in order to detect changes of the constitution, the thickness as well as the pore size of the oxide scale formed for the Ta contents chosen. Fundamental relationships between microstructure, oxide layer formation and tribological properties of $Ti_{1-x-y}Al_xTa_yN$ hard coatings were established.

2. Experimental Methods

Six coatings with different Ta contents were deposited using cathodic arc evaporation in an industrial scale Oerlikon Balzers Innova deposition plant. For all deposition runs, four cathodes were simultaneously operated at a DC arc current of 200 A in a pure N_2 reactive gas atmosphere (total pressure ~3 Pa). The Ta content of the powder metallurgically manufactured TiTaAl compound cathodes was 0, 1, 2.5, 5, 10, and 15 at.-%, respectively, at a constant Ti:Al atomic ratio of 1:1. Polished cemented carbide disks (Ø 30 mm × 4 mm), consisting of 77 wt.-% tungsten carbide, 11 wt.-% cobalt and 12 wt.-% mixed carbides, served as substrates. Additionally, a low alloy steel foil was used as substrate and dissolved after coating deposition in 2M nitric acid. The resulting coating powder was then dried and ground in order to provide a sole coating material for thermal stability investigations, to prevent undesired reactions between coating and substrate material. The substrates were plasma etched in an argon plasma, and afterwards coatings were deposited in a N_2 atmosphere using twofold rotation at a bias voltage of -70 V and a substrate temperature of 550 °C.

The coating thickness was determined by means of the ball cratering technique using a CSM CaloWear device, and was found to be in the range of 6.7±0.6

µm for each coating. The elemental composition of the coatings was detected by energy-dispersive X-ray spectroscopy (EDX) using an Oxford Instruments INCA extension in a Zeiss EVO 50 scanning electron microscope (SEM) and built-in sensitivity factors for quantification. The friction coefficient was determined with ball-on-disk tests in ambient air, utilizing a CSM high-temperature ball-on-disk tribometer. The normal load applied was 5 N for the tests at RT and 700 °C, and 1 N for the tests at 900 °C, while the distance was set to 300 m. An alumina ball (Ø 6 mm) was used as counterpart. Special emphasis was laid on measurement procedures for the 900 °C tests with identical preheating time as well as heating and cooling rates, to ensure that differences in oxide scale formation solely stem from the respective coating compositions. The overall time of exposure to a temperature of 900 °C was about 60 min. An optical white light interferometer (Veeco Wyko NT1000) was utilized to reconstruct a 2D profile for three different positions on the generated wear tracks.

The microstructure of the coatings was determined using X-ray diffraction (XRD) in grazing incidence mode (angle of incidence 2°) in a Bruker D8 Advance diffractometer using Cu K_α radiation with λ=0.154 nm. Cross-sections of the disks after ball-on–disk tests at 900 °C were prepared using an Orsay Physics Cobra Z-05 focused ion beam (FIB) in a Zeiss Auriga 40 SEM workstation, to investigate oxide scale and phases formed during annealing. Furthermore, a cross-section within the wear track of the coating with y=0.17 was prepared by FIB for EDX mapping of the oxide scale formed directly in the wear-affected zone. In order to obtain a smooth FIB cut for all samples prepared, a Pt layer was deposited on the oxidized coatings. The FIB/SEM was equipped with two detectors, an in-lens secondary electron (SE) detector for determination of the topographical information, while for illustration of the elemental contrast an in-lens energy-selected backscattered (ESB) detector was used. EDX mapping was conducted using an EDAX EDX Apollo XPP detector. In order to determine the mass change during oxidation, thermogravimetric analysis (TGA) of the coating powders was performed in synthetic air in a Setaram Setsys Evo 2400 dynamic differential scanning calorimeter (DSC) equipped with a

thermobalance. The gas flow was set to 16 ml/sec and the heating and cooling rate to 10 K/min up to a maximum temperature of 1500 °C; the samples were immediately cooled down after reaching 1500 °C. The microstructure of the annealed coating powders was determined using the same X-ray diffractometer as mentioned before, but in Θ-2Θ geometry.

3. Results

3.1. Chemical composition

The chemical analysis revealed a considerably higher Ta content of the coatings than of the respective cathodes. The coating elemental compositions were determined as $Ti_{0.53}Al_{0.47}N$, $Ti_{0.52}Al_{0.47}Ta_{0.01}N$, $Ti_{0.52}Al_{0.44}Ta_{0.04}N$, $Ti_{0.50}Al_{0.42}Ta_{0.08}N$, $Ti_{0.46}Al_{0.37}Ta_{0.17}N$, and $Ti_{0.43}Al_{0.34}Ta_{0.23}N$ for the cathodes with Ta contents of 0, 1, 2.5, 5, 10, and 15 at.-%, respectively. The nitrogen content was 48.3±3.3 at.-% for all coatings. Hereinafter, we will refer to the Ta content y in $Ti_{1-x-y}Al_xTa_yN$ to distinguish the different coatings.

3.2. Friction and wear

The average friction coefficients of the $Ti_{1-x-y}Al_xTa_yN$ coatings are presented in Fig. 1 as a function of the Ta content. At RT, the friction coefficient increases with the increase of the Ta content, which coincides with the slight hardness increase from 32.6±1.2 GPa for y=0 to 34.4±0.8 GPa for y=0.17 reported in our previous work [22]. Increasing the testing temperature to 700 °C leads to an average friction coefficient of ~0.63, which is hardly influenced by the Ta content. The oxidation of the coating and formation of a single amorphous oxide scale containing Ti, Al and Ta is expected to contribute to the observed friction reduction [7,8]. For the sample with y=0 tested at 900 °C, the friction coefficient is ~0.6; however, with the addition of a small Ta content (y=0.01) it decreases to 0.5. For y=0.04 and y=0.08, the friction coefficient decreases again to ~0.47, and it reaches its lowest value of 0.44 for y=0.17, which represents a reduction of 25 % compared to the Ta-free coating. The

coating with y=0.23 shows with 0.7 the highest friction coefficient for all coatings tested at 900 °C.

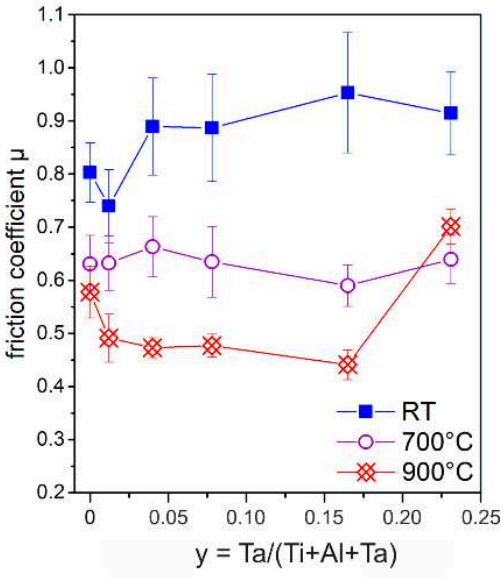

Fig. 1 Friction coefficient at RT, 700 °C and 900 °C of $Ti_{1-x-y}Al_xTa_yN$ coatings as a function of the Ta content.

During oxidation of Ti containing materials, the formation of substoichiometric Ti_nO_{2n-1} is very likely, leading for a fraction of Ti atoms to a lower ionization state (Ti^{3+} ions instead of Ti^{4+}). These Magnéli phases are well known to decrease the friction of a surface by formation of lubricant-like low-shear crystallographic planes with reduced bond strength [28,29]. The addition of Ta leads to the formation of $(Ti,Ta)_nO_{2n-1}$, where the pentavalent Ta furthermore decreases the amount of oxygen vacancies in the coating, consequently promoting Magnéli phase formation and leading to the decrease of the friction coefficient observed in Fig. 1. The abrupt increase of the friction coefficient for y=0.23 is a possible response of the coating to the significantly increased oxygen deficiency in $(Ti,Ta)_nO_{2n-1}$. Gardos *et al.* [28,30] also observed an increase of the bond strength due to a change of the crystallographic shear planes, when the oxygen deficiency exceeds a certain limit, which leads to an increase of the friction coefficient.

The influence of the Ta content on the wear performance of $Ti_{1-x-y}Al_xTa_yN$ coatings at the three chosen temperatures was evaluated by means of the 2D profiles of the wear tracks illustrated in Fig. 2. For the coatings y=0 and y=0.01, the ball-on-disk tests at RT result in a broad wear track with a depth of up to ~1 µm. The wear track depth slightly increases to ~1.5 µm for y=0.04, 0.08 and 0.17. With increasing Ta content, also a smoothening of the track is observable, probably stemming from the formation of smaller abrasive wear particles.

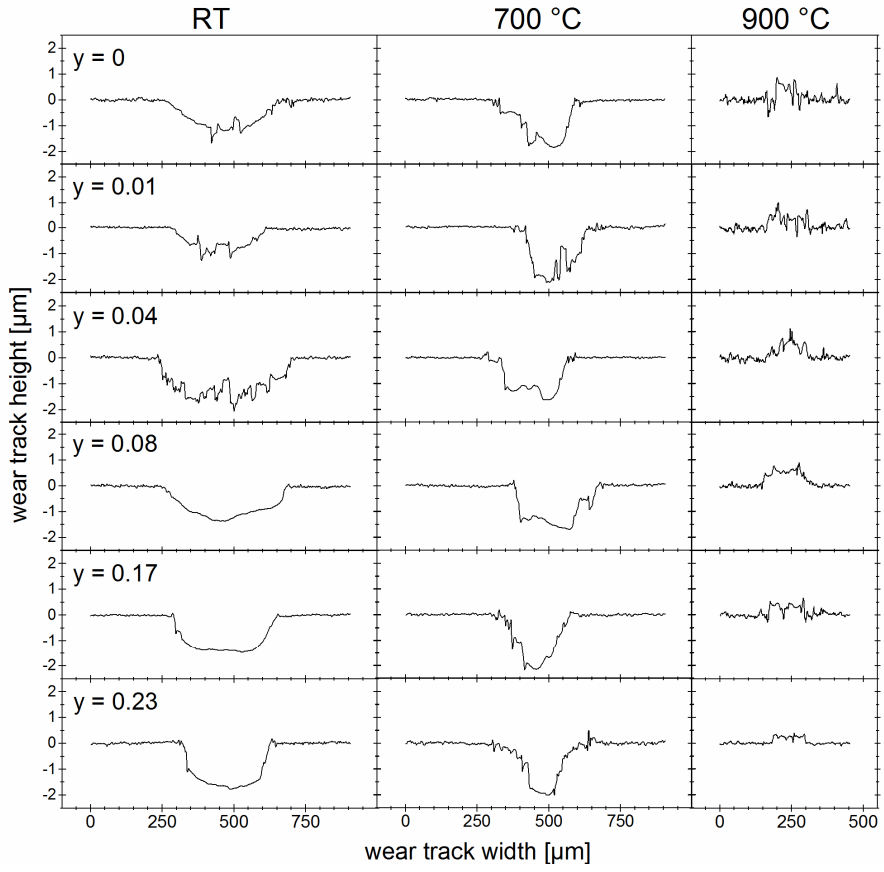

Fig. 2 2D profiles of the wear track of $Ti_{1-x-y}Al_xTa_yN$ coatings after ball-on-disk tests at RT, 700 and 900 °C. While the RT and 700 °C tests were carried out with a normal load of 5 N, a normal load of 1 N was used for the 900 °C test.

The wear track of the coating containing the highest Ta content shows the most pronounced depth. For the coatings tested at 700 °C, the wear track width decreases with increasing Ta content, while its depth slightly increases. The resulting narrow and deep track points towards abrasion as the dominating wear mechanism.

The temperature increase to 900 °C leads to an increasing tendency of adhesion of the softened and thus worn Al_2O_3 ball material to the coating. It can be assumed that this material transfer superimposes the effect of the still present abrasion. This material transfer prevents to detect an eventual increase of abrasive wear due to the formation of the Ta_2N phase at high Ta contents, as reported in [22]. The wear track profiles indicate material transfer for all coatings, but a decreasing wear track height with increasing Ta content. Although the normal load for the ball-on-disk tests at 900 °C was only 1 N compared to 5 N for RT and 700 °C, the resulting wear track width is with ~200 µm rather similar to the 700 °C tests, and about half of the track width compared to the tests at RT. The average surface roughness of the coatings decreases significantly with increasing Ta content, as indicated in Fig. 2 by the smoother coating surface outside the wear tracks.

3.3. Microstructural changes after 900 °C ball-on-disk test

A detailed microstructural analysis for the as deposited coatings can be found in our previous publication [22] and revealed a single fcc-$Ti_{1-x-y}Al_xTa_yN$ phase for all six coatings, with diffraction peaks located between fcc-TiN (ICDD 00-038-1420) and fcc-AlN (ICDD 00-025-1495). With increasing Ta content, a peak shift towards lower diffraction angles and thus to the standard peak position for fcc-TaN (ICDD 00-049-1283) was observed [22], which corresponds with [24]. Fig. 3 represents the X-ray diffractogram of the $Ti_{1-x-y}Al_xTa_yN$ coatings after the 900 °C ball-on-disk tests. For y=0, the dominant peak at ~43.5 ° indicates the presence of the metastable $Ti_{1-x}Al_xN$ solid solution. Its pronounced width as well as the shoulder on the right hand side indicate ongoing spinodal decomposition [31]. The fcc-$Ti_{1-x}Al_xN$ peak is also visible at ~37 °. Additionally, an enhanced signal at ~33 ° leads to the conclusion that a small amount of w-AlN (ICDD 01-076-0702) is present. Furthermore, several peaks stemming from oxides can be observed, i.e., r-TiO_2 (ICDD 00-021-1276), a-TiO_2 (ICDD 00-021-1272), and small fractions of α-Al_2O_3 (ICDD 00-010-0173), which is at ~38° superimposed by a-TiO_2. The increased Ta content for y=0.01 leads to a slight reduction of the a-TiO_2 peak intensity, while the r-TiO_2 peaks increase (best

visible at ~54 ° in Fig. 3). The w-AlN peak intensity also decreases due to the incorporation of Ta into the metastable $Ti_{1-x}Al_xN$, which is known to stabilize the cubic phase [22]. An increase of the Ta content to y=0.04 results in another increase of the r-TiO_2 peak intensity, while the anatase peak further decreases. For this coating, the α-Al_2O_3 peak at ~35° reaches the highest intensity. The fcc-$Ti_{1-x-y}Al_xTa_yN$ peaks are slightly shifted to lower diffraction angles, towards the standard peak position of TaN. Additionally, they are slightly narrower with a lower pronounced shoulder than for y=0, indicating a retarded progress of spinodal decomposition as a result of Ta incorporation [19,22,23].

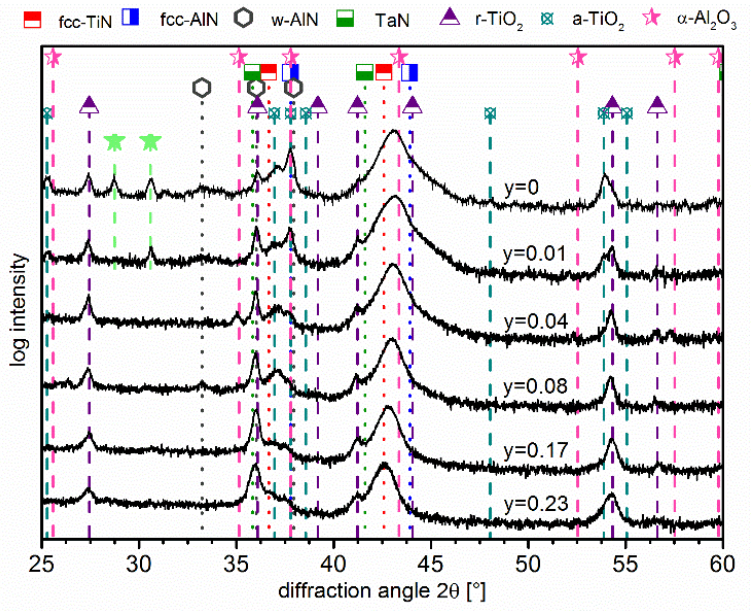

Fig. 3 Phase evolution of $Ti_{1-x-y}Al_xTa_yN$ coatings after ball-on-disk tests at 900 °C. The green asterisks mark the peak position stemming from substrate oxides.

The coatings with y=0.08, 0.17 and 0.23 show a further peak shift of the fcc-$Ti_{1-x-y}Al_xTa_yN$ peak with increasing Ta content to lower angles. The r-TiO_2 peak at ~36 ° is increasing with increasing Ta content, and is also slightly shifted to lower diffraction angles. The shifts of both peaks evidence the increasing lattice parameter due to the incorporation of the larger Ta atoms in the fcc-TiN and r-TiO_2 lattice, respectively. Besides the formation of these crystalline oxides, the existence of amorphous Al_2O_3-based scales at high Ta contents can not be excluded.

3.4. Oxidation during 900 °C ball-on-disk test

Since at elevated temperatures friction and wear mechanisms are significantly affected by tribo-oxidation [32], the nature of the formed oxide layers is of vital interest. Therefore, cross-sections of the tribometer disks tested at 900 °C outside the wear track were prepared by FIB. Fig. 4 illustrates three selected coatings to provide a comprehensive overview of the differences in oxide scale formation for a $Ti_{1-x}Al_xN$ coating as well as $Ti_{1-x-y}Al_xTa_yN$ with moderate and high Ta contents, respectively. Fig. 4a reveals two different oxide layers formed on the coating with y=0, an outermost, dark and dense layer and a bright layer next to the remaining $Ti_{1-x}Al_xN$ layer, which contains big pores. Since the darker color within backscattered images indicates elements with lower atomic number, the top layer is assumed to be Al_2O_3-rich, while the porous layer below is TiO_2-rich, as also observed in [6,7,12,23]. The Al_2O_3-rich layer thickness is ~100 nm, while the porous TiO_2-rich layer is ~170 nm thick. Oxidation of the sample with y=0.08 leads to an Al_2O_3-rich layer with a thickness of ~80 nm, and a TiO_2-rich layer below with an average thickness of 140 nm, which seems to be separated into two sublayers (Fig. 4b). A dense TiO_2–rich layer is formed below the Al_2O_3-rich top layer, and comprises dark spots indicating an Al_2O_3-rich phase within the TiO_2-rich layer. The porous TiO_2-rich layer beneath shows again a brighter color, with pores at the interface to the remaining $Ti_{1-x-y}Al_xTa_yN$ layer. In Fig. 4c, the oxide scale formed on sample y=0.23 is depicted. The Al_2O_3-rich layer is reduced to ~50 nm thickness, and the TiO_2-rich layer is again separated into two layers; the Al_2O_3-rich phase is evident within the TiO_2-rich oxide scale directly beneath the dense Al_2O_3-rich layer (i.e., the dense, spotted TiO_2-rich layer), while at the interface to the remaining $Ti_{1-x-y}Al_xTa_yN$ layer, a dense, unspotted TiO_2-rich layer is formed.

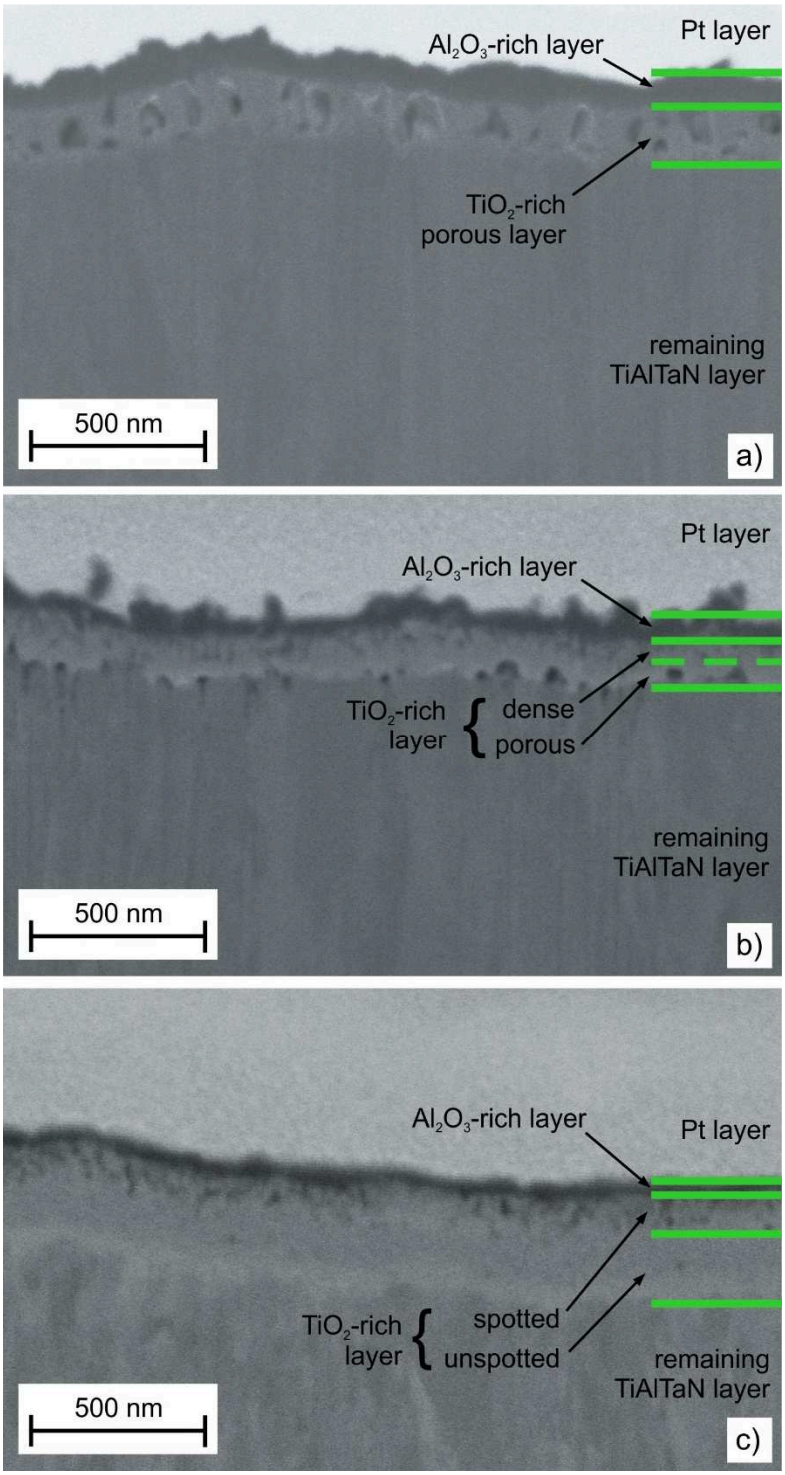

Fig. 4 SEM micrographs of FIB cross-sections outside the wear track showing in detail the oxide layer formation on $Ti_{1-x-y}Al_xTa_yN$ coatings after ball-on-disk tests at 900 °C. a) y=0 b) y=0.08 and c) y=0.23

For a better understanding of the elemental distribution within the oxide layer formed during the 900 °C ball-on-disk test, a FIB cut for the sample with y=0.17, again outside of the wear track, was prepared and investigated using EDX-mapping (Fig. 5). Two detectors were used, to determine on the one hand the topographical information (SE detector, Fig. 5a), while on the other hand the ESB detector image illustrates the elemental contrast in Fig. 5b. A Pt layer to obtain a smooth FIB cut is visible on the top of the oxidized coating. The Al_2O_3-rich layer of sample y=0.17 is with ~75 nm thicker compared to ~50 nm for y=0.23. Nevertheless, the TiO_2-rich layer is similarly separated into two layers, a dense unspotted layer next to the interface to the remaining $Ti_{1-x-y}Al_xTa_yN$ layer and a layer next to the Al_2O_3-rich top layer, which is characterized by dark spots within the bright TiO_2-rich matrix. Fig. 4c does not unambiguously evidence the dark spots as Al_2O_3-rich. However, equivalent dark spots appear white in Fig. 5a and thus invalidate the existence of pores. In the EDX-mapping in Fig. 5c, the elemental distribution of Al, Ti, O and Pt is displayed. The oxygen content decreases within the oxide scale from the surface to the interface to the remaining $Ti_{1-x-y}Al_xTa_yN$ layer. Within the remaining $Ti_{1-x-y}Al_xTa_yN$ layer, diffusion of Al towards the interface to the oxide layer can be detected, evidenced by the elevated Al content close to the interface. The chemical distribution of Al and Ti within the oxide layer can be best seen in Fig. 5d. Beyond the Pt layer, mainly Al can be observed. This high Al content corresponds to the dark Al_2O_3-rich layer and in part to the intermediate bright oxide layer containing the dark, Al_2O_3-rich regions visible in Fig. 5b. This observation supports the notion of the existence of an Al_2O_3-rich layer as top layer [6,8]. Further, a subjacent Al-depleted, Ti- and O-rich layer can be identified, which corresponds to the bright layer in Fig. 5b.

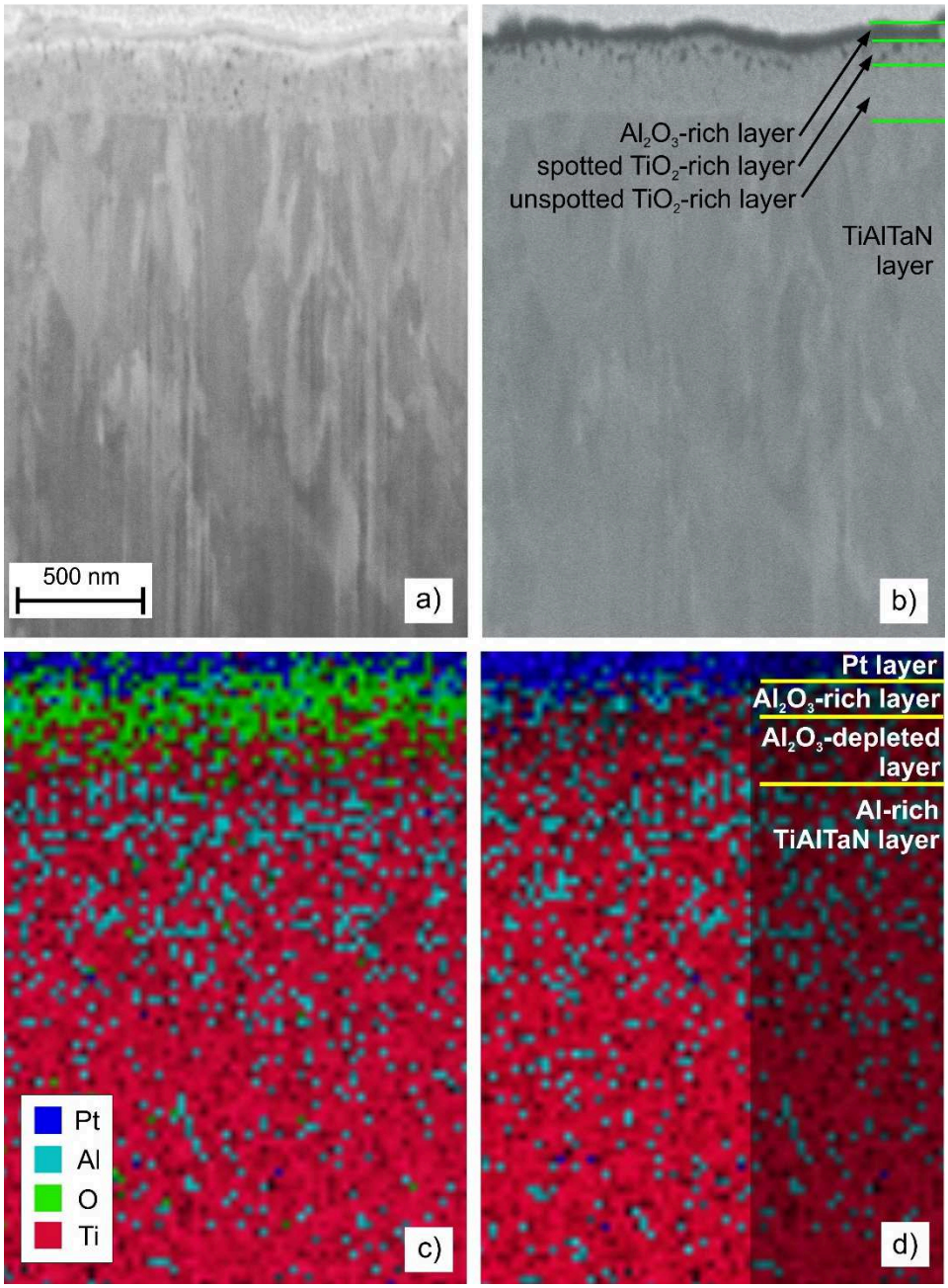

Fig. 5. SEM micrographs of the surface near region of the coating with y=0.17 after the ball-on-disk test at 900 °C obtained with a) the SE and b) the ESB detector. c) displays the elemental distribution of Pt, Al, Ti and O in the oxide scale obtained by EDX-mapping, d) reveals the elemental distribution of Pt, Al and Ti in the oxide scale to highlight the distribution of merely the metallic components. The Pt layer stems from surface preparation for the FIB cut.

In order to study the effect of the ball-on-disk test at 900 °C on oxide scale formation, cross-sections of the wear track of a disk of y=0.17 prepared by FIB are

presented in Fig. 6. Fig. 6a displays the transition of the coating surface from outside to inside the wear track. On the one hand, the formation of an easy shearable oxide layer and its abrasion during continuous sliding leads to a reduction of the coating thickness by ~350 nm within the wear track. On the other hand, indications for adhesive wear are also evident by the additional build-up of material at the surface. This adhesion layer material appears porous, and is polished to a smooth surface on top of the wear track.

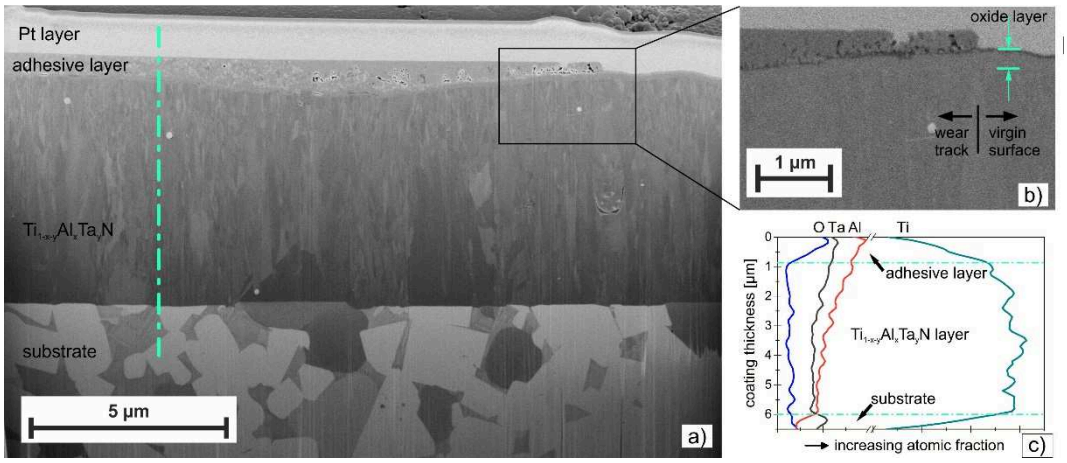

Fig. 6. Cross-section of the sample with y=0.17 within the wear track obtained by the ball-on-disk test at 900 °C. a) SEM micrograph obtained by the SE detector, b) SEM micrograph obtained by the ESB detector showing in detail the oxide layer on the surface, as well as the transition zone to the wear track and therefore the adhesive wear layer and c) EDX line profile at the position marked in a) by the dashed line.

In Fig. 6b the transition zone to the wear track is illustrated in detail. Again, differences in the layer composition are illuminated by ESB micrographs. The oxide layer unaffected by wear, i.e., next to the wear track, shows a similar appearance in Fig. 5b. Underneath the adhesive layer, the appearance of the oxide layer changes, since the dark Al_2O_3-rich top layer starts to diminish with increasing distance to the transition zone. The elemental distribution along the dashed vertical line in Fig. 6a is illustrated in Fig. 6c. Since the Ti content tends to be overrated by EDX due to its superimposition with N (see the high Ti content in the unaffected $Ti_{1-x-y}Al_xTa_yN$ coating), Fig. 6c provides merely a distributional trend over the coating thickness. Up to ~1 µm from the top (the Pt layer was cut out), the adhesive

layer can be recognized. The oxygen content reaches next to the surface its highest values, and is then decreasing within the adhesive layer. The Al content is within the adhesive layer relatively high, and reaches its highest value next to the surface, corroborating the assumption of worn Al_2O_3 ball material as well as worn coating material adhering on the coating surface. Within this adhesive layer, the observed fractions of Ta and Ti stem from worn coating material, where the Ti signal is most probably again overrated. The Al content is continuously decreasing within the remaining $Ti_{1-x-y}Al_xTa_yN$ layer. The distribution of the Ta content over the layer thickness shows an increased Ta content within the adhesive layer, and a continuous decline up to ~3 µm coating thickness. Below that level, the Ta content remains at a constant level evidencing the Ta content of the unaffected coating.

3.5. Oxidation during annealing in synthetic air

Fig. 7 represents the mass change of the coating powders during annealing in synthetic air, as determined by TGA. A threshold of 5 % mass gain is marked to facilitate assessment of the oxidation progress. Up to ~900 °C the oxidation behavior expressed by the mass gain of the coatings is similar, yielding a slight increase for all six coatings. The coating without Ta starts to oxidize first; between 950 and 1000 °C, a drastic mass increase occurs, and the coating attains 5 % mass gain at 980 °C. The former is attributed to the formation of TiO_2, since among the metals present within the coating Ti oxidizes first, as evidenced by its lower activation energy for oxidation compared to Al [6]. The subsequent formation of a dense Al_2O_3 top layer is a possible explanation for the slight slope change at ~1025 °C, since it reduces the diffusivity of oxygen from the surface via the porous TiO_2 towards the remaining $Ti_{1-x-y}Al_xTa_yN$ coating. Oxidation is assumed to be complete at 1160 °C, since no further mass change can be observed. At this temperature, a maximum mass gain of ~26 % is reached, which is in good agreement with [12]. For y=0.01, the oxidation starts at the same temperature as for y=0; it hits the 5 % mass gain threshold at 985 °C and the maximum mass gain is ~25 %. Likewise, a slope change occurs between 980 and 1020 °C due to the formation of the denser Al_2O_3. For the coatings with y=0.04 up

to 0.23 a similar behavior can be observed, but every process is shifted to higher temperatures and is less pronounced with increasing Ta content. The threshold of 5 % mass gain is shifted from 1020 for y=0.04 to 1085 °C for y=0.23. Oxidation is complete at 1270 °C for y=0.23, while e.g. the powder of y=0.01 is fully oxidized at 1120 °C. The lower mass gain of the Ta containing coatings visible in Fig. 7 can be explained by the relatively higher initial density of the as deposited coatings, which is a result of the considerably higher mass of Ta.

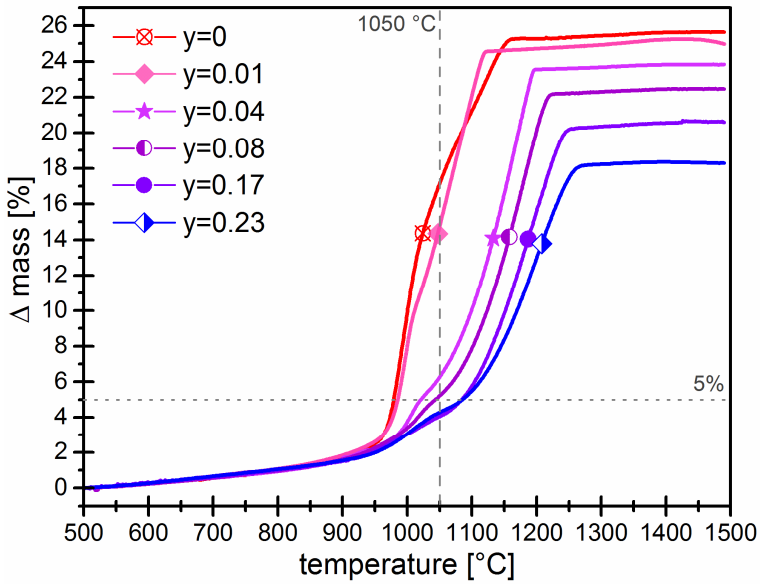

Fig. 7 Dynamical thermal analysis shows the relative mass gain observed for $Ti_{1-x-y}Al_xTa_yN$ coatings during annealing in synthetic air. A threshold of 5 % mass gain is marked for easier comparison of the oxidation onset temperature.

XRD measurements of the coating powders annealed up to 1500 °C in synthetic air (not shown here) yielded that all six coatings were completely oxidized, with r-TiO_2, α-Al_2O_3 and in addition the orthorhombic Al_2TiO_5 phase [33]. With increasing Ta content, the peak intensity of the Al_2TiO_5 phase decreased, while the intensity of the r-TiO_2 peaks increased, suggesting the incorporation of Ta into the rutile structure. Additional annealing treatments in synthetic air up to 1050 °C were performed, and the subsequent XRD measurements revealed the microstructural changes during oxidation (Fig. 8). The pattern of the powdered coating without Ta indicates nearly complete oxidation, evidencing dominating r-TiO_2 and α-Al_2O_3. A

slightly enhanced background signal at ~43.5° stems from the assumingly remaining fcc-$Ti_{1-x}Al_xN$ solid solution. For y=0.01, the signal at ~43.5° representing the fcc-$Ti_{1-x-y}Al_xTa_yN$ phase is slightly more pronounced; additionally the decrease of the peaks of TiO_2 as well as α-Al_2O_3 point towards a less advanced oxidation progress than for y=0. This trend is more pronounced for y=0.04, where the fcc-$Ti_{1-x-y}Al_xTa_yN$ peak reaches the same intensity as the r-TiO_2 peaks, which are together with the α-Al_2O_3 peaks again decreasing in intensity. The fcc-$Ti_{1-x-y}Al_xTa_yN$ peaks are visible at a diffraction angle of 37 and 43°, i.e., between the standard peak position of fcc-TiN and fcc-AlN, indicating a considerable amount of fcc-$Ti_{1-x-y}Al_xTa_yN$ in the coating.

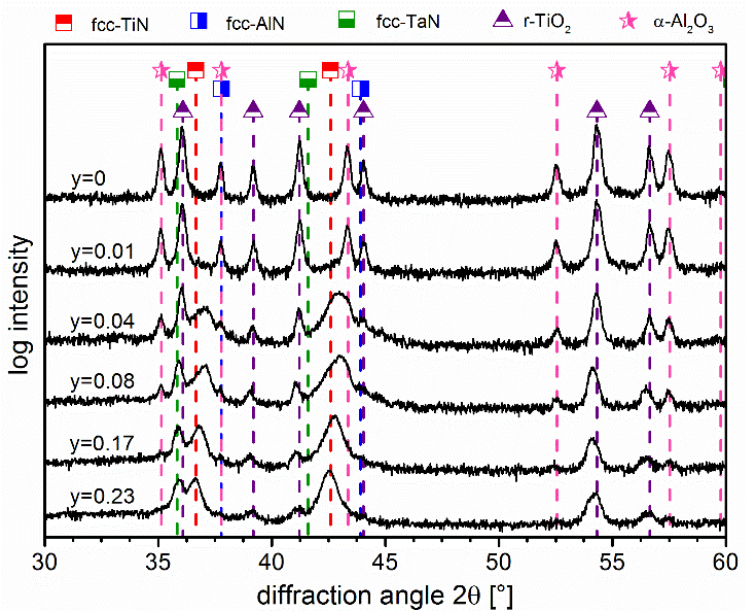

Fig. 8 Phase evolution of powdered $Ti_{1-x-y}Al_xTa_yN$ coatings after annealing at 1050 °C in synthetic air.

Another increase of the Ta content to y=0.08 results in formation of a dominating peak at ~43°. With respect to the Ta-free coating, the intensity of the r-TiO_2 peaks is decreased and slightly shifted to lower diffraction angles, which indicates the incorporation of Ta into the r-TiO_2. The α-Al_2O_3 peaks appear much smaller, since the majority of the present Al is incorporated within the fcc-$Ti_{1-x-y}Al_xTa_yN$ solid solution. A further increase of the Ta content to y=0.17 and y=0.23 leads to a further shift of the fcc-$Ti_{1-x-y}Al_xTa_yN$ peaks to lower angles, towards

the standard peak position of fcc-TaN. In addition, the intensity of the r-TiO_2 and the α-Al_2O_3 peaks is further decreased.

4. Discussion

Our findings demonstrate that the tribological properties of $Ti_{1-x-y}Al_xTa_yN$ coatings at elevated temperatures strongly depend on the oxide layer formation, which is significantly affected by the Ta content. Based on the findings obtained within this work by SEM and XRD, a schematic of the evolution of the different oxide layers and their thickness as a function of the Ta content is presented in Fig. 9.

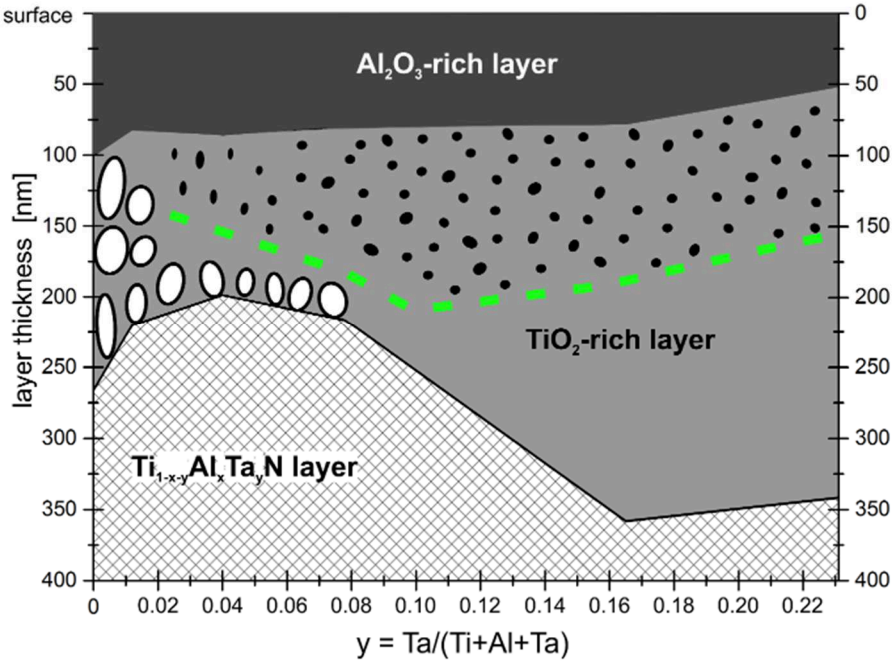

Fig. 9 Schematic of the oxide layers formed during ball-on-disk tests at 900 °C outside of the wear track, as a function of the Ta content of the respective coating. The green dashed line marks the separation of the TiO_2-rich layer into two layer sections: pores are marked in white while the dark spots indicate the Al_2O_3 phase formed within the TiO_2-rich layer.

The dark, Al_2O_3-rich top layer shows with 100 nm the highest layer thickness for y=0, and is decreasing to ~80 nm with increasing Ta content. The coating containing the highest Ta content shows another decrease of the Al_2O_3-rich layer to ~50 nm, which comprises half the thickness than the coating without Ta.

This decrease of the thickness of the Al_2O_3-rich layer with increasing Ta content is on the one hand related to the hindered transport of Al atoms through the densified TiO_2-rich layer, and on the other hand to the decrease of the Al fraction within the coating (see section 3.1). The TiO_2-rich layer has an average thickness of 170 nm for y=0, and contains pores throughout the entire layer, as evidenced by Fig. 4a. The beneficial effect of even small amounts of Ta is also visible for the TiO_2-rich layer, since it reduces the layer thickness to 140 nm for y=0.01 and 120 nm for y=0.04. This is in good agreement with the shift of the oxidation onset to higher temperatures, as shown in Fig. 7. However, at a Ta content of y=0.08 the thickness of the TiO_2-rich layer increases again to ~140 nm. With increasing Ta content it is more and more separated into a porous region adjacent to the remaining $Ti_{1-x-y}Al_xTa_yN$ layer with a distinct decrease of the pore size, and a pore-free layer comprising dark Al_2O_3-rich spots within the bright TiO_2-rich layer, as demonstrated by Fig. 4b. The observed decreasing amount of a-TiO_2 formed during ball-on-disk tests at 900 °C as a result of the increasing Ta content (see Fig. 3) is in good agreement with the decreasing pore density, since the stable r-TiO_2 has a higher density than the metastable a-TiO_2. Additionally, it also concurs with the decreasing friction coefficient, since r-TiO_2 is characterized by improved friction properties as a result of the accompanied formation of Magnéli phases [28]. The addition of Ta leads to the formation of substoichiometric mixed $(Ti,Ta)_nO_{2n-1}$ Magnéli phases, where the formation of Ti^{3+} instead of Ti^{4+} caused by the oxygen deficiency is promoted by the higher valence of Ta^{5+}. These phases exhibit superior friction and wear properties due to their decreased shear strength compared to the fully stoichiometric phase [29,32], which is responsible for the decrease of the friction coefficient with increasing Ta content in Fig. 1.

The high Ta contents within samples y=0.17 and y=0.23 lead to a pore free, 290 nm thick TiO_2-rich layer, and its distinct separation between a layer spotted with Al_2O_3 on top of the unspotted layer next to the remaining $Ti_{1-x-y}Al_xTa_yN$ coating. A possible explanation for the drastic increase of the overall TiO_2-rich layer thickness is the decrease of the dense Al_2O_3 layer thickness as a result of the decreasing Al

content, and the therefore lowered protection of further oxidation. After oxidation, the high Ta containing coatings show a much smoother surface than the coatings with $y \leq 0.04$, as can be observed at the 2D profiles in Fig. 2 outside of the wear track for the coatings tested at 900 °C. The contribution of Ta to lower friction can be observed up to y=0.17 (see Fig. 1); for y=0.23, the friction coefficient increases as a result of the exceptional oxygen deficiency, which is known to lead to an increase of the bonding strength of the shear planes, if it falls below a critical level (as observed in [28]).

As summarized in Fig. 9, a moderate Ta content of y=0.08 is suitable to avoid formation of porous and thus less mechanically stable oxide scales. Exceeding this content yields thick oxide layers, which might be brittle and delaminate when exposed to severe tribological conditions with cyclic loads during application.

5. Conclusions

The investigation of $Ti_{1-x-y}Al_xTa_yN$ coatings with a Ta content between $0 \leq y \leq 0.23$ has revealed a strong relation between tribological properties and oxide layer formation, where the latter is significantly affected by the Ta content. After ball-on-disk tests performed at 900 °C, the metastable anatase TiO_2 phase is formed within the oxide scale of coatings with a low Ta content, which deteriorates its mechanical and thermal stability. The transformation of anatase TiO_2 to the stable rutile TiO_2 is accompanied by a volume change, leading inevitably to formation of pores, which provide additional diffusion paths and thus decrease the oxidation resistance. With increasing Ta content, the formation of anatase is suppressed, which reduces the pore density within the oxide scale and enhances oxidation resistance. Additionally, the substoichiometric rutile $(Ti,Ta)_nO_{2n-1}$ phase is formed, which results in a decreased shear strength of the oxide scale and to a decrease of the friction coefficient with increasing Ta content.

Acknowledgements

The authors are very grateful to Bernhard Sartory (Materials Center Leoben) for SEM, EDX and FIB investigations, and to Thaddäa Rath for the tribological investigations at 700°C. This work was financially supported by the Österreichische Forschungsförderungsgesellschaft FFG (grant number 845255).

References

[1] A. Hörling, L. Hultman, M. Odén, J. Sjölén, L. Karlsson, Thermal stability of arc evaporated high aluminum-content $Ti_{1-x}Al_xN$ thin films, J. Vac. Sci. Technol. A 20 (2002) 1815.

[2] A. Hörling, L. Hultman, M. Odén, J. Sjölén, L. Karlsson, Mechanical properties and machining performance of $Ti_{1-x}Al_xN$-coated cutting tools, Surf. Coat. Technol. 191 (2005) 384–392.

[3] P.H. Mayrhofer, A. Hörling, L. Karlsson, J. Sjölén, T. Larsson, C. Mitterer, L. Hultman, Self-organized nanostructures in the Ti–Al–N system, Appl. Phys. Lett. 83 (2003) 2049.

[4] A. Kimura, H. Hasegawa, K. Yamada, T. Suzuki, Effects of Al content on hardness, lattice parameter and microstructure of $Ti_{1-x}Al_xN$ films, Surf. Coat. Technol. 120-121 (1999) 438–441.

[5] C. Wüstefeld, D. Rafaja, V. Klemm, C. Michotte, M. Kathrein, Effect of the aluminium content and the bias voltage on the microstructure formation in $Ti_{1-x}Al_xN$ protective coatings grown by cathodic arc evaporation, Surf. Coat. Technol. 205 (2010) 1345–1349.

[6] D. McIntyre, J.E. Greene, G. Hakansson, J.E. Sundgren, W.D. Münz, Oxidation of metastable single-phase polycrystalline $Ti_{0.5}Al_{0.5}N$ films: Kinetics and mechanisms, J. Appl. Phys. 67 (1990) 1542–1553.

[7] V. Khetan, N. Valle, D. Duday, C. Michotte, M.-P. Delplancke-Ogletree, P. Choquet, Influence of temperature on oxidation mechanisms of fiber-textured AlTiTaN coatings, ACS Appl. Mater. Interfaces 6 (2014) 4115–4125.

[8] F. Vaz, L. Rebouta, M. Andritschky, da Silva, M. F., J.C. Soares, Thermal oxidation of $Ti_{1-x}Al_xN$ coatings in air, ECerS 17 (1997) 1971–1977.

[9] H.J. Rösler, Lehrbuch der Mineralogie, 5th ed., p. 399, Deutscher Verlag für Grundstoffindustrie, Leipzig, 1991.

[10] D.A.H. Hanaor, C.C. Sorrell, Review of the anatase to rutile phase transformation, J Mater Sci 46 (2011) 855–874.

[11] R.D. Shannon, J.A. Pask, Kinetics of the Anatase-Rutile Transformation, J. Am. Ceram. Soc. 48 (1965) 391–398.

[12] R. Hollerweger, H. Riedl, J. Paulitsch, M. Arndt, R. Rachbauer, P. Polcik, S. Primig, P.H. Mayrhofer, Origin of high temperature oxidation resistance of Ti–Al–Ta–N coatings, Surf. Coat. Technol. 257 (2014) 78–86.

[13] F.C. Walsh, R. Wills, The continuing development of Magnéli phase titanium sub-oxides and Ebonex® electrodes, Electrochim. Acta 55 (2010) 6342–6351.

[14] D. Holec, L. Zhou, R. Rachbauer, P.H. Mayrhofer, Alloying-related trends from first principles: An application to the Ti–Al–X–N system, J. Appl. Phys. 113 (2013) 113510.

[15] K. Kutschej, P.H. Mayrhofer, M. Kathrein, P. Polcik, C. Mitterer, Influence of oxide phase formation on the tribological behaviour of Ti–Al–V–N coatings, Surf. Coat. Technol. 200 (2005) 1731–1737.

[16] M. Pfeiler, J. Zechner, M. Penoy, C. Michotte, C. Mitterer, M. Kathrein, Improved oxidation resistance of TiAlN coatings by doping with Si or B, Surf. Coat. Technol. 203 (2009) 3104–3110.

[17] K. Kutschej, N. Fateh, P.H. Mayrhofer, M. Kathrein, P. Polcik, C. Mitterer, Comparative study of $Ti_{1-x}Al_xN$ coatings alloyed with Hf, Nb, and B, Surf. Coat. Technol. 200 (2005) 113–117.

[18] M. Mikula, M. Truchlý, D.G. Sangiovanni, D. Plašienka, T. Roch, M. Gregor, P. Ďurina, M. Janík, P. Kúš, Experimental and computational studies on toughness enhancement in Ti-Al-Ta-N quaternaries, J. Vac. Sci. Technol. A 35 (2017) 60602.

[19] R. Rachbauer, D. Holec, P.H. Mayrhofer, Increased thermal stability of Ti–Al–N thin films by Ta alloying, Surf. Coat. Technol. 211 (2012) 98–103.

[20] R. Rachbauer, D. Holec, P.H. Mayrhofer, Phase stability and decomposition products of Ti–Al–Ta–N thin films, Appl. Phys. Lett. 97 (2010) 151901.

[21] C.M. Koller, R. Hollerweger, C. Sabitzer, R. Rachbauer, S. Kolozsvári, J. Paulitsch, P.H. Mayrhofer, Thermal stability and oxidation resistance of

arc evaporated TiAlN, TaAlN, TiAlTaN, and TiAlN/TaAlN coatings, Surf. Coat. Technol. 259 (2014) 599–607.

[22] B. Grossmann, A. Jamnig, N. Schalk, C. Czettl, M. Pohler, C. Mitterer, Tailoring age hardening of $Ti_{1-x}Al_xN$ by Ta alloying, J. Vac. Sci. Technol. A 35 (2017) 60604.

[23] M. Pfeiler, C. Scheu, H. Hutter, J. Schnöller, C. Michotte, C. Mitterer, M. Kathrein, On the effect of Ta on improved oxidation resistance of Ti–Al–Ta–N coatings, J. Vac. Sci. Technol. A 27 (2009) 554.

[24] M. Pfeiler, G.A. Fontalvo, J. Wagner, K. Kutschej, M. Penoy, C. Michotte, C. Mitterer, M. Kathrein, Arc Evaporation of Ti–Al–Ta–N Coatings: The Effect of Bias Voltage and Ta on High-temperature Tribological Properties, Tribol Lett 30 (2008) 91–97.

[25] N.E. Christensen, I. Gorczyca, Calculated structural phase transitions of aluminum nitride under pressure, Phys. Rev. B 47 (1993) 4307–4314.

[26] R. Rachbauer, S. Massl, E. Stergar, D. Holec, D. Kiener, J. Keckes, J. Patscheider, M. Stiefel, H. Leitner, P.H. Mayrhofer, Decomposition pathways in age hardening of Ti-Al-N films, J. Appl. Phys. 110 (2011) 023515.

[27] R.G. Reddy, Y. Li, M.F. Arenas, Oxidation of a Ternary Ti_3Al-Ta Alloy, High Temp. Mater. Process. 21 (2002) 195–206.

[28] M.N. Gardos, Magnéli phases of anion-deficient rutile as lubricious oxides. Part I. Tribological behavior of single-crystal and polycrystalline rutile (Ti_nO_{2n-1}), Tribol Lett 8 (2000) 65–78.

[29] M. Woydt, Tribological characteristics of polycrystalline Magnéli-type titanium dioxides, Tribol Lett 8 (2000) 117–130.

[30] M.N. Gardos, The effect of anion vacancies on the tribological properties of rutile (TiO_{2-x}), Tribol. Trans. 31 (1988) 427–436.

[31] P.H. Mayrhofer, D. Music, J.M. Schneider, Ab initio calculated binodal and spinodal of cubic $Ti_{1-x}Al_xN$, Appl. Phys. Lett. 88 (2006) 71922.

[32] K. Holmberg, A. Matthews, Coatings tribology: Properties, techniques and applications in surface engineering, Tribology series 28, Elsevier, Amsterdam, 1994.

[33] D. Hochauer, C. Mitterer, M. Penoy, C. Michotte, H.P. Martinz, M. Kathrein, Thermal stability of doped CVD κ-Al_2O_3 coatings, Surf. Coat. Technol. 204 (2010) 3713–3722.